1-1-2013

Coarse-Grained Lattice Monte Carlo Simulation of Continuous Systems

Xiao Liu
University of Pennsylvania, liuxiao2008@gmail.com

Recommended Citation

Liu, Xiao, "Coarse-Grained Lattice Monte Carlo Simulation of Continuous Systems" (2013). *Publicly Accessible Penn Dissertations*. 662.
http://repository.upenn.edu/edissertations/662

Coarse-Grained Lattice Monte Carlo Simulation of Continuous Systems

Abstract

In this thesis, a coarse-grained lattice Metropolis Monte Carlo (CG-MMC) framework is presented for simulating atomic and molecular fluid systems described by standard molecular force-fields. The CG-MMC technique is demonstrated to be highly thermodynamically consistent with the underlying full resolution problem using a series of detailed comparisons, including vapor-liquid equilibrium phase envelopes and spatial density distributions for the square well, Lennard-Jones argon, and simple point charge (SPC) water models.

The principal computational bottleneck associated with computing a coarse-grained interaction function for evolving particle positions on the discretized domain is addressed by the introduction of new closure approximations. It is shown that the coarse-grained potential can be computed at multiple temperatures and scales using a single set of free energy calculations. Theoretical underpinnings of CG-MMC are further discussed by addressing additional potential sources of error as well as computational advantages.

Two important applications of CG-MMC model are presented. The first application explores the validity of CG-MMC model in non-equilibrium simulations. A variant of the CG-MMC method is developed that enables simulation of coarse-grained non-equilibrium trajectories. It is shown that the resulting NECG-MMC method generates trajectories that are consistent with coarse-grained Langevin dynamics. The second application explores the validity of CG-MMC model in large-scale simulation. Multi-particle move capability is developed and the scaling properties of the CG-MMC approach are studied. A non-equilibrium simulation at large scale is used as a demonstration.

Degree Type

Dissertation

Degree Name

Doctor of Philosophy (PhD)

Graduate Group

Chemical and Biomolecular Engineering

First Advisor

Talid Sinno

Second Advisor

Warren D. Seider

Subject Categories

Chemical Engineering

COARSE-GRAINED LATTICE MONTE CARLO SIMULATION OF CONTINUOUS SYSTEMS

Xiao Liu

A DISSERTATION

in

Chemical and Biomolecular Engineering

Presented to the Faculties of the University of Pennsylvania

in

Partial Fulfillment of the Requirements for the

Degree of Doctor of Philosophy

2013

Supervisor of Dissertation

____

Dr. Talid Sinno, Professor of Chemical and Biomolecular Engineering

Co-Supervisor of Dissertation

____

Dr. Warren D. Seider, Professor of Chemical and Biomolecular Engineering

Graduate Group Chairperson

____

Dr. Raymond J. Gorte, Professor of Chemical and Biomolecular Engineering

Dissertation Committee

Dr. John C. Crocker, Associate Professor of Chemical and Biomolecular Engineering
Dr. Robert A. Riggleman, Assistant Professor of Chemical and Biomolecular Engineering
Dr. Vaclav Vitek, Professor of Materials Science and Engineering

COARSE-GRAINED LATTICE MONTE CARLO SIMULATION OF CONTINUOUS SYSTEMS

Xiao Liu

ABSTRACT

COARSE-GRAINED LATTICE MONTE CARLO SIMULATION OF CONTINUOUS SYSTEMS

Xiao Liu
Dr. Talid Sinno
Dr. Warren D. Seider

In this thesis, a coarse-grained lattice Metropolis Monte Carlo (CG-MMC) framework is presented for simulating atomic and molecular fluid systems described by standard molecular force-fields. The CG-MMC technique is demonstrated to be highly thermodynamically consistent with the underlying full resolution problem using a series of detailed comparisons, including vapor-liquid equilibrium phase envelopes and spatial density distributions for the square well, Lennard-Jones argon, and simple point charge (SPC) water models.

The principal computational bottleneck associated with computing a coarse-grained interaction function for evolving particle positions on the discretized domain is addressed by the introduction of new closure approximations. It is shown that the coarse-grained potential can be computed at multiple temperatures and scales using a single set of free energy calculations. Theoretical underpinnings of CG-MMC are further discussed by addressing additional potential sources of error as well as computational advantages.

Two important applications of CG-MMC model are presented. The first application explores the validity of CG-MMC model in non-equilibrium simulations. A variant of the CG-MMC method is developed that enables simulation of coarse-grained non-equilibrium trajectories. It is shown that the resulting NECG-MMC method generates trajectories that are consistent with coarse-grained Langevin dynamics. The second application explores the validity of CG-MMC model in large-scale simulation. Multi-particle move capability is developed and the scaling properties of the CG-MMC approach are studied. A non-equilibrium simulation at large scale is used as a demonstration.

TABLE OF CONTENTS

LIST OF TABLES

LIST OF ILLUSTRATIONS

Chapter 1

Introduction and Fundamentals

1.1 Introduction of the Coarse-Graining Concept

Coarse-graining (CG) has been applied in a wide variety of settings in order to extend the scope of full-resolution atomistic and molecular simulations such as Metropolis Monte Carlo (MMC) and molecular dynamics (MD), which are usually otherwise limited to nanoscale lengths and times even with the use of empirical interatomic potentials. In general, coarse-graining refers to a transformation in which some of the degrees-of-freedom describing the system are eliminated, increasing computational efficiency at the expense of detail, and depending on the assumptions made, accuracy. While it is difficult to neatly classify the many types of coarse-graining schemes that have been described in the literature, they broadly fall under two coarse-graining strategies: *topological coarse-graining* and *spatial coarse-graining*.

1.2 Coarse-Graining Strategy I: Topological Coarse-Graining

One very popular class of methods is *topological* coarse-graining, in which several atoms are grouped into effective entities that obey a new interaction function which implicitly contains all the atomic-level interaction information, e.g. the MARTINI force field for biomolecular systems [1, 2] and potentials for DNA-coated colloids [3-5]. A coarse-grained representation of the lipopeptide C16-KGGK obtained from MARTINI model is shown in Figure 1.1 to demonstrate the general idea of topological coarse-graining.

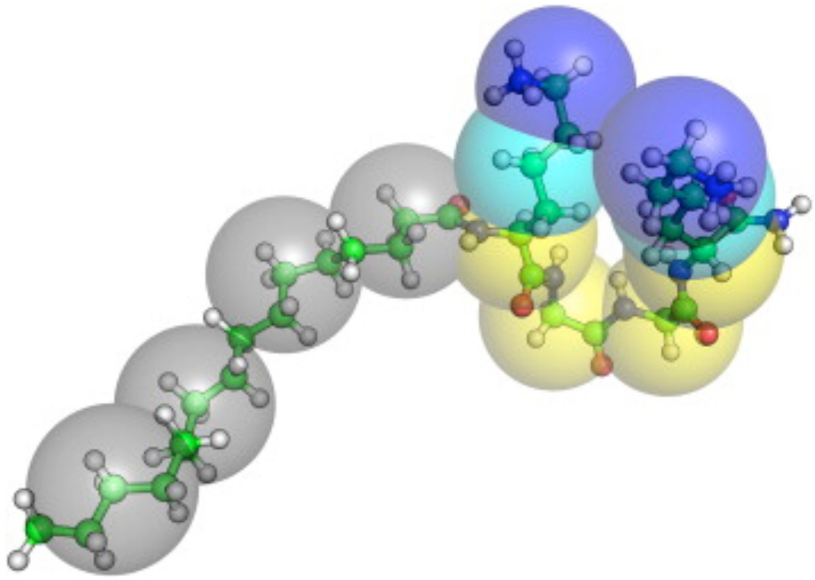

Figure. 1.1: A representative example of topological coarse-graining by grouping several atoms into effective entities: Coarse-grained representation of the lipopeptide C16-KGGK (MARTINI model) overlaying a ball-and-stick all-atom representation. The non-polar saturated fatty acid tail is represented by gray spheres. Individual peptide backbone segments are represented by yellow spheres, apolar lysine chains by turquoise, and each lysine's charged sidechain amino group by blue. Figure and coarse-graining description is taken from ref. [1].

The central challenge in topological coarse-graining is to then find the appropriate coarse-grained interaction potential to ensure thermodynamic and dynamical consistency with the full-resolution system. Accuracy in coarse-grained modeling depends on how well the coarse-grained partition function (determined by the coarse-grained potential) reproduces the full-resolution partition function (determined by the full-resolution potential).

Without loss of generality, consider the canonical (*NVT*) ensemble system. For the full-resolution system with N_{full} all-particle representation, the canonical partition function shows

$$Q_{full}(N_{full},V,T)=\frac{1}{\Lambda^{3N_{full}}N_{full}!}\int d\mathbf{r}^{N_{full}}\exp\left[-\frac{U_{full}(\mathbf{r}^{N_{full}})}{k_BT}\right], \qquad (1.1)$$

where $U_{full}(\mathbf{r}^{N_{full}})$ is a specified interaction potential function for the full-resolution system. Upon coarse-graining, the number of coarse-grained entities reduced to N_{CG} by grouping several atoms into one effective entity. The coarse-grained canonical partition function now is defined as

$$Q_{CG}(N_{CG},V,T)=\frac{1}{\Lambda^{3N_{CG}}N_{CG}!}\int d\mathbf{r}^{N_{CG}}\exp\left[-\frac{U_{CG}(\mathbf{r}^{N_{CG}})}{k_BT}\right], \qquad (1.2)$$

where $U_{CG}(\mathbf{r}^{N_{CG}})$ is the coarse-grained interaction potential. When an appropriate coarse-grained interaction potential is defined such that the coarse-grained partition function can reproduce the full-resolution partition function after topological coarse-graining, thermodynamic and dynamical consistency is achieved between the coarse-grained representation and the full-resolution system.

Examples of successful approaches for accomplishing this task include force matching [6-8], Boltzmann inversion [9, 10], and relative entropy minimization [11-13]. The resulting coarse-grained models have been used to study a broad range of materials and systems including polymers [14-16], biomolecules [17, 18], nanoparticle [19], and nanoparticle-polymer assemblies [20], and ionic liquids [21], to name a few.

Another paradigm for topological coarse-graining is based on combining particle and field-based descriptions into a single multiresolution simulation [22-26]. Although solid-state simulations are not a focus of the present paper, much progress has been made in this type of coarse-graining for crystalline materials [27]. The quasicontinuum (QC) framework, in particular, has emerged as a very powerful tool in the simulation of micro-structure evolution [28, 29]. QC method significantly reduces the total number of degrees of freedom that must be considered by introducing representative atoms (see Figure 1.2). The Hamiltonian is reduced to a coarse-grained version as a function of momenta, effective mass and position of the representative atoms; therefore, this approach is also properly categorized as topological coarse-graining.

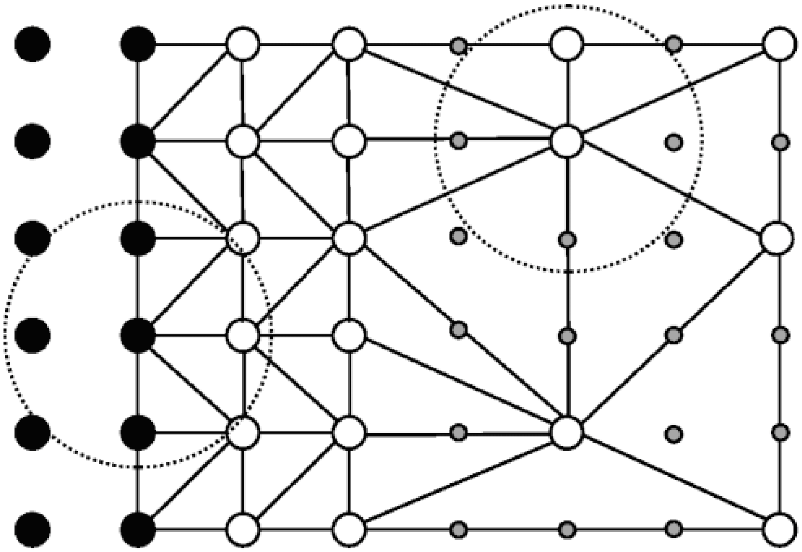

Figure. 1.2: A representative example of a coarse-grained alternative to molecular dynamics without all-atom representation using a quasicontinuum framework. Atom populations are split between representative atoms (large circles) and constrained atoms (small gray circles). The average positions of the latter are estimated from the position of the

former using finite-element interpolation. Among the representative atoms, a distinction is made between nonlocal atoms (black circles), whose energy only depends on representative atoms (as shown by the dashed circle whose radius equals the cutoff distance of the interatomic potential), and local atoms (white circles), that interact with constrained atoms. Figure and coarse-graining description is taken from ref. [29].

1.3 Coarse-Graining Strategy II: Spatial Coarse-Graining

A different approach for degree-of-freedom reduction is to map the problem onto a fixed lattice, starting with block-spin renormalization group theory [30]; here, we refer to this type of transformation as *spatial* coarse-graining. In spatial coarse-graining of polymeric systems, for example, chains are placed on fixed grids and allowed to evolve subject to discretized moves; one example is the bond fluctuation method [31].

Recently, spatial coarse-graining has been applied extensively to Metropolis and kinetic Monte Carlo simulations of Ising-type systems in which the aim is to transform one (high-resolution) lattice problem onto a lower-resolution lattice by grouping together lattice sites into coarse “cells”. Notable examples include the work of Katsoulakis, Vlachos and coworkers [32-37] and Ismail et al. [38, 39]. A key element of these methods is the closure rule, which dictates how processes on the fine-grid lattice are averaged to generate consistent processes on the coarse-cell grid. This may be accomplished using analytical approximations [32, 40] or numerical averaging [38, 39, 41-43]. The spatial coarse-graining approach is particularly useful when there is no obvious topological simplification (or grouping) to be made, e.g. in atomic or simple molecular systems. Lattice-based simulations are also extremely computationally efficient if the missing degrees-of-freedom are properly accounted for [44-47]. Vlachos and coworkers have developed a mathematical formulation to coarse-grain the events from a fine-grid lattice to a coarse-grid one [34]. In their work, several closure rules are developed such as Local Mean-Field approximation [33, 35], quasichemical approximation [48] and approximation based on numerical methods [48].

The coarse-graining approach essentially begins with the full atomic scale lattice and groups several adjacent lattice sites together into "cells" that then effectively represent the new unit element of the coarse-grained lattice as shown in Figure 1.3. The reduction in the spatial degrees of freedom is accounted for by increasing the number of states that each coarse-grained cell can exist in. For example, if each coarse-grained cell contains four lattice sites, it is now characterized by a four-level state variable, or "occupancy". The key task of the coarse-graining process is to define consistent new rates for the evolution of the particle population from one coarse-grained cell to the next. The essence of all coarse-grained simulations under this framework is to effectively compute the interaction energy on a coarse-grid lattice based on the characteristics of the fine-grid interactions so that the coarse-grained model performance matches the fine-grid model. In the work of Vlachos and coworkers, this is achieved by averaging over all the interactions within a cell and also over interactions between interacting cells, i.e. the coarse-grained interaction between two coarse-grained cells *l* and *k* is given by [32, 34]:

$$U(k,l) = \frac{1}{A} \iint_{D_l \times D_k} U(r-s)\,drds \tag{1.3}$$

where $U(r-s)$ is the interaction between lattice sites r and s, A is the area of the origin cell plus that of cells within interaction range.

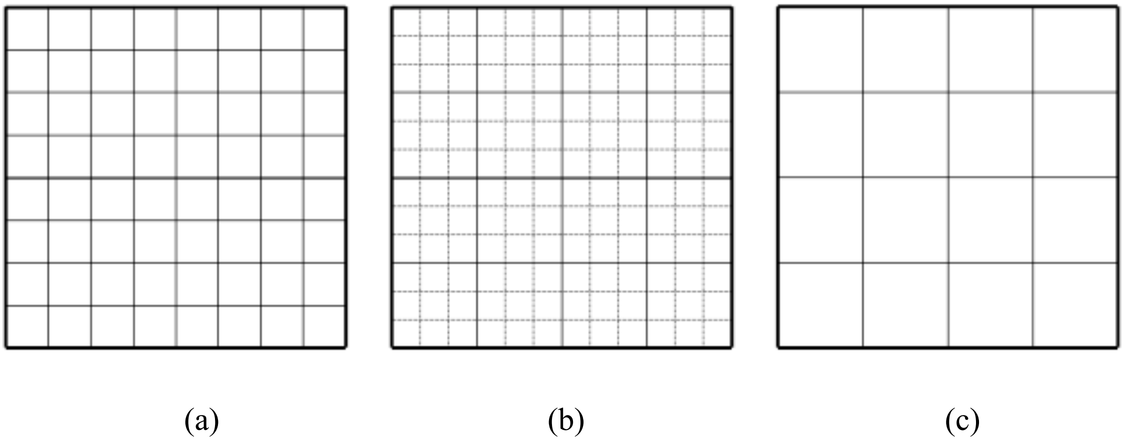
(a) (b) (c)

Figure. 1.3: Schematic representation of spatial coarse-graining. (a) Fine grid lattice with occupancy 0 or 1 in each fine-grid site; (b) Coarse-graining process by grouping every 3×3 adjacent fine-grid sites into one coarse-grid site; (c) Corresponding coarse grid lattice with maximum occupancy 9 in each coarse-grid site.

Ismail and coworkers also successfully developed a wavelet transform based coarse-graining approach, and successfully applied it in Monte Carlo simulation of Ising model [38, 39]. The basic idea of wavelet transform is to separate data sets into sets representing local averages and local differences. For example, by rewriting the Hamiltonian in terms of wavelet-transformed averages and differences, the number of variables is reduced from *2N* to *N*. More importantly, the wavelet transform can be iterated if applied to successive sets of averages; thus it becomes a hierarchical technique that can map data from one scale to the next coarser scale. As in the demonstration of wavelet-accelerated Monte Carlo (WAMC) model, a lattice model is hierarchically coarse-grained by computing the probability distribution for successively larger block spins.

While previous approaches for spatial coarse-graining have focused on weakly interacting systems, Dai and coworkers developed numerical closure rules that account for strong interactions between particles, which are generally present in aggregating systems [42, 44, 45]. Although previous closure rules in the literature provide a good approximation for weak or short-ranged interactions, they fail for strong interactions: clusters of particles form during simulations and cause inhomogeneities, which presents a great challenge for coarse-graining. A new spatial coarse-graining approach was introduced aiming at greatly extending the scope of the Lattice Kinetic Monte Carlo (LKMC) simulations and proper closure methods for systems with strong interactions.

Two important contributions were presented in their coarse-graining framework as critical elements for successful coarse-graining in strongly interacting systems. The first is the use of exponentially weighted average binding energies, rather than simple averages. Physically, the former is an average over the transition rates, which effectively biases the average binding energy in a given coarse cell towards less strongly bound configurations that are more likely to generate particle hops. In the limit of weak interactions, both averaging schemes were shown to converge to the same estimate for the average binding energy of a coarse cell. The second is the consideration of intra- and inter-cell coupling by an appropriate choice of closure rule, which has been largely ignored in previous literature.

Two limitations were also pointed out about this approach. The first was that the computational cost for the Wang-Landau simulations [49] used to compute the coarse-grained interaction potential as input in the CG-LKMC model was significant, especially for high levels of coarse-graining and small LKMC systems. The second was that the

LKMC approach is not highly transferable, in particular to variable temperature systems.

1.4 Motivations of a New Coarse-Graining Framework

The primary reason that coarse-grained models are able to simulate larger length and time scales is due to the reduction in configuration space. With reduced configurational complexity, the states of a system can be sampled more rapidly, resulting in significant computational speed gains. Previous spatial coarse-graining methods [33-35, 38, 39, 42] effectively focus on computing the interaction energy on a coarse-grid lattice based on the characteristics of the fine-grid interactions so that the coarse-grained model performance matches the fine-grid model as shown in Figure 1.4.

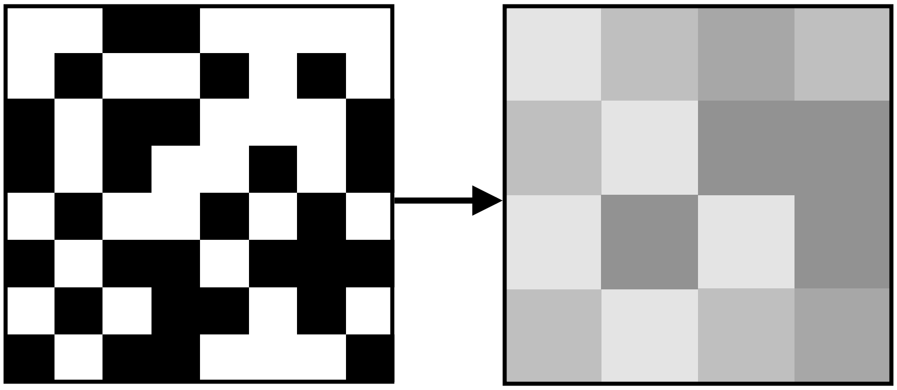

Figure 1.4: Schematic representation of reduction in configuration space by spatial coarse-graining. High-resolution lattice-based description is converted to a lower-resolution description. Cell shading represents local particle density within each coarse cell.

However, compared to a full-resolution continuous model, its lattice representation is usually limited by the missing off-lattice entropic contribution [50, 51]. In other words, a lattice-based representation of a continuous model is already a “coarse-grained” version with configuration space reduced. Since any information lost from the low-resolution of the starting model cannot be captured in further coarse-grained model, a full resolution continuous model (with highest resolution) is generally a better starting point, although may not be necessary in all cases, than its lattice representation. This thesis focuses on developing a coarse-graining framework that extends the spatial coarse-graining concept to a far more general situation in which particles subjected to an arbitrary, continuous interaction potential are mapped directly onto a rigid lattice of variable scale as shown in Figure 1.5.

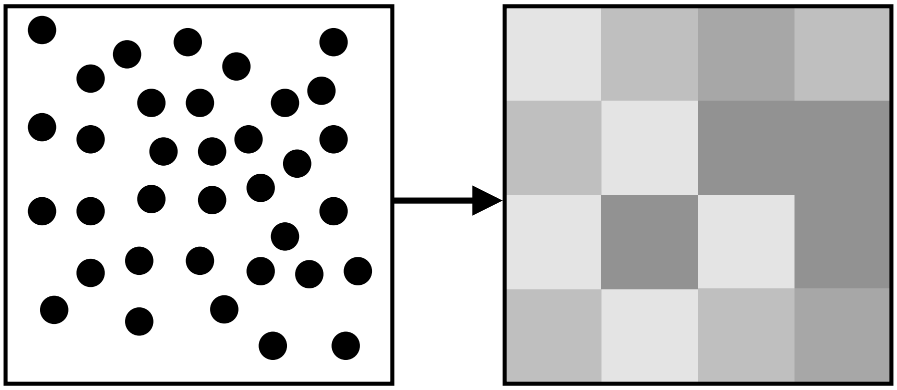

Figure. 1.5: Schematic representation of reduction in configuration space by spatial coarse-graining. A continuous-space particle-based representation is directly coarse-grained into a low-resolution lattice-based description. Cell shading represents local particle density within each coarse cell.

Our approach is to bypass the already “coarse-grained” lattice model and start from a full-resolution continuous model with information coarse-grained in a way such that the off-lattice entropic contribution will be intrinsically included. A coarse-grained interaction potential, pre-computed directly from the continuous potential using a numerical averaging procedure, is then used to evolve coarse-grained Metropolis Monte Carlo (CG-MMC) simulations. The first goal is to establish that the rules governing coarse-grained models are equivalent to the rules followed by full-resolution models. In this derivation, the Metropolis Monte Carlo (MMC) becomes the direct frame of reference for CG-MMC.

Inspired by previous spatial coarse-graining framework [33-35, 38, 39, 42], we also pay special attention to the appropriate choice of closure rule as well as the intra- and inter-cell coupling when developing the continuous coarse-graining framework. The intra- and inter-cell coupling is replaced by an averaged environmental contribution. In addition, the principal computational bottleneck associated with computing a coarse-grained interaction function for evolving particle positions on the discretized domain is addressed by the introduction of new closure approximations. In particular, we show that the coarse-grained potential, like all coarse-grained interaction functions, is generally a function of temperature and coarse-graining level and can be computed at multiple temperatures and scales using a single set of free energy calculations.

1.5 Theoretical Foundations of General Monte Carlo Simulation

Molecular simulation of many-body systems can occur on discrete or coarse-graining levels. Discrete models treat individual atoms, molecules, or particles individually while the coarse-grain approach groups discrete elements into more abstract entities. In both models, simulation of the system can occur through deterministic or stochastic algorithms. Examples of the former mainly comprise of Molecular Dynamics (MD), while examples of the latter include various Monte Carlo (MC) methods, Brownian Dynamics (BD), etc.

Monte Carlo methods are derived from the statistical mechanics notion of averaging over ensembles where the intention is to map the system description onto a stochastic Markov-based framework. That is, we first choose an appropriate statistical mechanics ensemble, along with a distribution function describing the probability of occurrence of various states, and then evaluate physical quantities in this ensemble.

A general Monte Carlo simulation is now described following ref. [52] as a guideline for both the coarse-grained Metropolis Monte Carlo model (CG-MMC), and its direct frame of reference, the full-resolution Metropolis Monte Carlo model (MMC).

In more detail, the goal in general Monte Carlo simulation is to construct a set of states in the phase space $\mathbf{Q}$, in which various states occur with the probability $\mathrm{P}(\mathbf{Q})$. Thus, we devise a Markov chain such that, starting from an initial state $\mathbf{Q}_0$, other states are generated by transitions $\mathbf{Q} \to \mathbf{Q'}$ and, ultimately in the steady state, they are distributed according to $\mathrm{P}(\mathbf{Q})$. The transitions $\mathbf{Q} \to \mathbf{Q'}$ occurs in this process with a probability $p(\mathbf{Q},\mathbf{Q'})$ that defines the nature of this process and must be chosen to attain the distribution $\mathrm{P}(\mathbf{Q})$ in the steady state.

This probability must satisfy the following conditions:

(i) $p(\mathbf{Q},\mathbf{Q'}) \geq 0$, such that the transition probability cannot be negative;

(ii) $\sum_{\mathbf{Q}'} p(\mathbf{Q},\mathbf{Q}') = 1$, where the summation extends over all available states $\mathbf{Q}'$. The meaning of this condition is that every state $\mathbf{Q}$ is eventually attained in this random walk process; and

(iii) $\sum_{\mathbf{Q}'} p(\mathbf{Q}',\mathbf{Q})\mathrm{P}(\mathbf{Q}') = \mathrm{P}(\mathbf{Q})$, this condition defines the probability $p(\mathbf{Q},\mathbf{Q}')$, and it is the requirement of self-consistency, which assures that in equilibrium, the states in the phase space are distributed in accordance with the prescribed distribution function $\mathrm{P}(\mathbf{Q})$.

The trick, which leads to an elegant algorithm, used in MC is to replace the last condition by a stronger condition of microscopic reversibility

$$p(\mathbf{Q}',\mathbf{Q})\mathrm{P}(\mathbf{Q}') = p(\mathbf{Q},\mathbf{Q}')\mathrm{P}(\mathbf{Q}) \tag{1.4}$$

Clearly, equation (iii) follows from equation (1.4). By summation over Q' we obtain

$$\sum_{\mathbf{Q}'} p(\mathbf{Q}',\mathbf{Q})\mathrm{P}(\mathbf{Q}') = \mathrm{P}(\mathbf{Q})\sum_{\mathbf{Q}'} p(\mathbf{Q},\mathbf{Q}') \tag{1.5}$$

according to (ii), equation (iii) is automatically satisfied. However, it can also be satisfied in some different way, and thus equation (1.4) does not follow from (iii).

A possible choice for the transition probabilities satisfying equation (1.4) is

$$p(\mathbf{Q},\mathbf{Q}') = \frac{\mathrm{P}(\mathbf{Q}')}{\mathrm{P}(\mathbf{Q})}, \text{ when } \mathrm{P}(\mathbf{Q}') < \mathrm{P}(\mathbf{Q});$$

$$p(\mathbf{Q},\mathbf{Q}') = 1, \text{ when } \mathrm{P}(\mathbf{Q}') > \mathrm{P}(\mathbf{Q});$$

$$p(\mathbf{Q},\mathbf{Q}) = 1 - \sum_{\mathbf{Q}'\neq\mathbf{Q}} p(\mathbf{Q},\mathbf{Q}'). \tag{1.6}$$

The last equation, which follows from (ii), determines the probability with which the system remains in the state $\mathbf{Q}$ when it is already in this state.

If $\mathrm{P}(\mathbf{Q}') < \mathrm{P}(\mathbf{Q})$, then $p(\mathbf{Q}',\mathbf{Q}) = 1$ and $p(\mathbf{Q},\mathbf{Q}') = \frac{\mathrm{P}(\mathbf{Q}')}{\mathrm{P}(\mathbf{Q})}$, and thus

$$p(\mathbf{Q},\mathbf{Q}')\mathrm{P}(\mathbf{Q}) = \mathrm{P}(\mathbf{Q}') = p(\mathbf{Q}',\mathbf{Q})\mathrm{P}(\mathbf{Q}') \tag{1.7}$$

and Eq. (1.4) is satisfied.

If $\mathrm{P}(\mathbf{Q}') > \mathrm{P}(\mathbf{Q})$, then $p(\mathbf{Q},\mathbf{Q}') = 1$ and $p(\mathbf{Q}',\mathbf{Q}) = \frac{\mathrm{P}(\mathbf{Q})}{\mathrm{P}(\mathbf{Q}')}$, and thus

$$p(\mathbf{Q}',\mathbf{Q})\mathrm{P}(\mathbf{Q}') = \mathrm{P}(\mathbf{Q}) = p(\mathbf{Q},\mathbf{Q}')\mathrm{P}(\mathbf{Q}) \tag{1.8}$$

and Eq. (1.4) is satisfied.

A general Monte Carlo simulation algorithm following ref. [52] can now be described step by step as a guideline for both the CG-MMC model, and its direct frame of reference, the MMC model for analysis in future chapters:

1) Specify an initial state $\mathbf{Q}_0$ in the phase space of the system studied, which is usually represented by a starting configuration defined by positions and velocities of the particles in the full-resolution system.

2) Starting from a state $\mathbf{Q}$, which is $\mathbf{Q}_0$ for the first step, generate randomly a new state $\mathbf{Q}'$.

3) Evaluate the transition probability $p(\mathbf{Q},\mathbf{Q}')$ defined by eq. (1.6).

4) Generate a random number ζ such that $0 \le \zeta \le 1$.

5) If $p(\mathbf{Q},\mathbf{Q}') < \zeta$ then remain in the old state $\mathbf{Q}$ and go to 2).

6) If $p(\mathbf{Q},\mathbf{Q}') \ge \zeta$ accept the new state, i.e. $\mathbf{Q} \to \mathbf{Q}'$, and go to 2).

The steps 5) and 6) correspond to making the transition $\mathbf{Q} \to \mathbf{Q}'$ with the probability $p(\mathbf{Q},\mathbf{Q}')$ since the probability that $p(\mathbf{Q},\mathbf{Q}') \ge \zeta$ is equal to $p(\mathbf{Q},\mathbf{Q}')$.

1.6 Thesis Outline

Chapter 2 begins by introducing the coarse-grained lattice Metropolis Monte Carlo model (CG-MMC), including an introduction to the whole coarse-graining framework and the base case CG-MMC algorithm that will be applied in later chapters. Chapter 3 introduces additional closure approximations that may substantially enhance the utility of the CG-MMC approach by reducing the overall computational effort associated with calculation of the coarse-grained interaction potential. It also describes the theoretical underpinnings of CG-MMC by addressing additional potential sources of error as well as computational advantages. In Chapter 4, a variant of the CG-MMC method is developed that enables simulation of (coarse-grained) non-equilibrium trajectories. It is shown that the resulting method generates trajectories that are consistent with coarse-grained Langevin dynamics. In Chapter 5, multi-particle move capability is developed and the scaling properties of the CG-MMC approach are studied. A large simulation of a non-equilibrium process is used to demonstrate possible applications of CG-MMC. Conclusions and suggestions for further study are presented in Chapter 6.

Reference

---

[1] J. N. Horn, J.D. Sengillo, D. Lin, T. D. Romo, and A. Grossfield, *Biochim. Biophys. Acta* **1818**, 212 (2012).

[2] S. J. Marrink, H. J. Risselada, S. Yefimov, D. P. Tieleman, and A. H. de Vries, *J. Phys. Chem. B* **111**, 7812 (2007).

[3] P. L. Biancaniello, A. J. Kim, and J. C. Crocker, *Phys. Rev. Lett.* **94**, 058302 (2005).

[4] R. T. Scarlett, M. T. Ung, J. C. Crocker, and T. Sinno, *Soft Matter* **7**, 1912 (2011).

[5] M. E. Leunissen and D. Frenkel, *J Chem. Phys.* **134**, 084702 (2011).

[6] J. Zhou, I. F. Thorpe, S. Izvekov, and G. A. Voth, *Biophys. J.* **92**, 4289 (2007).

[7] S. Izvekov and G. A. Voth, *J. Phys. Chem. B* **109**, 2469 (2005).

[8] W. G. Noid, J. W. Chu, G. S. Ayton, V. Krishna, S. Izvekov, G. A. Voth, A. Das, and H. C. Andersen, *J. Chem. Phys.* **128**, 244114 (2008).

[9] D. Reith, M. Putz, and F. Muller-Plathe, *J. Comput. Chem.* **24**, 1624 (2003).

[10] Q. Sun and R. Faller, *J. Chem. Theory Comput.* **2**, 607 (2006).

[11] M. S. Shell, *J. Chem. Phys.* **129**, 144108 (2008).

[12] A. Chaimovich and M. S. Shell, *Phys. Rev. E* **81**, 060104 (2010).

[13] S. P. Carmichael and M. S. Shell, *J. Phys. Chem. B* **116**, 8383 (2012).

[14] A. J. Clark, J. McCarty, I.Y. Lyubimov, and M. G. Guenza, *Phys. Rev. Lett.* **109**, 168301 (2012).

[15] K. Kremer and F. Mueller-Plathe, *Mol. Simul.* **28**, 729 (2002).

[16] C. F. Abrams and K. Kremer, *J. Chem. Phys.* **115**, 2776 (2001).

[17] S. Izvekov and G. A. Voth, *J. Phys. Chem. B*, **109**, 2469 (2005).

[18] J. W. Chu and G. A. Voth, *Biophys. J.* **90**, 1572 (2006).

[19] S. Izvekov, A. Violi, and G. A. Voth, *J. Phys. Chem. B* **109**, 17019 (2005).

[20] A. J. Rahedi, J. F. Douglas, and F. W. Starr, *J. Chem. Phys.* **128**, 024902 (2008).

[21] Y. T. Wang, S. Izvekov, T. Y. Yan, and G. A. Voth, *J. Phys. Chem. B* **110**, 3564 (2006).

[22] T. P. Schulze, P. Smereka, and E. Weinan, *J. Comput. Phys.* **189**, 197 (2003).

[23] J. Li, D. Y. Liao, and S. Yip, *Phys. Rev. E* **57**, 7259 (1998).

[24] C. Y. Gao, D. M. Nicholson, D. J. Keffer, and B. J. Edwards, *J. Non-Newtonian Fluid* **152**, 140 (2008).

[25] R. Chang, G. S. Ayton, and G. A. Voth, *J. Chem. Phys.* **122**, 244716 (2005).

[26] M. Praprotnik, L. Delle Site, and K. Kremer, *Annu. Rev. Phys. Chem.* **59**, 545 (2008).

[27] J. Q. Broughton, F. F. Abraham, N. Bernstein, and E. Kaxiras, *Phys. Rev. B* **60**, 2391 (1999).

[28] R. E. Miller and E. B. Tadmor, *J. Comput. Aided Mater. Des.* **9**, 203 (2002).

[29] L. M. Dupuy, E. B. Tadmor, R. E. Miller, and R. Phillips, *Phys. Rev. Lett.* **95**, 060202 (2005).

[30] S. K. Ma, *Phys. Rev. Lett.* **37**, 461 (1976).

[31] I. Carmesin and K. Kremer, *Macromolecules* **21**, 2819 (1988).

[32] M. A. Katsoulakis, A. J. Majda, and D. G. Vlachos, *J. Comput. Phys.* **186**, 250 (2003).

[33] M. A. Katsoulakis, A. J. Majda, and D. G. Vlachos, *Proc. Natl. Acad. Sci. USA* **100**, 782 (2003).

[34] M. A. Katsoulakis and D. G. Vlachos, *J. Chem. Phys.* **119**, 9412 (2003).

[35] A. Chatterjee, D. G. Vlachos, and M. A. Katsoulakis, *J. Chem. Phys.* **121**, 11420 (2004).

[36] A. Chatterjee and D. G. Vlachos, *Chem. Eng. Sci.* **62**, 4852 (2007).

[37] A. Chatterjee, M. A. Snyder, and D. G. Vlachos, *Chem. Eng. Sci.* **59**, 5559 (2004).

[38] A. E. Ismail, G. C. Rutledge, and G. Stephanopoulos, *J. Chem. Phys.* **118**, 4414 (2003).

[39] A. E. Ismail, G. Stephanopoulos, and G. C. Rutledge, *J. Chem. Phys.* **118**, 4424 (2003).

[40] M. A. Katsoulakis and D. G. Vlachos, *Phys. Rev. Lett.* **84**, 1511 (2000).

[41] S. D. Collins, A. Chatterjee, and D. G. Vlachos, *J. Chem. Phys.* **129**, 184101 (2008).

[42] J. G. Dai, W. D. Seider, and T. Sinno, *J. Chem. Phys.* **128**, 194705 (2008).

[43] X. Liu, W. D. Seider, T. Sinno, *Phys. Rev. E* **86**, 026708 (2012)

[44] J. G. Dai, J. M. Kanter, S. S. Kapur, W. D. Seider, and T. Sinno, *Phys. Rev. B* **72**, 134102 (2005).

[45] J. Dal, W. D. Seider, and T. Sinno, *Mol. Simul.* **32**, 305 (2006).

[46] A. La Magna, S. Coffa, and L. Colombo, *Phys. Rev. Lett.* **82**, 1720 (1999).

[47] J. W. Kang, Y. G. Choi, J. H. Lee, S. H. Lee, and H. J. Oh, *Mol. Simul.* **35**, 234 (2009).

[48] A. Chatterjee and D. G. Vlachos, *J. Chem. Phys.* **124**, 064110 (2006).

[49] F. Wang and D. P. Landau, *Phys. Rev. Lett.* **86**, 2050 (2001).

[50] M. Prasad and T. Sinno, *Phys. Rev. B*, **68**, 045206 (2003).

[51] M. Prasad and T. Sinno, *Phys. Rev. B*, **68**, 045207 (2003).

[52] V. Vitek, *Computer Atomistic Modeling in Material Science*, Course Note. (2007).

Chapter 2

Coarse-Grained Lattice Metropolis Monte Carlo Models

2.1 Introduction

In this Chapter, we aim at developing a general coarse-grained Monte Carlo (CG-MMC) framework that extends spatial coarse-graining to a more general situation in which a continuous system of particles, subject to an arbitrary interaction potential, is mapped onto a rigid lattice of variable scale that can then be evolved with Metropolis Monte Carlo method using an appropriate coarse-grained potential. We require that the coarse-grained potential be thermodynamically consistent with the microscopic potential, i.e., that the entropy associated with the missing degrees-of-freedom is transparently embedded into the coarse-grained potential. This latter issue has not been addressed in previous spatial coarse-graining approaches [1-6] as discussed in Chapter 1.

The remainder of this chapter is organized as follows. In section 2.2, we start from developing the general CG-MMC framework by deriving equivalent coarse-grained partition function from the full-resolution partition function in Metropolis Monte Carlo model (MMC). Instead of applying a "matched" coarse-grained potential in previous coarse-graining approaches so that the coarse-grained partition function could reproduce the full-resolution partition function as well as possible, the CG-MMC framework developed in this thesis provides a clear demonstration on what the correct format of the coarse-grained potential should be. The significance is that the directly derived coarse-grained potential at a given temperature and coarse-graining level does not require any specific physical insight and theoretically can be applicable to any potential. In section 2.3, approaches to treat inter-particle interactions using basic numerical closure approximations are discussed as basic closure rule. How to calculate the coarse-grained interaction potentials using numerical averaging procedure is also fully discussed. The CG-MMC algorithm is summarized in detail in section 2.4, and the detailed discussion on detailed balance requirement in the CG-MMC model is presented in section 2.5. Applications of the CG-MMC model to atomic systems (represented by Lennard-Jones and square-well potentials) and molecular systems (represented by SPC-water potential) are demonstrated in section 2.6. Finally, conclusions are presented in sections 2.7.

2.2 General Concepts of CG-MMC Model

Consider a three-dimensional system of *N* particles within a cubic simulation box of length *L* subject to periodic boundary conditions and evolving within the canonical ensemble (constant *NVT*). Spatial coarse-graining proceeds by discretizing the overall domain into $M = m^3$ cubic coarse cells, each with length $L_{cell} = L/m$ and volume $V_{cell} = {L_{cell}}^3$. Figure 2.1(a) shows a two-dimensional example of the discretization.

Upon coarse-graining, each coarse cell is characterized by a single particle occupancy number, n_k, with $0 \le n_k \le n_{\max}$ and $N = \sum_{k=1}^{M} n_k$, as shown in Figure 2.1(b). The state of the coarse-grained system is now uniquely defined by an *M*-dimensional vector $\mathbf{n} \equiv \left(n_1, n_2, ..., n_M\right)$, which is generally much smaller than the full-resolution system state-space, which is of dimension 3*N* (in three-dimensional space).

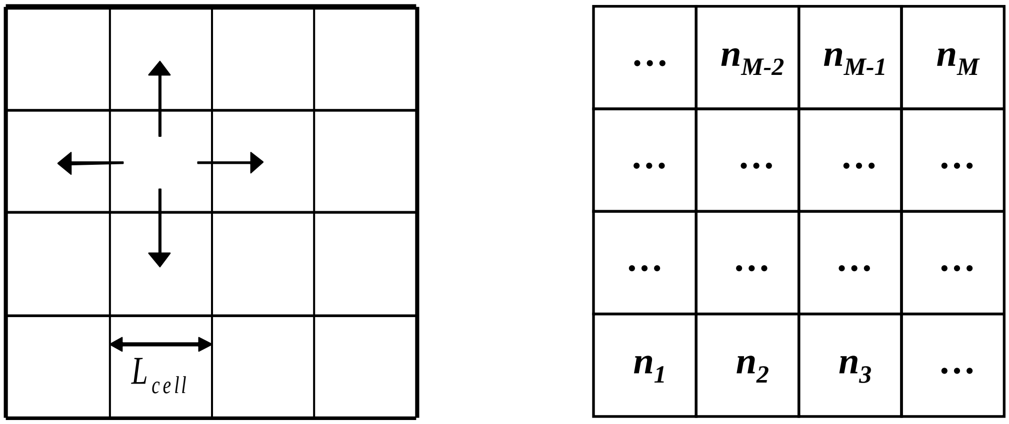

(a) (b)

Figure 2.1: (a) Discretization of a two-dimensional simulation domain into a square grid of coarse cells. Arrows denote neighbor cells to which particles can be moved. (b) *N* particles in the system are distributed over the *M* coarse cells. Each coarse cell is characterized by a single particle occupancy number n_k, $0 \le n_k \le n_{\max}$, satisfying $N = \sum_{k=1}^{M} n_k$.

The degree-of-freedom reduction implied by the spatial coarse-graining transformation is represented schematically in Figure 2.2.

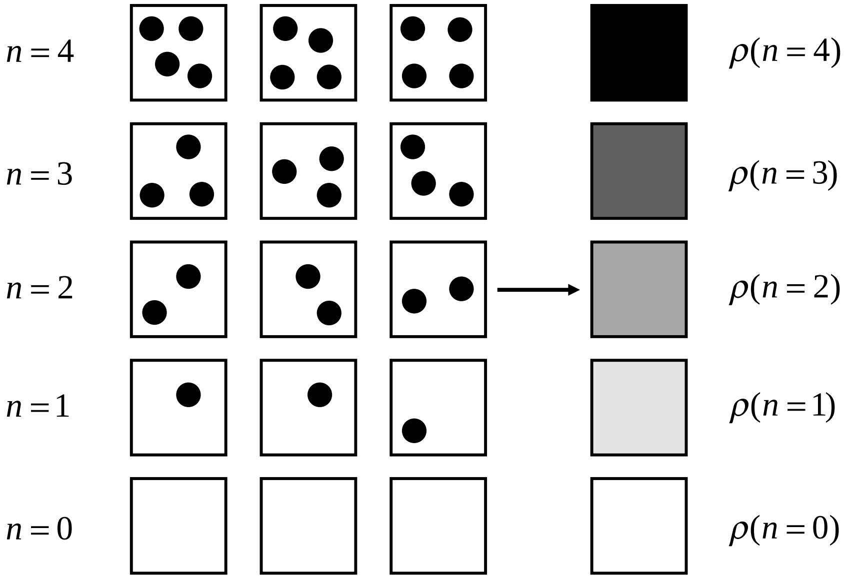

Figure 2.2: Multiple microstates associated with *n* particles in a coarse-cell are mapped onto a single coarse state within the coarse-grained representation, denoted by density, $\rho = n / V_{cell}$ or the particle occupancy number, *n*.

After defining the general nature of the spatial coarse-graining operation, the next step is to define the rules that govern particle moves between cells in the coarse-grained system, which are consistent with Metropolis Monte Carlo (MMC) moves in the continuous, fully-resolved system. In the following, we consider exclusively the canonical (*NVT*) ensemble. The coarse-graining transformation is derived by first considering the system-wide canonical partition function

$$Q(N,V,T) = \frac{1}{\Lambda^{3N} N!} \int \mathrm{d}\mathbf{r}^N \exp\left[-\frac{U(\mathbf{r}^N)}{k_B T} \right], \tag{2.1}$$

where $U(\mathbf{r}^N)$ is a specified interaction potential function. Rewriting the partition function in terms of sub-integrals over coarse cells, whereby the $N = \sum_{i=1}^{M} n_i$ particles in the system are distributed over the M coarse cells, gives

$$Q(N,V,T) = \frac{1}{\Lambda^{3N} N!} \sum_k \int \mathrm{d}\mathbf{r}^{n_1} \exp\left[-\frac{U(\mathbf{r}^N)}{k_B T}\right] \ldots \int \mathrm{d}\mathbf{r}^{n_M} \exp\left[-\frac{U(\mathbf{r}^N)}{k_B T}\right], \tag{2.2}$$

where the sum index k runs over all possible ways of distributing the N particles over the M coarse cells, i.e., all of the microstates of the coarse-grained system. Each of the sub-integrals in eq. (2.2) can be interpreted as a local Helmholtz free energy, i.e.,

$$Q(N,V,T) = \frac{1}{\Lambda^{3N} N!} \sum_k \exp\left(-\frac{A_1}{k_B T}\right) \ldots \exp\left(-\frac{A_M}{k_B T}\right), \tag{2.3}$$

where $A_k \equiv -k_B T \ln \int d\mathbf{r}^{n_k} \exp(-U(\mathbf{r}^N)/k_B T)$. There is no approximation implicit in the statement of eq. (2.3) beyond the central spatial coarse-graining assumption that the particles within each cell are in equilibrium. However, note that the local free energy of a given cell is, in general, a function of particle positions both inside (intra-cell interactions) and outside the cell (inter-cell interactions). How the inter-cell interactions are resolved depends on the specification of a closure rule, which does generally entail making an approximation; this will be addressed in Chapter 3.

Defining a coarse-grained overall system free energy, $A_{CG}(\mathbf{n}) = \sum_{k=1}^{M} A_k$, leads to a restatement of the system partition function:

$$Q_{CG}(N,V,T) = \frac{1}{\Lambda^{3N} N!} \sum_k \exp\left(-\frac{A_{CG}(\mathbf{n})}{k_B T}\right), \tag{2.4}$$

where $\mathbf{n} \equiv (n_1, n_2, ..., n_M)$ is an *M*-dimensional vector that defines a micro-configuration or state in the coarse-grained system (see Figure 2.1(b)). The "CG" subscript on the left-hand side simply denotes that the partition function is defined in terms of coarse variables. A schematic representing the action of the coarse-graining transformation on the potential energy landscape of the original system is shown in Figure 2.3. Both the dimensionality and the roughness (density of local minima per energy interval) are expected to be reduced in the coarse-grained system. Based on these considerations, it is reasonable to expect that the coarse-grained system would exhibit improved ergodicity and faster equilibration.

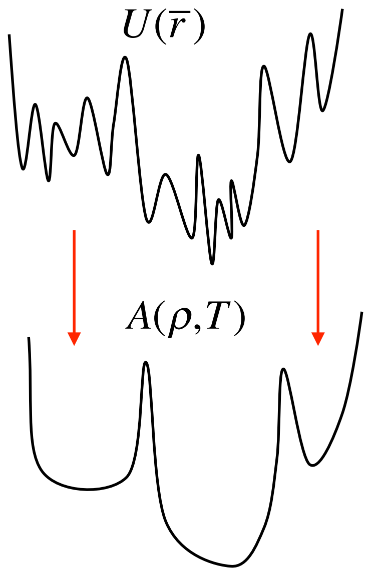

Figure 2.3: One-dimensional projection of energy landscape, $U(\bar{r})$, in fully-resolved system and corresponding CG (free energy) landscape, $A(\rho, T)$, in coarse-grained system with micro-configurational degrees-of-freedom implicitly captured.

Direct comparison of eqs. (2.1) and (2.4) suggests that a valid coarse-grained Metropolis Monte Carlo (CG-MMC) simulation proceeds identically to one on the original continuous system, except that the move acceptance criterion should be based on $\Delta A_{CG}(\mathbf{n})$ rather than $\Delta E(\mathbf{r}^N)$, i.e.,

$$\alpha_{ij} = \min\left[\exp\left(-\frac{\Delta A_{CG}(\mathbf{n})}{k_B T}\right), 1\right], \tag{2.5}$$

where α_{ij} is the acceptance probability for moving from state *i* to state *j*. Throughout the remainder of this Chapter, a CG-MMC "move" is restricted to the transfer of a single particle from one cell to a neighboring cell (see Figure 2.1(a)). More generalized moves (e.g., involving multiple particles) also will be discussed Chapter 5.

It is also worth noting that the spatial coarse-graining is generally applicable to systems of any geometry, as long as a unit coarse cell of an appropriate geometry exists such that the simulation domain can be discretized into an integer number of coarse cells that are space filling. In the remainder of this work, cubic cells are used to discretize rectangular simulation domains.

2.3. Coarse-Grained Potentials and Basic Closure Rules

The primary input needed to execute a CG-MMC simulation is $\Delta A_{CG}(\mathbf{n})$ in eq. (2.5), which represents the free energy change in the system upon moving from one microstate to another. In this sense, the function $\Delta A_{CG}(\mathbf{n})$ is a coarse-grained interaction potential that must be computed before a CG-MMC simulation can be performed. Ideally, the coarse-grained potential is obtained directly from a given full-resolution interaction potential (e.g., Lennard-Jones) with a minimum number of approximations and in a manner that is generalizable to any interaction model.

Consider first the Helmholtz free energy in a system containing *N* particles at volume *V* and temperature *T*:

$$\begin{aligned} A(N,V,T) &= -k_B T \ln Q \\ &= -k_B T \ln\left(\frac{V^N}{\Lambda^{3N} N!}\right) - k_B T \ln\left(\int dr^N \exp\left[-\frac{U\left(r^N\right)}{k_B T}\right]\right), \\ &\equiv A_{id}(N,V,T) + A_{ex}(N,V,T) \end{aligned} \tag{2.6}$$

where "*id*" and "*ex*" refer to ideal and excess contributions to the free energy, respectively. Similarly, the Helmholtz free energy *change* upon the addition of a particle to the system is given by

$$\begin{aligned} \Delta A(N \to N+1) &= -k_B T \ln Q_{N+1} / Q_N \\ &= -k_B T \ln\left(\frac{V/\Lambda^3}{N+1}\right) - k_B T \ln\left(\frac{\int dr^{N+1} \exp\left[-U\left(r^{N+1}\right)/k_B T\right]}{\int dr^N \exp\left[-U\left(r^N\right)/k_B T\right]}\right). \\ &\equiv \Delta A_{id}(N \to N+1) + \Delta A_{ex}(N \to N+1) \end{aligned} \tag{2.7}$$

The ideal contribution can be further decomposed so that

$$\Delta A_{id} = \Delta A_{id}^0 + k_B T \ln \rho \tag{2.8}$$

where ρ is defined as the density of the (*N+1*)-particle system and $\Delta A_{id}^0 \equiv k_B T \ln \Lambda^3$ is a reference term that only depends on temperature; the latter is not discussed further in the following considerations, since it is cancelled out when one particle is moved out of a cell and inserted to one of the neighboring cells, with the total number of particles unchanged. Note that one CG-MMC step always consists of one particle deletion (from an origination cell) and one particle insertion (in the destination cell).

While the ideal contribution to the particle insertion free energy change is immediately available for any microstate, the excess portion must be computed numerically (see eq. (2.8). However, it is generally the case that some assumptions must be imposed, in the form of a *closure rule*, to render this calculation computationally efficient; we address the central issue of closure approximation next.

Consider again the (Helmholtz) free energy change within a particular coarse cell due to the addition of one particle. The ideal contribution to the free energy change depends only on the intra-cell number density, ρ, and temperature, *T*. On the other hand, the excess contribution will depend on the densities of particles both inside and outside the cell, and possibly their spatial distributions. These functional dependencies are represented schematically by

$$\Delta A = \Delta A_{id}\left(\rho, T\right) + \Delta A_{ex}\left(\rho(r), \rho_{env}(r), T\right), \tag{2.9}$$

where $\rho_{env}(r)$ is the (spatially varying) number density in the environment surrounding the cell under consideration, and $\rho(r)$ explicitly accounts for any non-uniformity in the intra-cell density distribution. In eq. (2.9) and in the rest of the thesis, the "CG" subscript and the descriptor ($N \rightarrow N+1$) are dropped for clarity. Note that the free energy change associated with the addition of a single particle to a cell corresponds to the chemical potential in the limit of large particle number.

A full evaluation of the functional dependencies implied within eq. (2.9) would make computation of a coarse-grained interaction potential extremely cumbersome and negate any computational advantage of CG-MMC. The following closure approximations are therefore employed; these are subject to *a posteriori* verification once the results of the coarse-grained simulations are compared to reference, full-resolution predictions. First, the extent of the “environment” is assumed to be localized around the coarse cell in question and the density distribution within the environment is assumed to be coupled only to that in the central coarse cell. Second, the density distributions within the coarse cell and the environment are assumed to be fully characterized by their respective overall densities. In other words, any spatial variations in the density distributions are averaged and only captured implicitly. With these closure rule simplifications, eq. (2.9) simplifies to

$$\Delta A = \Delta A_{id}\left(\rho, T\right) + \Delta A_{ex}\left(\rho, \rho_{env}, T\right), \tag{2.10}$$

Equation (2.10) suggests that a full pre-computation of the coarse-grained interaction function would require a three-dimensional scan over all relevant combinations of ρ, ρ_{env}, and *T*, even if the closure approximations noted above are assumed. The coarse-grained potential also is likely to be a function of coarse-graining level, i.e., the coarse cell size, necessitating additional calculations for multiresolution simulations. These considerations highlight the potentially significant overhead associated with coarse-grained potential evaluation. Additional closure approximations are introduced in Chapter 3, beyond the base case ones described above, in order to greatly reduce the expense associated with coarse-grained potential calculations, while retaining the accuracy of the overall CG-MMC method.

To compute the excess free energy change for particle insertion (or deletion) as a function of number density and temperature, a test simulation cell is constructed as a cubic central coarse cell with width L_{cell} embedded in a surrounding environment shell with width L_{env}, as shown in Figure 3(a). The outer boundaries of the environment shell are subject to standard periodic boundary conditions. The boundary between the coarse cell and the environment shell is reflective in order to constrain the particle number densities in both regions to desired values; note, however, that particles are allowed to interact normally across this boundary. In this manner, it is possible to compute the free energy change for particle insertion for all combinations of (ρ, ρ_{env}).

Special care must be taken in the case of molecular species. Constraining entire molecules to either side of the partition would lead to configurational exclusion effects because the molecular center-of-mass would only able to reach the boundary for certain molecular configurations. Hence, for molecular entities, only the molecular center-of-mass is constrained to lie within a given region while portions of the molecules are allowed to cross. This restricted reflective boundary condition is denoted schematically in Figure 2.4(b) for the case of small molecules such as water. It should be noted that restriction of the center-of-mass, rather than the entire molecule, relaxes the imposed density constraint somewhat, particularly when there is a large density difference between the reference coarse cell and its surroundings. The impact of this issue is probed in more detail in Chapter 3.

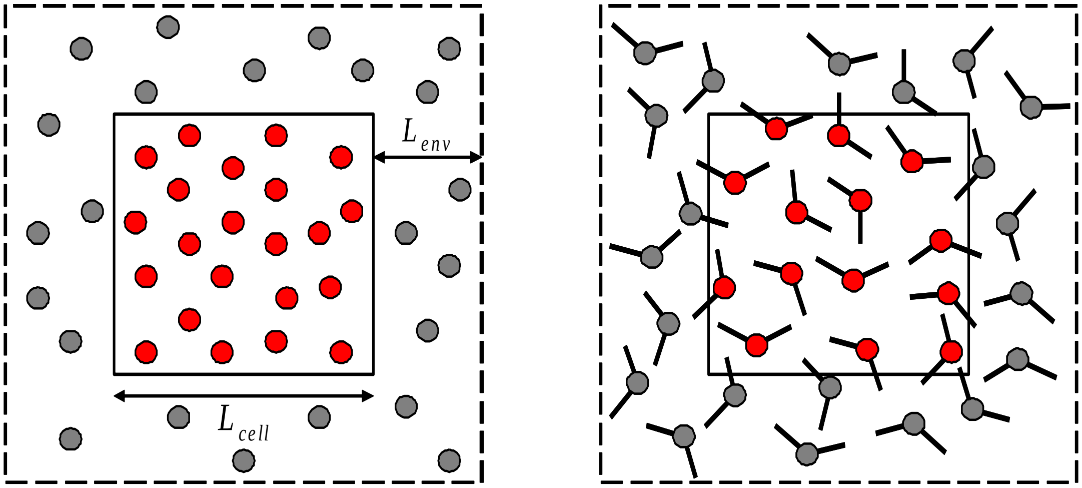

(a) (b)

Figure 2.4: Cell setup for computing coarse-grained interaction potential for (a) atomic systems, and (b) molecular systems. In both cases, an inner cell (solid line) is surrounded by an "environment" shell subject to periodic boundary conditions (dashed line). In (a), particles are not allowed to move between the two regions during free energy sampling but do interact across the partition, while in (b) only the centers-of-mass are restricted.

In this thesis, the excess free energy change due to particle insertion in Eq. (2.10) is directly computed using the Widom particle insertion method [7], although any other method for free energy estimation also can be employed. We note here that the basic Widom method is problematic under a variety of common conditions, such as high densities, low temperatures and for large molecular entities. Many studies have demonstrated that the Widom approach can be improved substantially in most of these situations, but these are not considered here because it was possible to obtain convergence for all conditions of interest. Of course, the computational expense associated with the pre-computation of the coarse-grained potential would be reduced with more advanced techniques.

In the basic Widom particle insertion method, the excess free energy change due to particle insertion is given by

$$\Delta A_{ex}(N \rightarrow N+1) = -k_B T \ln \int \mathrm{d}\mathbf{r}^{N+1} \left\langle \exp\left(-\frac{\Delta U}{k_B T} \right) \right\rangle_{N,T}, \qquad (2.11)$$

where $\Delta U = U(r^{N+1}) - U(r^N)$ is the internal energy change due to the insertion of the $(N+1)^{\mathrm{th}}$ particle, and the averaging is carried out in the trajectory generated by the N-particle system at the temperature of interest. Note that test particle insertions are performed only within the center cell although the corresponding potential energy change is computed over all particles. Unless otherwise stated, a Widom insertion simulation for a given (ρ, ρ_{env}, T) combination consisted of a pre-equilibration phase (~10^6 MC sweeps over all particles in the simulation cell) followed by about 10^6 MC sweeps to collect the average in eq. (2.11). In detail, during the pre-equilibration phase, $5\text{x}10^7$ MC steps for LJ and SW cases, and $2.5\text{x}10^8$ MC steps for SPC case are performed over all particles in the simulation cell. During the collection phase, $5\text{x}10^7$ steps for LJ and SW cases and $7.5\text{x}10^7$ MC steps for SPC case are performed to collect the average in eq. (2.11). Configurations taken every 2500 MC steps were used to perform 100 test insertions for LJ and SW cases, and 250 test insertions for SPC case. The procedure is repeated across a range of center cell and environment particle densities and temperatures; the final result is a multidimensional surface of excess free energy differences that, along with the ideal contribution (eq. 2.8), defines the coarse-grained potential. In many cases, the Widom simulation was repeated multiple times in order to reduce the statistical uncertainty associated with the estimated free energy at that (ρ, ρ_{env}, T) combination.

2.4 The CG-MMC Algorithm

Based on the theoretical derivation of CG-MMC model discussed in section 2.2, the CG-MMC simulation algorithm proceeds as follows:

1) Start from an initial state i_0 represented by the M-dimensional vector $\mathbf{n}(i_0) \equiv (n_1, n_2, ..., n_M)$ in the phase space of the coarse-grained system.

2) Given an initial coarse state i generate randomly a new state j with probability a_{ij}. This is done by randomly selecting a coarse cell k and one of its six adjacent cells l, both with equal probability. If cell k is not empty, i.e. $n_k > 0$ and cell l is not at the maximum occupancy, i.e. $n_l < n_{\max}$, move one particle from cell k to l. Otherwise re-select cell k or l until both meet the occupancy requirements. The state of the system then changes from $\mathbf{n}(i) \equiv (n_1, n_2, ...n_k, ...n_l, ..., n_M)$ to $\mathbf{n}(j) \equiv (n_1, n_2, ...(n_k - 1), ...(n_l + 1), ..., n_M)$.

3) Evaluate the change of free energy due to the particle move. This is accomplished by decomposing the move into a particle removal and particle insertion subprocess. The particle deletion process is defined in terms of a particle insertion process, as shown in the following equations for both the ideal and excess free energy changes.

$$\Delta A_{id}\left(n_l \to n_l+1\right) = \Delta A_{id}^0 - k_B T \ln\left(\frac{V/\Lambda^3}{n_l+1}\right), \tag{2.12}$$

$$\Delta A_{ex}\left(n_l \to n_l+1\right) = \Delta A_{\text{input}}\left(n_l, n_{env,l}\right), \tag{2.13}$$

$$\Delta A_{id}\left(n_k \to n_k-1\right) = -\Delta A_{id}\left(n_k-1 \to n_k\right) = -\Delta A_{id}^0 + k_B T \ln\left(\frac{V/\Lambda^3}{n_k}\right), \tag{2.14}$$

$$\Delta A_{ex}\left(n_k \to n_k-1\right) = -\Delta A_{ex}\left(n_k-1 \to n_k\right) = -\Delta A_{\text{input}}\left(n_k-1, n_{env,k}\right), \tag{2.15}$$

Summing up the four free energy change contributions in eqs. (2.12-2.15) gives the free energy change associated with the transition from state i to j:

$$\Delta A\left(i \to j\right) = k_B T \ln\frac{n_l+1}{n_k} + \Delta A_{\text{input}}\left(n_l, n_{env,l}\right) - \Delta A_{\text{input}}\left(n_k-1, n_{env,k}\right), \tag{2.16}$$

where the free energy is decomposed into ideal contribution and excess contribution as discussed before. The excess contribution is provided by the input CG potential denoted as $\Delta A_{\text{input}}\left(\rho_k, \rho_{env,k}\right)$ representing the change of free energy by inserting one particle to a coarse cell with density ρ_k and environment density $\rho_{env,k}$ as shown in eq. (2.11), where the density and the number of particles as occupancy are used interchangeably. Here we use ΔA_{input} (as a function of ρ_k and $\rho_{env,k}$) to represent the excess change of free energy with the subscript ‘input’ instead of specifying it is due to one particle insertion for simplicity, also to highlight the fact that the numerically averaged CG potential is the only input in the CG-MMC model.

4) Accept this move with probability α_{ij}, where

$$\alpha_{ij} = \min\left[\exp\left(-\beta\Delta A(i \rightarrow j)\right), 1\right]. \tag{2.17}$$

This is realized by generating a random number ζ such that $0 \le \zeta \le 1$. If $\alpha_{ij} < \zeta$, then remain in old state i; If $\alpha_{ij} \ge \zeta$, then accept the new state j;

5) The CG-MMC iterations continue by repeating steps 2-4.

2.5 Detailed Balance in the Coarse-Grained Representation

Detailed balance simply means at equilibrium, each elementary process should have an equivalent reverse process, i.e.

$$\pi_i a_{ij} \alpha_{ij} = \pi_j a_{ji} \alpha_{ji}, \tag{2.18}$$

where π_i is the probability of staying in state *i* and π_j is the probability of staying in state *j*. However, detailed balance is an overly strict condition to ensure a valid Monte Carlo simulation. A substantially weaker condition called “the balance condition” is actually the necessary and sufficient fundamental requirement [8]. Nonetheless, it is usually more convenient to set up the algorithm by maintaining the stronger than necessary requirement (i.e. detailed balance) [9].

Now, eq. (2.4) indicates that the equilibrium probability for being in state *i* is given by

$$\pi_i = \exp(-A_i / k_B T) / Q_{CG}(N,V,T). \tag{2.19}$$

It is straightforward to show that detailed balance is readily satisfied in a CG-MMC simulation by the application of eq. (2.5), provided that particle moves are selected appropriately.

Given that $\alpha_{ij} = \min\left[\pi_j / \pi_i, 1\right]$, there are two conditions to consider:

If $\pi_i < \pi_j$, $\alpha_{ij} = 1$ and $\alpha_{ji} = \pi_i / \pi_j$, then eq. (2.18) becomes

$$a_{ij} = a_{ji}. \tag{2.20}$$

Otherwise if $\pi_i \geq \pi_j$, $\alpha_{ij} = \pi_j / \pi_i$ and $\alpha_{ji} = 1$, eq. (2.18) also becomes eq. (2.20), i.e. $a_{ij} = a_{ji}$.

Detailed balance implies that the probability of changing from state i to state j, denoted a_{ij}, follows uniform distribution. Therefore to satisfy the detailed balance criterion, we follow uniform distribution to select beginning and ending states *i* and *j* in each CG-MMC move. In practice, each origination coarse cell *k* and each one of its six destination adjacent cells *l* is selected with equal probability, which is exactly how our CG-MMC algorithm is implemented.

In other words, for detailed balance to be satisfied in a CG-MMC simulation, coarse cells from which particles are selected to be moved should be picked at random. Consequently, selecting origination coarse cells in a way that is biased by the number of particles they contain would be inconsistent with detailed balance and lead to the incorrect equilibrium condition. The implications of random versus biased cell selection on system evolution under non-equilibrium conditions (i.e., *dynamics*) will be discussed in Chapter 4.

2.6 Results and Discussion

In this section we present and discuss results obtained using the base-case closure model (see Section 2.3), which will serve as a reference for results obtained with the additional closure rule approximations we introduce later in the next chapter. We consider three interatomic potentials: (1) the Lennard-Jones (LJ) potential for argon (2) the square-well (SW) potential with two different parameterizations, and (3) the spherical point charge (SPC) potential for water [10, 11] which demonstrates the applicability of CG-MMC to molecular systems. These potentials are given by:

1 – LJ ($r_c = 2.5\sigma, \sigma = 3.405$ Å, $\varepsilon / k_B = 119.8$ K):

$$U(r_{ij}) = \begin{cases} 4\varepsilon\left[\left(\frac{\sigma}{r_{ij}}\right)^{12} - \left(\frac{\sigma}{r_{ij}}\right)^{6}\right], & r_{ij} \le r_c \\ 0, & r_{ij} > r_c \end{cases} \tag{2.21}$$

2 – SW ($\lambda = 1.5$ or 1.25):

$$U(r_{ij}) = \begin{cases} \infty, & r_{ij} < \sigma \\ -\varepsilon, & \sigma \le r_{ij} < \lambda\sigma \\ 0, & r_{ij} > \lambda\sigma \end{cases} \tag{2.22}$$

3 – Water ($r_c = 7.75$ Å, $\sigma = 3.1655$ Å, $\varepsilon = 0.15542$ kcal/mol, $q_H = 0.41$, $q_O = -0.82$ electrons):

$$U(r_{ij}) = \begin{cases} 4\varepsilon\left[\left(\frac{\sigma}{r_{ij}}\right)^{12} - \left(\frac{\sigma}{r_{ij}}\right)^{6}\right] + \frac{q_i q_j e^2}{r_{ij}}, & r_{ij} \le r_c \\ 0, & r_{ij} > r_c \end{cases} \tag{2.23}$$

where the LJ portion in eq. (2.21) applies only between oxygen atoms. Note that the electrostatic interaction term in the SPC potential used here was spherically truncated without correction at 7.75 Å. Although this truncation leads to various errors, the resulting VLE phase diagram has been shown to be only slightly affected [11]. CG-MMC compatible approaches for correcting the effects of truncation include the reaction field [12] and Wolf summation [13] methods but these are not implemented in this work. The latter, in particular, has recently been shown to offer advantages over other methods because of its computational efficiency and applicability to inhomogeneous and finite systems.

Base case results are presented using coarse-grained potentials computed with coarse cells of size $L_{cell} = 3\sigma$ and $L_{env} = 1.5\sigma$. These dimensions ensure that each coarse cell is larger than the potential cutoff, and therefore that particles only interact with other particles in neighboring coarse cells. The results are only weakly influenced by the exact thickness of the environment shell as long as the shell thickness is sufficiently large to capture important multi-particle configurations. The value of L_{env} was chosen based on a compromise between convergence with respect to the environment shell thickness and computational expediency. At the $L_{cell} = 3\sigma$ coarse-graining level, a coarse-cell typically contains up to about 25 LJ or SW atoms and 30 water molecules.

Figures 2.5, 2.6 and 2.7 show the excess free energy change for single particle insertion as a function of (ρ, ρ_{env}) at two different temperatures for each of the three potential models, LJ-argon, SW, and SPC-water, respectively. In the following sections, reduced units are employed for the LJ-argon (see Figure 2.5) and SW (see Figure 2.6) cases ($T^* \equiv k_B T / \varepsilon,\ \rho^* \equiv \rho\sigma^3$), while dimensional quantities are used for SPC-water (see Figure 2.7). It is again emphasized that the excess free energy change for particle insertion corresponds to the excess chemical potential in the limit of large N. Each of the spherical symbols in Figures 2.5, 2.6 and 2.7 corresponds to the results of one or more Widom insertion simulations at a given density combination, while the color-field surfaces are 3rd-order (per dimension) polynomial fits to the simulation data. The number of Widom insertion simulations at each density combination was determined by requiring that the uncertainty (as defined by one standard deviation divided by the average) at each point was no larger than 0.15 (except for data points with very small average approaching 0). While the overall computational effort associated with the pre-calculation of the coarse-grained potential can be significant, it is trivially distributable over an arbitrary number of processing units. More detailed analysis of computational effort and related closure approximations will be discussed in the next Chapter.

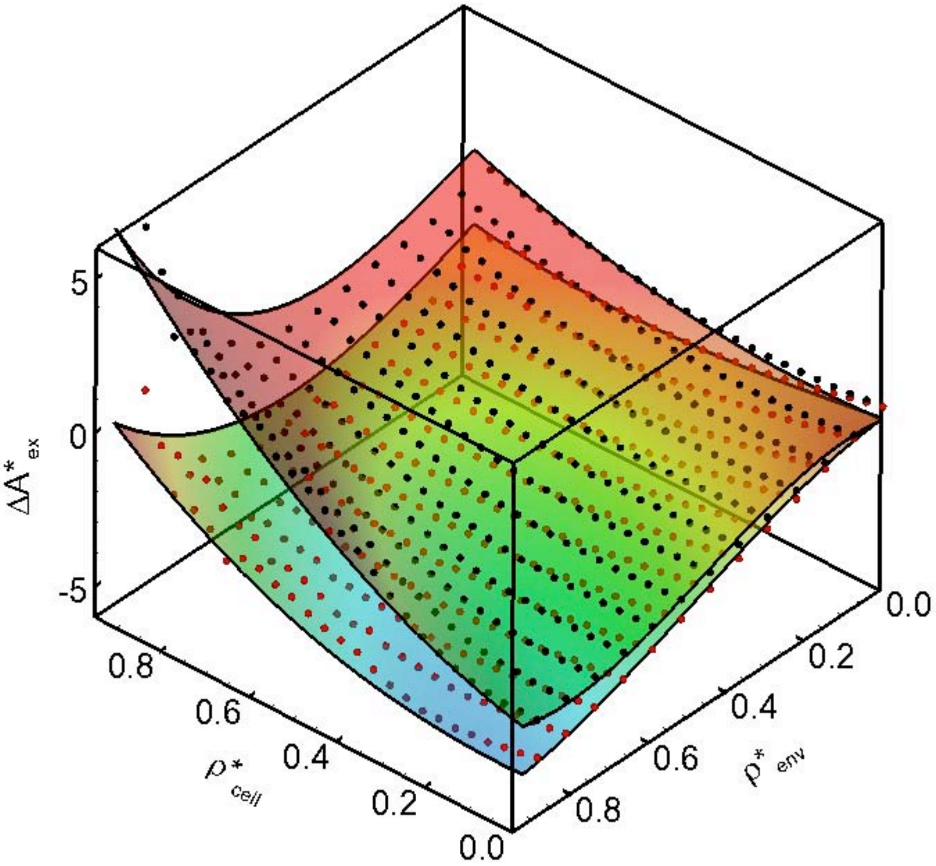

Figure 2.5: Excess free energy change for particle insertion computed for LJ potential for argon at $T^* = 0.8, 1.3$, as a function of cell and environment densities. Reduced units are used for LJ-argon. Coarse cell length (L_{cell}) is 3σ, environment shell thickness (L_{env}) is 1.5σ. Symbols – Widom insertion simulations (black spheres represent the higher temperature); color field contours – polynomial interpolation.

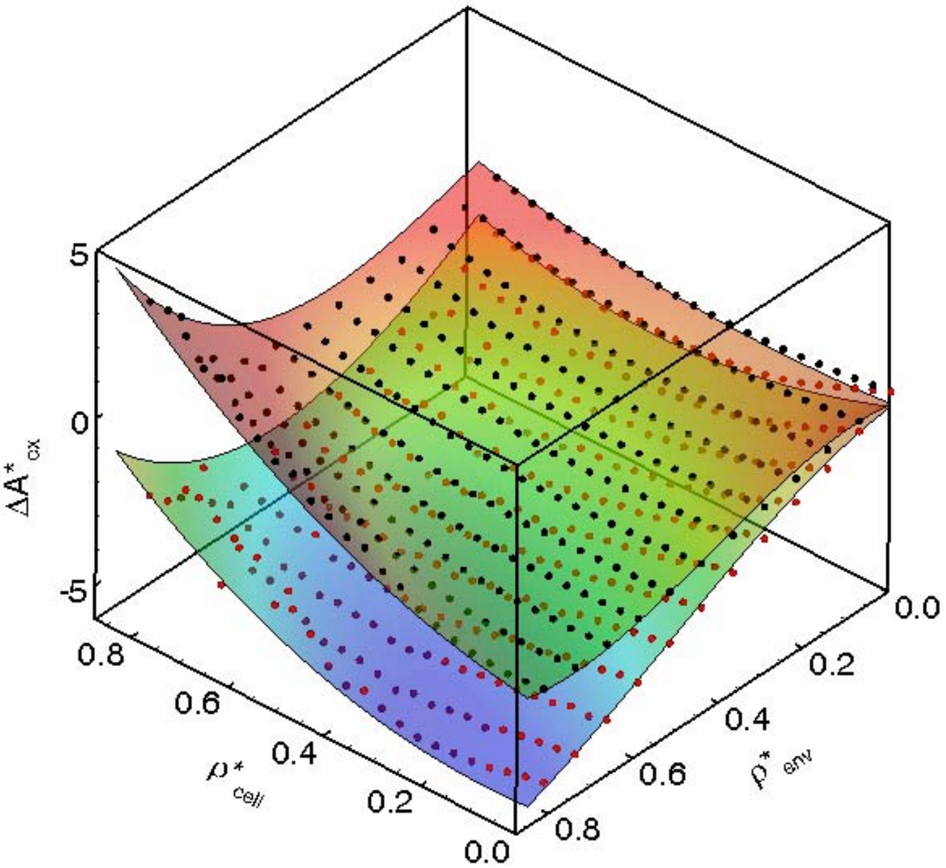

Figure 2.6: Excess free energy change for particle insertion computed for square-well potential with $\lambda = 1.5$ at $T^* = 0.9, 1.4$, as a function of cell and environment densities. Reduced units are used for SW potential. Coarse cell length (L_{cell}) is 3σ, environment shell thickness (L_{env}) is 1.5σ. Symbols – Widom insertion simulations (black spheres represent the higher temperature); color field contours – polynomial interpolation.

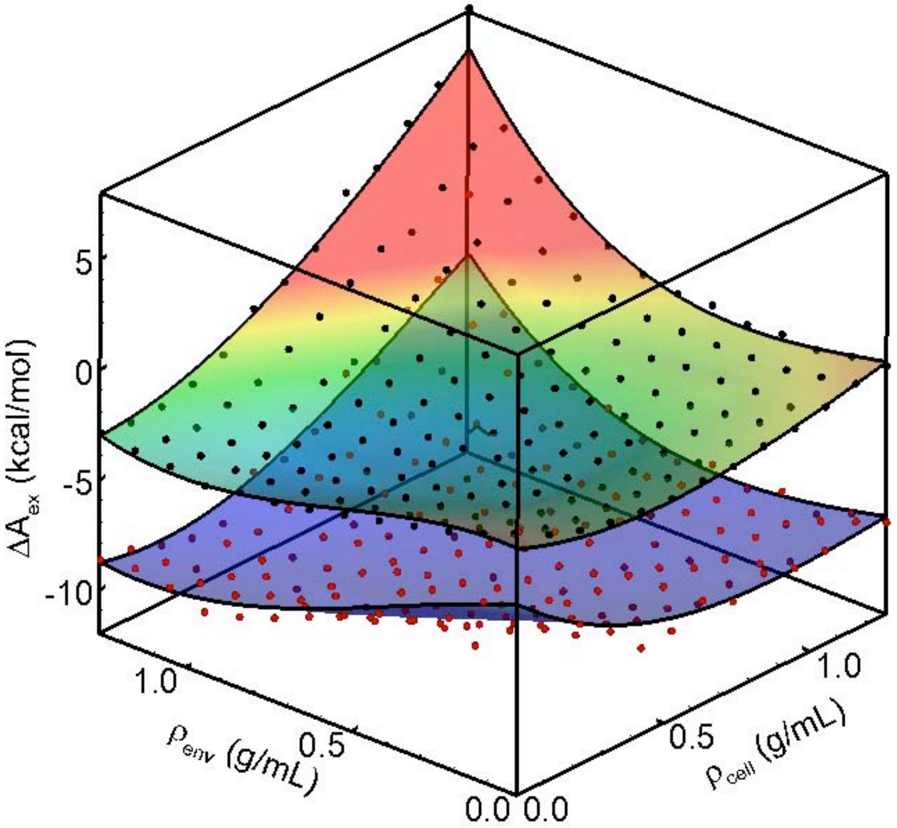

Figure 2.7: Excess free energy change for particle insertion computed for SPC potential for water at $T = 298\,K$, $600\,K$, as a function of cell and environment densities. Dimensional quantities are reported for SPC-water. Coarse cell length (L_{cell}) is 3σ, environment shell thickness (L_{env}) is 1.5σ. Symbols – Widom insertion simulations (black spheres represent the higher temperature); color field contours – polynomial interpolation.

The excess chemical potential fields shown in Figures 2.5 for LJ-argon, 2.6 for SW and 2.7 for SPC-water were then used to generate VLE phase diagrams for the three systems. At each temperature, a CG-MMC simulation cell consisting of 10^3 coarse cells was first initialized with a uniform density, ($\rho^* = 0.3$ for LJ, $\rho^* = 0.3$ and $\rho^* = 0.4$ for SW $\lambda = 1.5$ and 1.25 respectively, and $\rho = 0.3$ g/ml for SPC) and then allowed to evolve at a specified temperature. Particle moves were executed by picking a random origin and neighboring destination cell pair and computing the free energy change due to moving a particle across the cell pair according to eq. (2.20). Note again that a single CG-MMC step consists of one particle deletion and one particle insertion. The total free energy change was computed using a combination of the excess data in Figures 2.5 for LJ-argon, 2.6 for SW and 2.7 for SPC-water and the ideal contribution in eq. (2.8). The move acceptance was determined on the basis of eq. (2.5). Equilibration of the CG-MMC simulation was assessed by monitoring the total coarse-grained free energy.

Snapshots of example near-equilibrium configurations at three different overall system densities of the LJ system are shown for CG-MMC and full-resolution MMC simulations in Figure 2.8. The coarse-grained simulations (a system of size $180 \times 180 \times 180\ \sigma^3$) show very clearly the liquid-vapor phase boundaries, and also explicitly highlight the density fluctuations within each phase. Note that the full-resolution systems are represented by much smaller simulation cells (a system of size $36 \times 36 \times 36\ \sigma^3$) because of the computational expense required to reach equilibrium (lower row in Figure 2.8). As a result, the liquid-vapor phase boundaries are much less clearly delineated than in the CG-MMC snapshots and cannot be accurately located by direct visual inspection. OVITO [14] is used for snapshots in all cases through this thesis.

Detailed discussion of the computational advantages of CG-MMC is provided in Chapter 3. Here, we briefly note that the CG-MMC simulations reach equilibrium in far fewer Monte Carlo move attempts per particle than the full resolution simulations, primarily because the (successful) moves in the coarse-grained system are much larger. Moreover, the computational cost associated with each move, on a per-particle basis, is lower in the CG-MMC case due to the simplicity of the numerically tabulated potential. Overall, for $L_{cell} = 3\sigma$, and for the cases considered here, the CG-MMC simulation reaches equilibrium about 10^6 times faster than a similarly-sized full-resolution system.

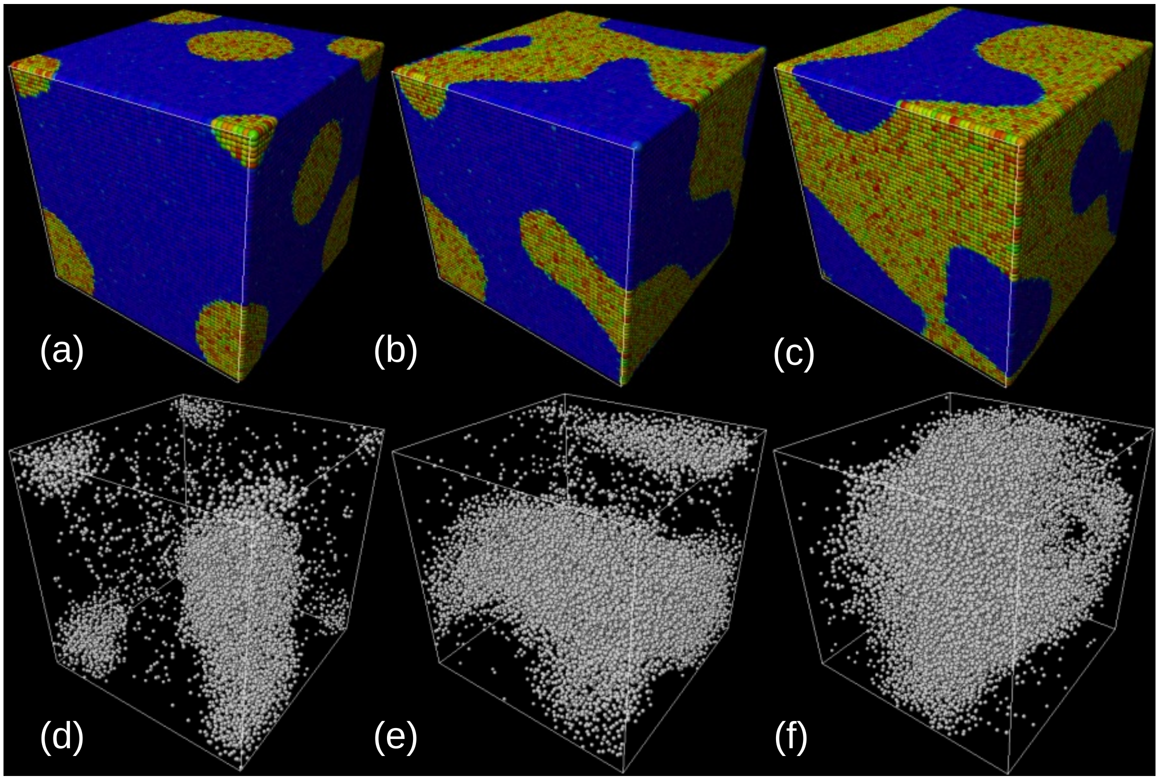

Figure 2.8: Top row: Equilibrium snapshots of LJ CG-MMC simulation configurations at (a) $\rho^* = 0.15$, (b) $\rho^* = 0.3$, and (c) $\rho^* = 0.45$. System size is $180 \times 180 \times 180\ \sigma^3$ with $L_{cell} = 3\sigma$. Cell color denotes particle number that ranges from zero (dark blue) to 24 (red). Bottom row (d-f): Corresponding full resolution MMC simulation snapshots for a system size of $36 \times 36 \times 36\ \sigma^3$.

Example near-equilibrium configurations for the SPC-water systems are shown in Figure 2.9 for both coarse-grained and full-resolution systems.

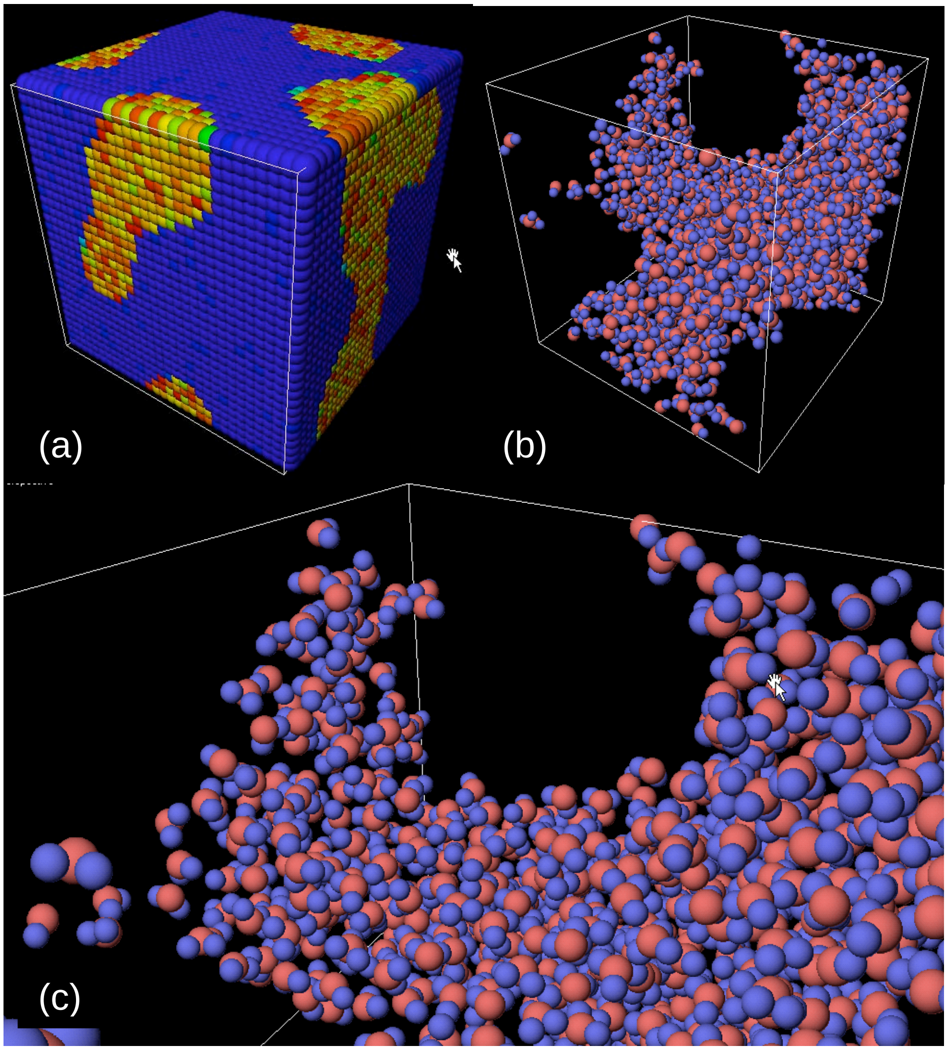

Figure 2.9: (a) Equilibrium snapshots of SPC-water CG-MMC simulation configurations at $T = 400\,K$ and $\rho = 0.3$ g/ml. System size is $90 \times 90 \times 90\sigma^3$ with $L_{cell} = 3\sigma$. Cell color denotes atom or molecule number that ranges from zero (dark blue) to about 30 (red). (b) Corresponding full resolution MMC simulation snapshots for a system size of

$15 \times 15 \times 15\sigma^3$. (c) A zooming in configuration of water molecules from a corner in full resolution MMC simulation.

At each temperature, the location of the VLE phase boundaries was determined using histograms of the equilibrium distribution of cell densities. Examples of equilibrated cell density distributions for LJ-argon and SPC-water potentials are shown in Figures 2.10 and 2.11 respectively for $L_{cell} = 3\sigma$. In both cases, peaks corresponding to the liquid and vapor phases are clearly visible; intermediate densities correspond to interfacial regions. For the LJ case (Figure 2.10), corresponding density histograms obtained from full-resolution simulations also are shown for comparison; these were computed by subdividing the full-resolution simulation cell into coarse cells and histogramming the density distribution. About 250 equilibrated (phase separated) configurations were captured and gridded into coarse cell lattices, which were then used to collect density distribution data. Each configuration was gridded 100 times using a randomly selected origin to improve the density distribution statistics.

For $\rho^* = 0.6,\ T^* = 1.1$, which lies outside the two-phase envelope, a single broad peak is observed and the agreement between the CG-MMC and full-resolution MMC is essentially perfect. At $\rho^* = 0.3,\ T^* = 0.8$, which lies inside the envelope, the distributions are bimodal corresponding to distinct vapor and liquid phases. Here, the agreement is excellent across the peaks corresponding to the two phases, but an apparent discrepancy is present in the intermediate region ($0.1 < \rho^* < 0.5$). In particular, the full-resolution MMC simulation exhibits a higher number of cells with densities inside the phase envelope, while the CG-MMC shows the expected overlap between two parabolic distributions. Note that the probability of cells with intermediate particle density ($0.15 < \rho < 0.55$) is artificially enhanced by the logarithmic axes used in Figure 2.10. The source of the discrepancy is the fact that in CG-MMC, interfacial regions between the liquid and vapor naturally align with the underlying cell discretization, whereas this effect is not present in the *a posteriori* coarse-graining performed on the full-resolution particle coordinates. There is no obvious method to account for this effect just at the phase boundary locations in the a posteriori coarse-graining operation.

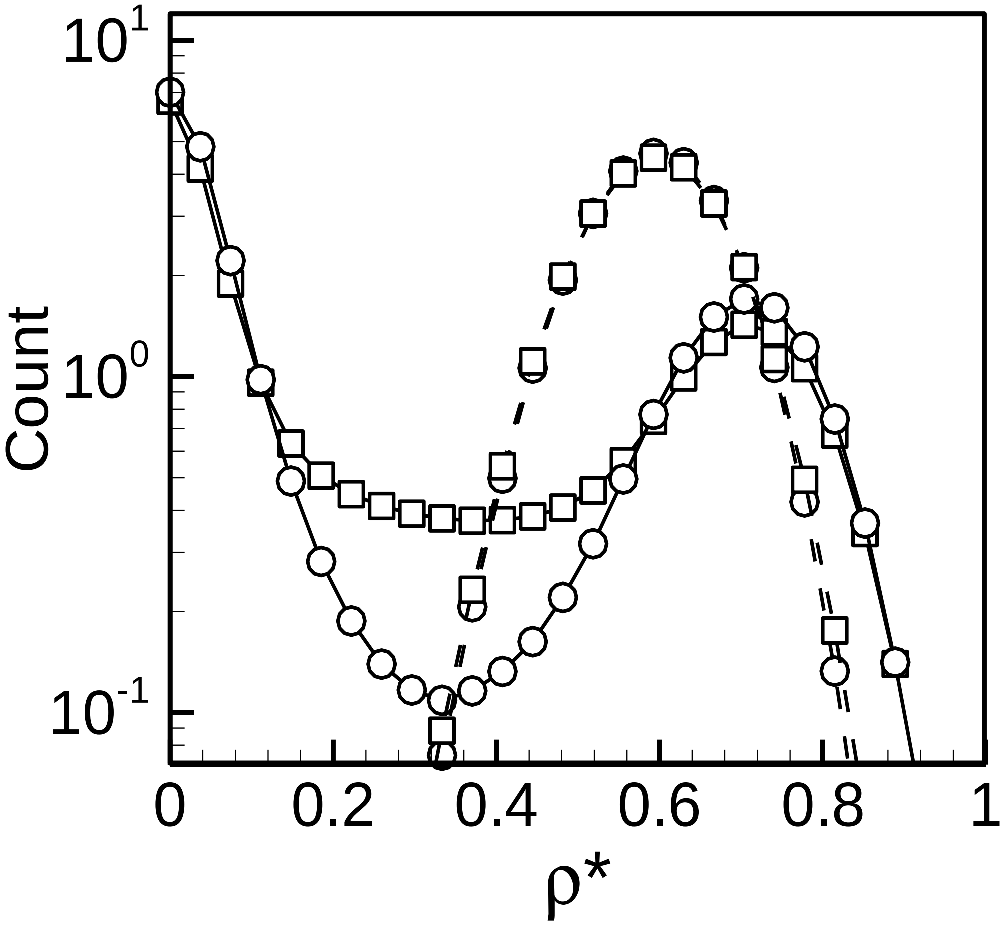

Figure 2.10: Area-normalized cell density histogram for LJ-argon from equilibrated CG-MMC simulations with $L_{cell} = 3\sigma$. Circles – CGMMC, squares – full-resolution MMC; solid lines – $\rho^* = 0.3,\ T^* = 0.8$, dashed lines – $\rho^* = 0.6,\ T^* = 1.1$.

This discretization discrepancy notwithstanding, the density histograms show that (1) the CG-MMC captures accurately the details of the density distribution in both single and multiphase cases, and (2) the average densities corresponding to each phase can be unambiguously extracted from CG-MMC simulations. Note, however, that as the peaks become broader and closer to each other at higher temperatures (Figure 2.11), the precise location of each peak becomes more difficult to define.

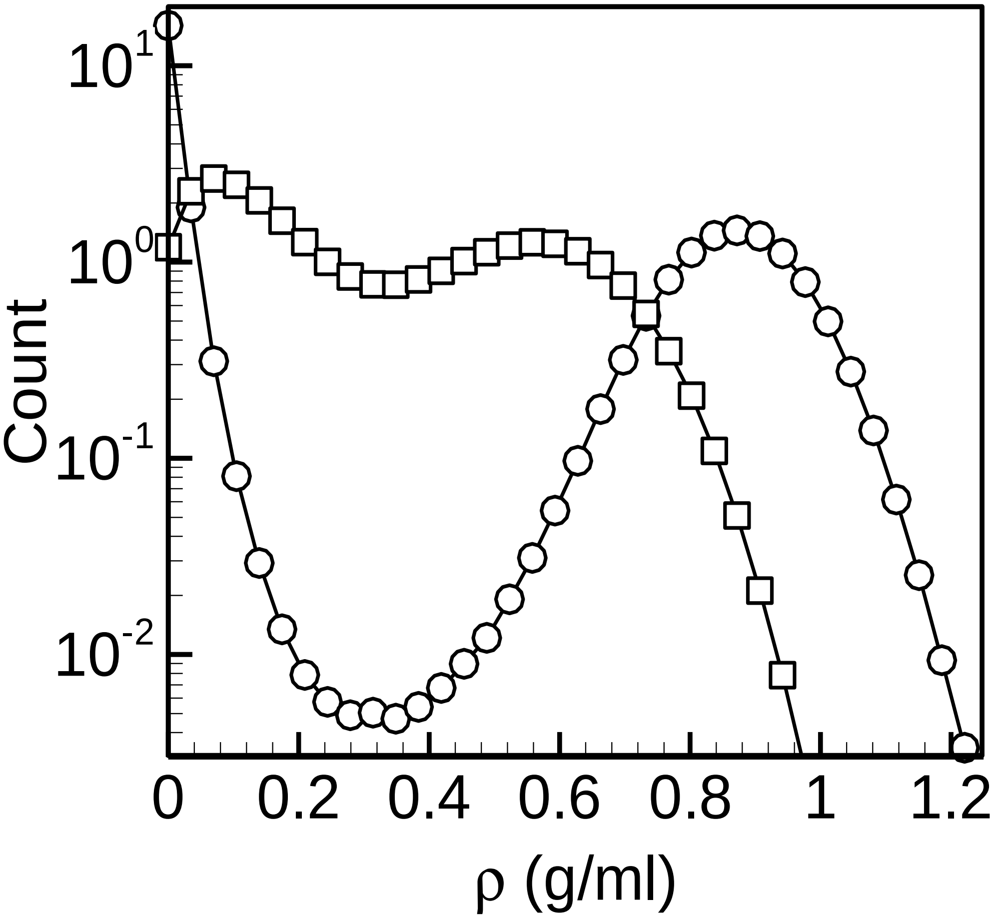

Figure 2.11: Area-normalized cell density histogram for SPC-water obtained from equilibrated CG-MMC simulations with $L_{cell} = 3\sigma$. Circles – $\rho = 0.3$ g/ml, $T = 400$ K; squares – $\rho = 0.3$ g/ml, $T = 580$ K.

For atomic systems, shown in Figures 2.12 and 2.13 are $T-\rho$ VLE envelopes obtained for the LJ and SW potentials using CG-MMC with cells of size $L_{cell} = 3\sigma$. Also shown in Figure 2.12 are LJ results using larger cells ($L_{cell} = 4\sigma$ and 6σ). For molecular systems, the $T-\rho$ VLE envelopes SPC-water are shown in Figure 2.13 at a coarse-graining level of $L_{cell} = 3\sigma$. Also shown for each case (with gray-filled circles) are the corresponding VLE envelopes predicted by full-resolution simulation based on the Gibbs-ensemble Monte Carlo (GEMC) method [11, 15, 16]. The agreement is generally very good for all three potentials, with the primary deviation observed near the critical points. The potential source of the deviation is probed by considering additional LJ calculations in which the coarse-graining level is increased to $L_{cell} = 4\sigma$ (open diamonds) and 6σ (open circles). While the prediction of the critical point is not significantly changed at $L_{cell} = 4\sigma$, the results are notably improved for $L_{cell} = 6\sigma$, with almost perfect agreement across the entire VLE envelope.

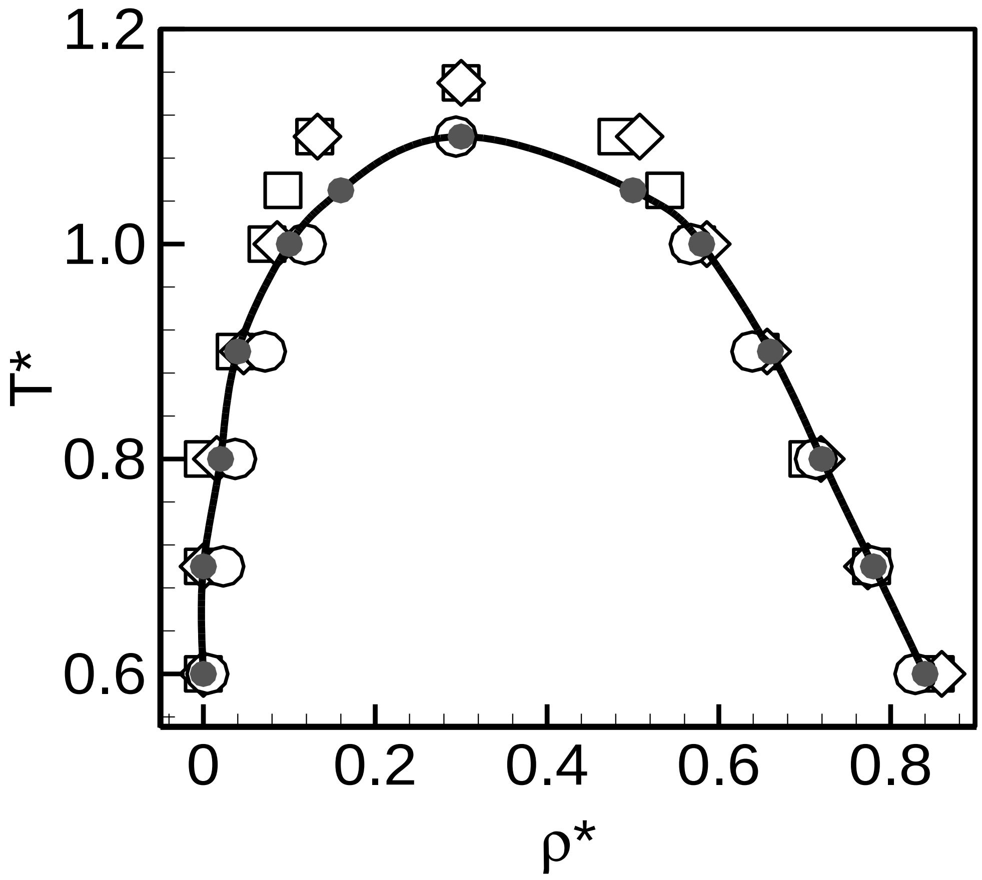

Figure 2.12: VLE phase envelopes for LJ-argon. Open squares – CG-MMC with $L_{cell} = 3\sigma$, open diamonds – CG-MMC with $L_{cell} = 4\sigma$, open circles – CG-MMC with $L_{cell} = 6\sigma$, gray filled circles – full resolution GEMC [11].

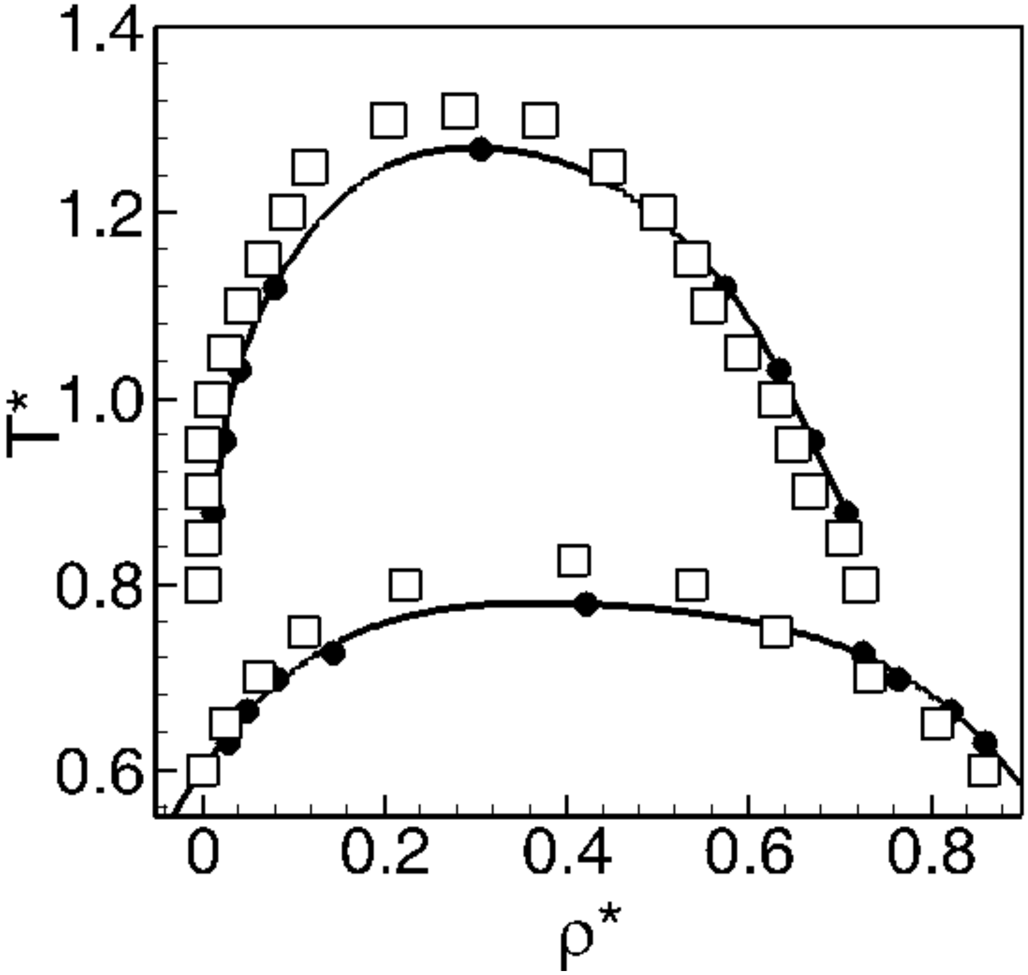

Figure 2.13: VLE phase envelopes for SW (top: $\lambda = 1.5$, bottom: $\lambda = 1.25$). Open squares – CG-MMC with $L_{cell} = 3\sigma$, gray filled circles – full resolution GEMC [15].

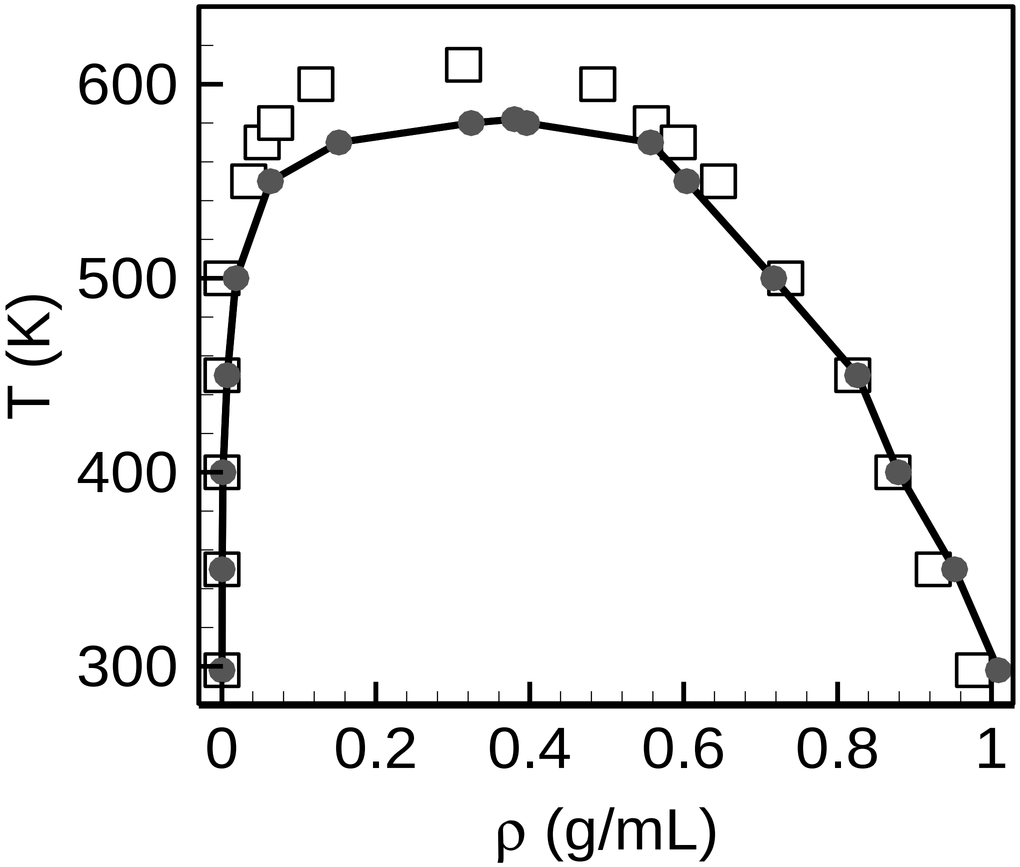

Figure 2.14: VLE phase envelopes for SPC-water. Open squares – CG-MMC with $L_{cell} = 3\sigma$, gray filled circles – full resolution GEMC [16].

Example equilibrium configurations using the LJ potential at all three coarse-graining scales ($L_{cell} = 3\sigma$, 4σ and 6σ)_are shown in Figure 2.15. While the overall liquid-vapor distributions are qualitatively similar, the reduced intra-phase fluctuations in the simulations with larger cells are clearly visible. This effect was quantified by considering the density distributions at a simpler, single-phase state point using all three coarse cell sizes. Shown in Figure 2.16 are the cell density histograms obtained from CG-MMC simulations (open symbols) at each of the three coarse graining levels for the state point

($\rho^* = 0.6$, $T^* = 1.1$), along with the corresponding histograms obtained from full resolution MMC simulations (filled symbols). As the cell size increases, the distributions become more sharply peaked around the overall density; for single-phase conditions such as the case considered in Figure 2.16, the distributions are Gaussian with standard deviations that scale as $(V_{cell})^{-1/2}$. At all three coarse-graining levels, the agreement with the corresponding full-resolution histograms is essentially perfect. Further discussion of the role of cell size and associated errors in CG-MMC simulations is presented in Chapter 3.

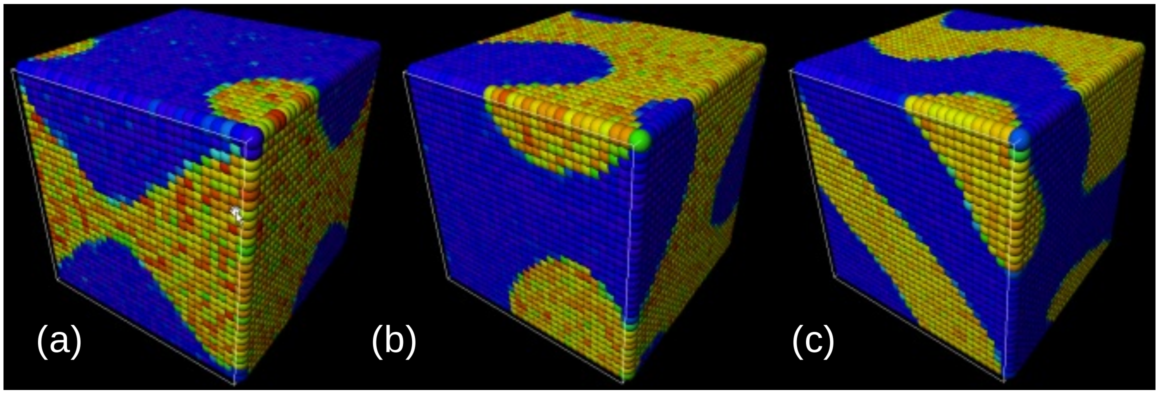

Figure 2.15: Equilibrium snapshots of LJ CG-MMC simulation configurations at $T^* = 0.8$ and $\rho^* = 0.3$. Coarse cell sizes are (a) $L_{cell} = 3\sigma$, (b) $L_{cell} = 4\sigma$, and (c) $L_{cell} = 6\sigma$. Cell color denotes reduced density that ranges from zero (dark blue) to 0.9 (red). There are 30 coarse cells in each direction; the effective number of particles in each CG-MMC simulation is approximately 2.2×10^5, 5.1×10^5, and 1.7×10^6, respectively.

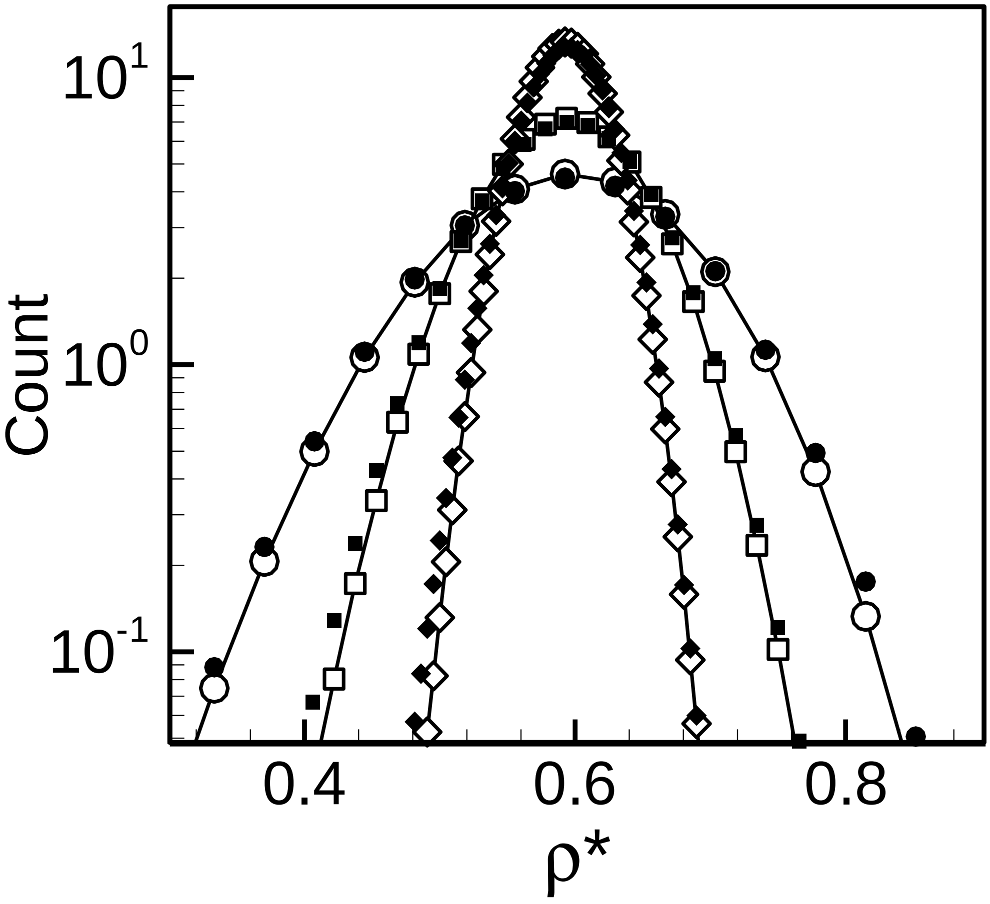

Figure 2.16: CG-MMC area-normalized cell density histogram for equilibrated LJ-argon at $\rho^* = 0.6$, $T^* = 1.1$ obtained using coarse-grained potential computed at $L_{cell} = 3\sigma$ and applied to CG-MMC simulations at 3σ (circles), 4σ (squares) and 6σ (diamonds). Open symbols are CG-MMC results, filled symbols are corresponding full resolution results.

2.7 Conclusions

In this Chapter, the basic CG-MMC simulation approach was derived and validated using three common interaction potentials. It was demonstrated that the method is able to capture the full VLE characteristics of both atomic (LJ and SW) and molecular (SPC-water) systems. The approach was also shown to be successful in describing the (equilibrium) microscopic density distributions within each phase using direct comparison to full-resolution Monte Carlo simulations.

The key advantages of the CG-MMC approach are explicitly evident. First, the each move within a simulation corresponds to a “larger” step within phase space that enables a faster approach to equilibrium. The ability to make larger moves, while still maintaining a high acceptance probability arises from the fact that the coarse-grained free-energy landscape is correspondingly smoother than the full-resolution one. For all the simulation examples presented in this Chapter, the move acceptance probability ranged from 70-80%. In other words, a single particle move between nearest-neighbor coarse cells always represents a small distance relative to the features of the landscape, irrespective of the coarse-graining level. In addition, the efficient representation of the numerically derived potential, along with the small number of neighboring cells that must be considered in its evaluation, makes each move computationally efficient.

Equally importantly, the numerical averaging procedure used to pre-evaluate the coarse-grained potential at a given temperature and coarse-graining level does not require any specific physical insight and appears to be applicable to any (short-ranged) potential. Although only pair potentials were considered here, there does not seem to be any apparent limitation for applying CG-MMC to many body interaction models. This is in contrast to many existing coarse-graining approaches that generally require some measure of physical insight to be established before the transformation can be applied.

Although the CG potential pre-computation can be expensive, it can be trivially farmed out to an arbitrary number of compute nodes, limiting the bottleneck associated with this calculation. In one sense, the CG-MMC transformation introduced in this Chapter can be regarded as one that transforms a Monte Carlo problem from one that is difficult to parallelize into one that is much easier (and more efficient). In the following Chapter, we describe two additional strategies for further reducing the computational overhead associated with coarse-grained potential pre-calculation and thereby show that the approach is well suited to challenging situations in which the temperature and the relevant length and time scales are evolving during a simulation. These examples are not intended to be comprehensive, but rather to motivate further work aimed at increasing the scope of the CG-MMC technique.

References

---

[1] M. A. Katsoulakis, A. J. Majda, and D. G. Vlachos, *Proc. Natl. Acad. Sci. USA* **100**, 782 (2003).

[2] M. A. Katsoulakis and D. G. Vlachos, *J. Chem. Phys.* **119**, 9412 (2003).

[3] A. Chatterjee, D. G. Vlachos, and M. A. Katsoulakis, *J. Chem. Phys.* **121**, 11420 (2004).

[4] A. E. Ismail, G. C. Rutledge, and G. Stephanopoulos, *J. Chem. Phys.* **118**, 4414 (2003).

[5] A. E. Ismail, G. Stephanopoulos, and G. C. Rutledge, *J. Chem. Phys.* **118**, 4424 (2003).

[6] J. G. Dai, W. D. Seider, and T. Sinno, *J. Chem. Phys.* **128**, 194705 (2008).

[7] B. Widom, *J. Chem. Phys.* **39**, 2808 (1963).

[8] V. I. Manousiouthakis and M. W. Deem, *J. Chem. Phys.* **110**, 2753 (1999).

[9] V. Vitek, *Computer Atomistic Modeling in Material Science*, Course Note. (2007).

[10] W. L. Jorgensen, J. Chandrasekhar, J. D. Madura, R. W. Impey, and M. L. Klein, *J. Chem. Phys.* **79**, 926 (1983).

[11] M. Mezei, *Mol. Simul.* **9**, 257 (1992).

[12] I. G. Tironi, R. Sperb, P. E. Smith, and W. F. Vangunsteren, *J. Chem. Phys.* **102**, 5451 (1995).

[13] D. Wolf, P. Keblinski, S. R. Phillpot, and J. Eggebrecht, *J. Chem. Phys.* **110**, 8254 (1999).

[14] http://www.ovito.org/

[15] D. Frenkel and B. Smit, *Understanding Molecular Simulation: From Algorithms to Applications*, 2nd ed. (Academic, San Diego, 2002).

[16] J. R. Elliott and L. G. Hu, *J. Chem. Phys.* **110**, 3043 (1999).

Chapter 3

Approximated Closure Rules and Further Investigation of Coarse-grained Lattice Monte Carlo Models

3.1 Introduction

The purpose of this chapter is two-fold. First, we seek to further describe the theoretical underpinnings of CG-MMC by more fully exploring potential sources of error. Second, we introduce additional closure approximations that substantially enhance the utility of the CG-MMC approach introduced in Chapter 2 by reducing the overall computational effort associated with pre-calculation of the coarse-grained interaction potential. While we unequivocally demonstrated that CG-MMC simulations are substantially more efficient than the corresponding full-resolution Metropolis Monte Carlo simulations, the pre-calculation of the coarse-grained interaction potential generally is computationally expensive and can be a bottleneck in the practical application of the CG-MMC method. This is expected to become increasingly the case as more complex systems, such as multicomponent mixtures and larger molecular entities, are considered.

In this Chapter we first demonstrate that it is possible to obtain coarse-grained interaction potentials at several temperatures simultaneously with a single sequence of calculations. This is an important advance because the vapor-liquid equilibrium phase envelopes computed in Chapter 2 for the three different potential models (LJ-Argon, square-well, and SPC-water) required that a coarse-grained interaction potential be obtained at each temperature of interest, greatly increasing the overhead associated with coarse-grained potential evaluation. As discussed previously, this requirement stems from the fact that coarse-grained potentials include entropic contributions from the missing degrees-of-freedom, and therefore are temperature dependent.

In the latter part of this Chapter, we also establish that the coarse-grained potentials used in CG-MMC are scalable, so that a potential computed at one coarse-graining scale can be employed at a variety of other coarse-graining levels. This finding provides an attractive solution for addressing multiresolution phenomena in which different coarse-graining scales are needed in a single simulation. Finally, we address in more detail the computational advantages of CG-MMC relative to standard full resolution Monte Carlo simulations.

3.2 The Supercritical Fluid Closure Approximation

We consider again the "base case" closure approximation that was used to perform the simulations in Chapter 2, in which the free energy change associated with the addition of one particle into a particular cell was simplified from

$$\Delta A = \Delta A_{id}\left(\rho, T\right) + \Delta A_{ex}\left(\rho(r), \rho_{env}(r), T\right), \tag{3.1}$$

to

$$\Delta A = \Delta A_{id}\left(\rho, T\right) + \Delta A_{ex}\left(\rho, \rho_{env}, T\right). \tag{3.2}$$

The assumptions implicit in transforming eq. (3.1) to eq. (3.2) include that (1) the "environment" is localized around the coarse cell in question, (2) the density distribution within the environment is coupled only to that in the central coarse cell, (3) the density distributions within the coarse cell and the environment are fully characterized by their respective overall average densities.

Equation (3.2) indicates that there exist three coarse state variables for defining the coarse-grained interaction potential, which are ρ, ρ_{env}, and T, necessitating a three-dimensional parameterization to fully evaluate the coarse-grained potential function**.** Here, we consider a simple but useful additional closure approximation that enables the calculation of a coarse-grained potential at all temperatures of interest with a single set of simulations, which effectively reduces potential evaluation to a two-dimensional scan over the densities.

In essence, the approximation entails the assumption that the fluids in both the reference coarse cell and its environment are homogeneously-distributed single phases at all densities. In other words, micro-configurations that correspond to phase separation at the sub-cell scale are neglected, while the basic structure of the fluid phase is retained. In order to enforce such a closure approximation, we assume that the fluid particles sample trajectories that correspond to a weakly supercritical state, *irrespective of the temperature at which the excess chemical potential is being computed*. In this view, we refer to this closure approximation as the supercritical fluid approximation, or SCFA.

It is instructive to consider the SCFA within the context of commonly employed closure approximations of this type. Shown in Figure 3.1 are different scenarios for particle trajectory sampling. In the leftmost panel, the actual particle trajectories at a given temperature are used – this represents the "no-approximation" situation that was used to compute the results in Chapter 2. At the other end of the spectrum, the two rightmost panels suggest very simplistic approximations. In the first (Local Mean Field, or LMF), it is assumed that particles are uniformly "smeared" across the domain and that the system exists at steady state. While this approach has been used successfully for certain interacting systems (e.g., Ising-type models [3, 4]), it is clearly not appropriate for describing discrete particles that evolve in continuous space – the LMF closure approximation is only applicable when the full resolution problem is itself defined on a lattice. The Random Positions (or Ideal Gas) model in the rightmost panel can be considered to be the closest analogue of the LMF for particles in continuous space. However, this approximation neglects any fluid structure that might be predicted by the interaction potential and also leads to sampling of potentially very high energy configurations that would be hihgly unlikely in the actual system. Finally, the Homogeneous (or Supercritical) Fluid model represents a compromise between the exact particle trajectories and the LMF or RP/IG. Here, the fluid structure that is predicted by a particular interaction potential is retained but phase separation is neglected. In one sense, this approximation retains small length scale features, while neglecting larger features.

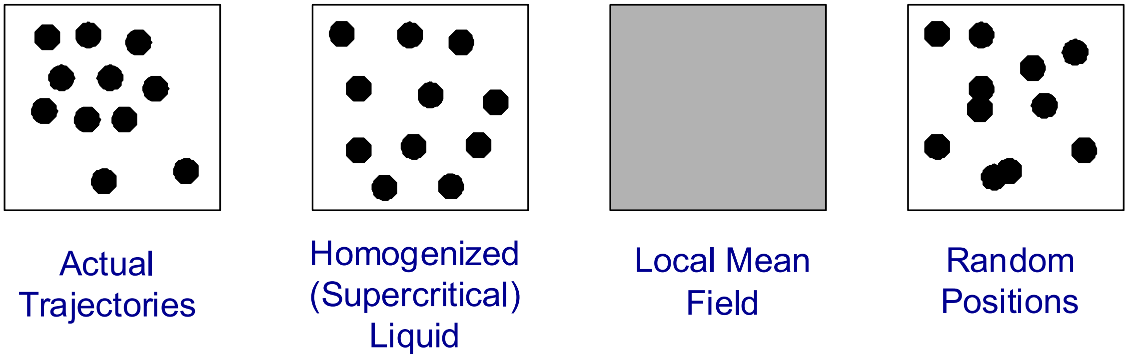

Figure 3.1: Schematic representations of different scenarios for particle trajectory sampling. From left to right are actual trajectories; homogenized (supercritical) liquid; local mean field; and random positions.

The modification of the Widom method used to compute the particle insertion free energy required in order to implement the SCFA is in principle straightforward: evolve the particle positions using Metropolis Monte Carlo moves based on a (reduced) homogenization temperature above the critical value, T_H^*, while accumulating the average(s) in eq. (2.11) using the temperature(s) of interest. Because the latter temperature(s) is(are) decoupled from the homogenization temperature, multiple averages can be accumulated simultaneously thereby enabling the calculation of excess chemical potentials at multiple temperatures within a single Widom simulation. In the following analysis, we seek to evaluate the impact of T_H^* within the SCFA, and to determine whether bounds exist on the allowable extent of homogenization, that is, the maximum temperature for evolving the supercritical fluid.

The VLE envelope for the LJ-argon case is used to evaluate the effects of applying the SCFA. In Figure 3.2 we show VLE envelopes for LJ-argon predicted using the base-case closure rule (i.e., using the actual particle trajectories at each temperature) and several different homogenization temperatures, all corresponding to supercritical fluids. First, as expected, the VLE is largely unaffected by the SCFA in the vicinity of the critical point, even when the homogenization temperature is as high as $T_H^* = 3.0$. On the other hand, at lower temperatures, the error in equilibrium liquid density increases with homogenization temperature. When $T_H^* = 1.2$, the error at the lowest VLE temperature considered ($T^* = 0.6$) is less than 5% but quickly saturates to the maximum density allowed in the simulation ($\rho^* = 0.85$) at $T^* = 1.5$. At $T_H^* = 3.0$, large errors are apparent at higher VLE temperatures. The vertical dashed lines in Figure 3.2 represent the VLE results obtained when infinite homogenization temperature is applied, which corresponds to the Random Positions or Ideal Gas approximation in Figure 3.1. In this case, all CG-MMC simulations temperatures lead to complete phase separation into a zero density vapor phase a maximum density liquid phase. Recall that the maximum density is defined by the density range over which the coarse-grained potential was evaluated, and moves that lead to cell densities higher than this limit are automatically rejected.

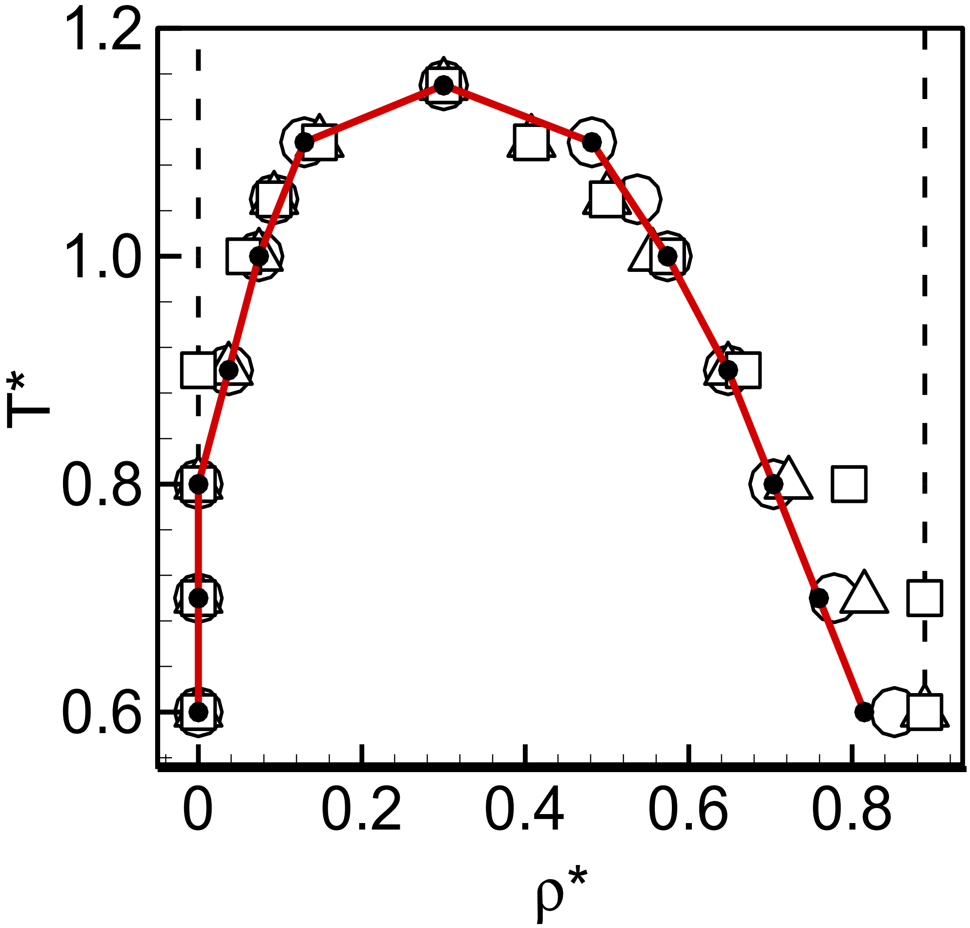

Figure 3.2: VLE phase envelopes for LJ-argon as a function of homogenization temperature within the SCFA closure approximation. Small filled circles and solid line – base

case (no SCFA), open circles – $T_H^* = 1.2$, open triangles – $T_H^* = 1.5$, open squares – $T_H^* = 3.0$, dashed line – ideal gas ($T_H^* \rightarrow \infty$).

The results in Figure 3.2 suggest that the SCFA is a good approximation as long as the homogenization temperature is not too high. Moreover, the quality of the SCFA closure approximation is non-uniform as it becomes worse at lower temperatures. In order to better define the upper bound on T_H^*, radial distribution functions were computed for several LJ systems at $\rho^* = 0.3$ and different temperatures, see Figure 3.3. There is no obvious transition in the radial distributions that denotes a limiting homogenization temperature beyond which the SCFA suddenly breaks down. Rather, there is a gradual degradation as the radial distribution profiles diverge from the reference temperature considered here ($T^* = 0.6$). The precise source of the error associated with the SCFA is therefore difficult to pinpoint from the radial distribution functions, but it is most likely related to the deviations at the first density peak.

With the preceding observations in mind, the prescription for applying the SCFA is that the homogenization temperature be set to a value at or near the critical temperature. Finally, we note that the rather narrow homogenization temperature constraint that is apparent for the LJ case is not a general result. For systems of particles in which the interactions include a hard-core (e.g., colloidal particles), the radial distribution functions around the first density peak are expected to be much less sensitive to temperature and as a result, would accommodate a wider range of homogenization temperatures with acceptable errors. Future studies with a broader range of interaction functions should help better define the applicability limits of the SCFA and establish more concrete prescriptions for its use.

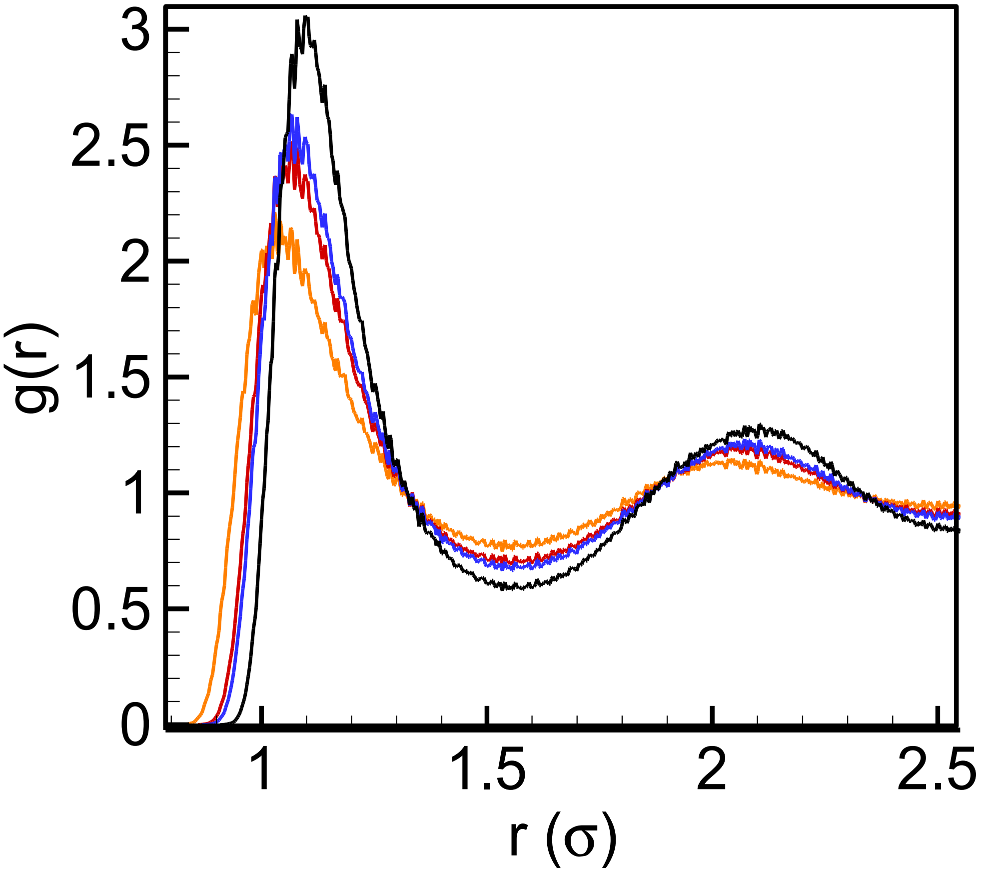

Figure 3.3: Radial distribution function for LJ-argon at $\rho^* = 0.6$ and several different temperatures. From highest peak down: Black – $T^* = 0.6$ (reference), Blue – $T^* = 1.2$, Red – $T^* = 1.5$, Orange – $T^* = 3.0$. All state points aside from the reference correspond to single-phase fluids.

3.3 Coarse-Grained Potential Scaling and Error Analysis

The implicitly contained entropic factors that make coarse-grained potentials functions of temperature may also introduce dependence on the coarse-graining scale. As a result, a different coarse-grained potential function may be required for CG-MMC simulations with different coarse cell sizes. At the same time, many non-equilibrium phenomena of interest take place over a large range of length and timescales. An example is the coarsening that occurs following spinodal decomposition in a fluid system – at early times, rapidly changing density gradients are present over atomic length scales, but as the system evolves, gradients become defined by much larger scales [5]. Another important potential bottleneck in CG-MMC simulations, therefore, is the need to compute multiple CG potentials at several different coarse-graining scales for use in a multiresolution simulation. In addition to the overall number of chemical potential evaluations required for a multiresolution simulation, one must also consider the fact that as the coarse-graining level increases, each individual chemical potential calculation itself becomes increasingly expensive due to the increasing number of particles within a coarse cell at a given density. The combination of these two factors makes multiresolution simulation with CG-MMC rather limited in scope.

In this section, we investigate the possibility of scaling an excess chemical potential surface obtained at one coarse graining level to another. Such scaling can be considered to be another example of closure approximation, in which finite cell size effects are ignored. A broader treatment of multiresolution simulations in which very large cell sizes are considered is deferred to Chapter 5. In fact, coarse-grained potential "scaling" is realized trivially by considering that the chemical potential surfaces shown in Figures 2.5 for LJ-argon, 2.6 for SW and 2.7 for SPC-water in previous chapter are expressed as a function of cell densities and therefore only implicitly refer to the number of particles. In other words, assuming that finite size effects are non-existent, at different cell sizes a given density simply corresponds to different numbers of particles. Thus, at least in principle, the chemical potential surfaces shown in Figures 2.5, 2.6 and 2.7, which were evaluated for cells of size 3σ, could be used directly in CG-MMC simulations at any larger scale (we refer to this as "upscaling"). Similarly, chemical potential surfaces computed at larger cell sizes could be used in a CG-MMC simulation at the 3σ resolution (or "downscaling"); both of these possibilities are demonstrated in Figures 3.4 and 3.5 for the LJ-argon case.

In Figure 3.4, LJ-argon VLE diagrams obtained from CG-MMC simulations with coarse cells of size 3σ (squares), 4σ (diamonds), and 6σ (circles) are shown, each of which was based on the excess chemical potential surface computed with 3σ cells. The predicted VLE curves are essentially invariant with respect to the coarse cell size used in the CG-MMC potential. Thus, when the 3σ potential is upscaled to a larger cell size in a CG-MMC simulation, the VLE curve is unchanged and reflects any finite cell size errors (and any other uncertainties such as statistical uncertainty in the free energy calculations) at the original coarse-graining level. These results suggest that finite cell size errors at the original coarse-graining level continue to have similar impact at larger scales.

We can better understand this behavior by conceptually defining two types of finite size errors: (1) those that are incurred during the calculation of the coarse-grained potential, and (2) those that are incurred within the CG-MMC simulation itself. We will refer to these hypothetical finite size errors as Type 1 and Type 2 errors, respectively. Type 1 errors could arise because certain configurations (e.g. those associated with large-scale fluctuations) are omitted during free energy sampling, or because cell size dependent boundary layers in the particle density distribution near the interface between the cell and the environment distort the averaging procedure. Type 2 errors, on the other hand, could arise from the discretized nature of the allowable densities during CG-MMC simulation. For example, at the 3σ coarse-graining level a total of only 25 different density values are possible (corresponding to single particle steps), which could lead to artifacts particularly when small density differences become important, e.g., near the critical point. By comparison, there are about 200 allowable density levels at the 6σ coarse-graining scale, enabling a much finer density resolution than at the 3σ scale.

Within this idealized framework, the results in Figure 3.4 suggest that Type 1 errors are dominant when the 3σ coarse-grained potential is upscaled. In other words, the lack of improvement upon upscaling indicates that Type 2 errors, which are expected to decrease with upscaling, are small compared to the Type 1 errors that are fixed by the coarse-grained potential pre-calculation.

In Figure 3.5, VLE diagrams are shown for CG-MMC simulations with cells of size 3σ and 6σ, using the potential computed at 6σ. Interestingly, downscaling of the 6σ potential to 3σ cells does not enable a more accurate simulation at the 3σ scale (circles), i.e., the increased accuracy obtained with the larger cells is not retained when downscaling is applied. Instead, the downscaled VLE curve is similar in quality to the one obtained using the unscaled 3σ potential (which is shown again in Figure 3.5 by the square symbols). Within the qualitative error framework defined above, these findings suggest that at the 6σ coarse-graining level, Type 1 and Type 2 errors are both small (resulting in a globally good VLE envelope as shown previously in Figure 2.12), but Type 2 errors become significant upon downscaling the potential to smaller cells.

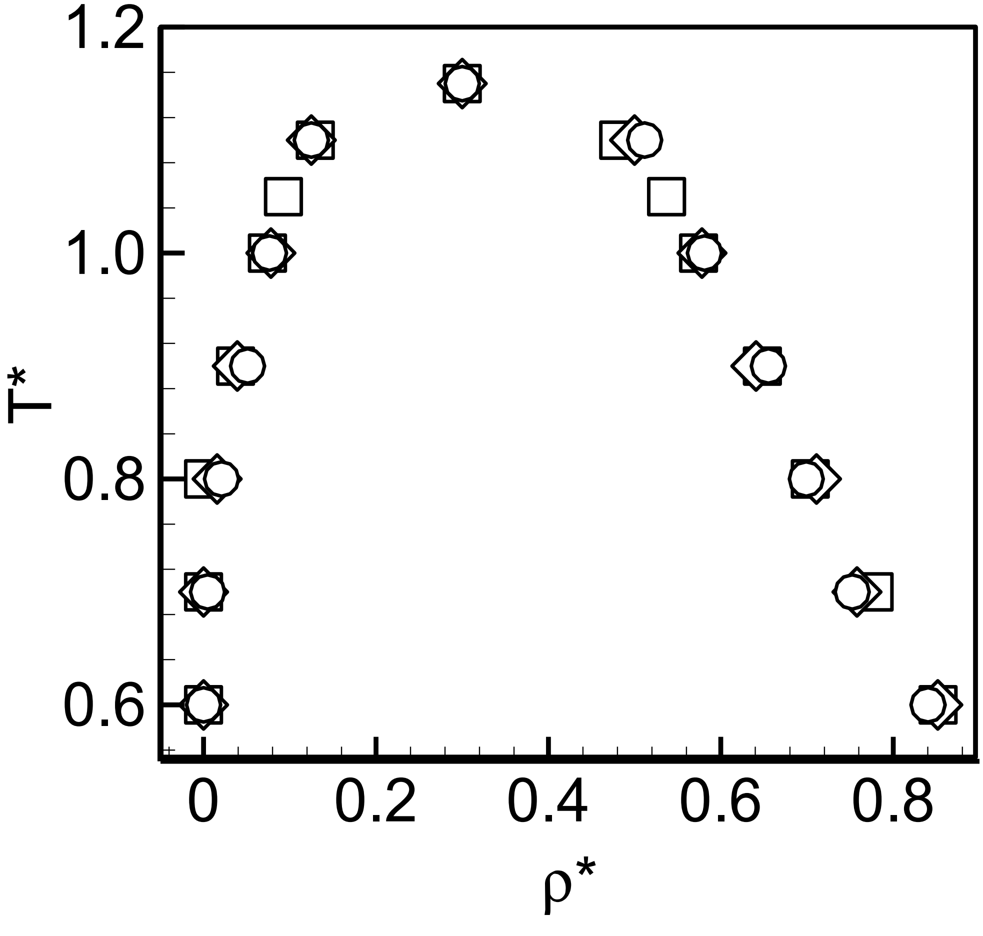

Figure 3.4: VLE phase envelopes for LJ-argon based on coarse-grained potential computed at $L_{cell} = 3\sigma$ and applied to CG-MMC at 3σ (squares), 4σ (diamonds) and 6σ (circles).

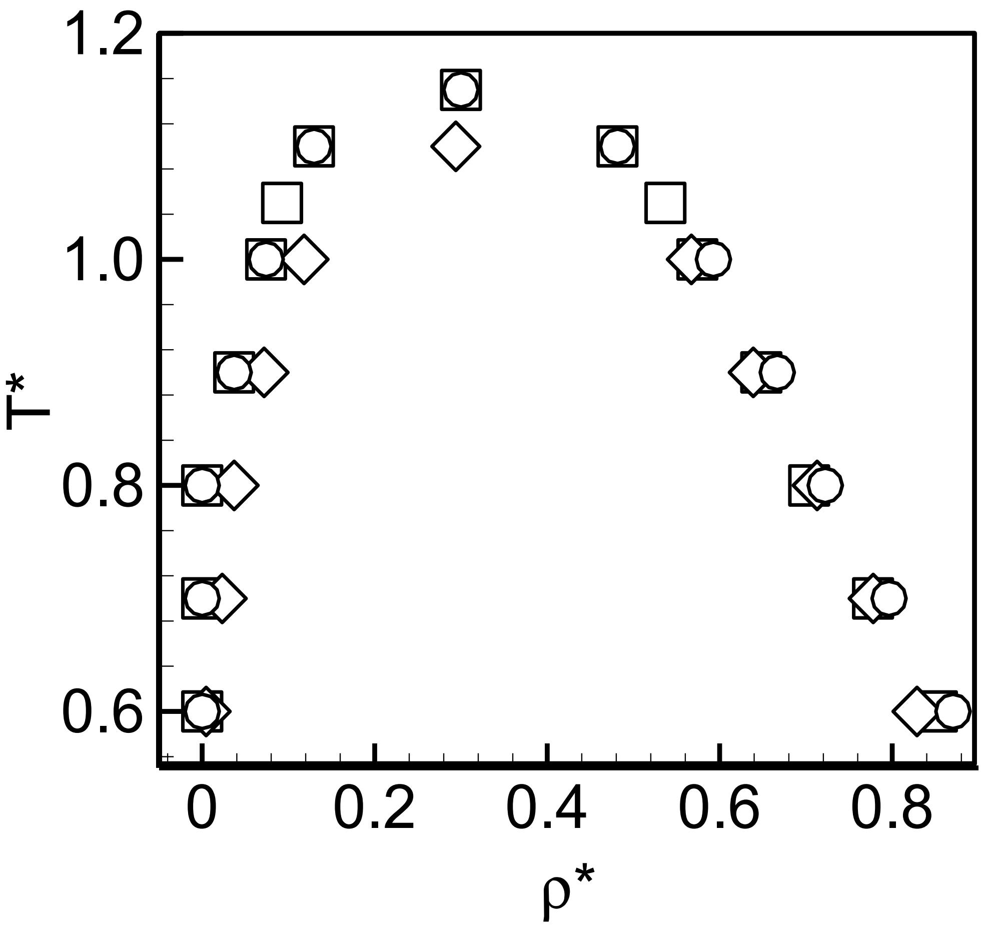

Figure 3.5: VLE phase envelopes for LJ-argon based on coarse-grained potential computed at $L_{cell} = 6\sigma$ and applied to CG-MMC at 6σ (diamonds) and 3σ (circles); also shown for reference is $L_{cell} = 3\sigma$ applied to CG-MMC at 3σ (squares).

Next, we attempt to better define the specific sources of error, particularly those of Type 1. The most obvious of these is the statistical uncertainty associated with computing the chemical potential at a given density combination. As shown in Figure 2.5, there is visible scatter in the individual data points particularly at the higher densities, where convergence of the Widom insertion method is slow. While the actual input to a CG-MMC simulation is an interpolated surface through the aggregate of the data points, the scatter in the individual points does lead to errors in the interpolated surface. The choice of interpolating function itself also is a source of error; if the order is too high, the resulting surface will reflect noise in the data, while too few degrees-of-freedom will result in a surface that cannot adequately capture the curvature across the range of the data. The examples shown in Figure 2.5 reflect a compromise between these two factors (3^{rd} order polynomial fit in each of two dimensions). It is noteworthy that the chemical potential data obtained for the $L_{cell} = 6\sigma$ case exhibited significantly less scatter than both the $L_{cell} = 3\sigma$ and $L_{cell} = 4\sigma$ cases across the entire density range considered – this may be one factor in the improved VLE diagram obtained at $L_{cell} = 6\sigma$, although there is no fundamental reason that the statistical scatter should be correlated with the cell size in general. A better method for chemical potential estimation that allows for better convergence would be required to unambiguously assess the role of this source of Type 1 error in the resulting VLE phase diagrams.

The second potential source of Type 1 error is a cell finite size effect that limits the accessible configurations and/or fluctuation length scale during the Widom sampling; if present, this error would be expected to diminish as the cell size was increased, consistent with the improved results at $L_{cell} = 6\sigma$. To probe the presence of finite cell size effects, averaged intra-cell density profiles at $T^* = 1.1$ were generated (using the simulation cell setup in Figure 2.4(a) in Chapter 2) for several combinations of inner cell and environment densities using three different cell sizes; see Figures 3.6 and 3.7. In Figure 3.6, the densities in the inner cell and environment are equal, resulting in a spatially invariant distribution across the inner cell; no significant cell size effect is expected for these cases. This is further confirmed by the results in Figure 2.16 in Chapter 2 that show that the coarse-grained potential computed at 3σ is fully able to capture the microscopic details in a single-phase system, where cell-to-cell density variations tend to be small. Moreover, the scalability of the potential across coarse-graining scales is expected to be excellent under these conditions because the profiles would not be distorted by the scaling operation.

In Figure 3.7, however, it is seen that large density differences across the boundary between the inner cell and the environment leads to the formation of an inner region and a boundary layer within the inner cell. When the inner cell density is high compared to the environment density (upper curves), the inner region density is equal to the overall cell density and the boundary layer exhibits oscillations about this value with a period corresponding to about one σ. The boundary layer structure itself appears to be unaffected by the cell size, although at $L_{cell} = 3\sigma$, the boundary layer effectively extends across the entire cell. In the opposite situation (low inner cell density relative to environment – lower curves) the inner region is strongly depleted relative to the overall set-point density, with most of the particles present near the cell boundary. Again, the boundary layer profile itself is apparently unaffected by the cell size.

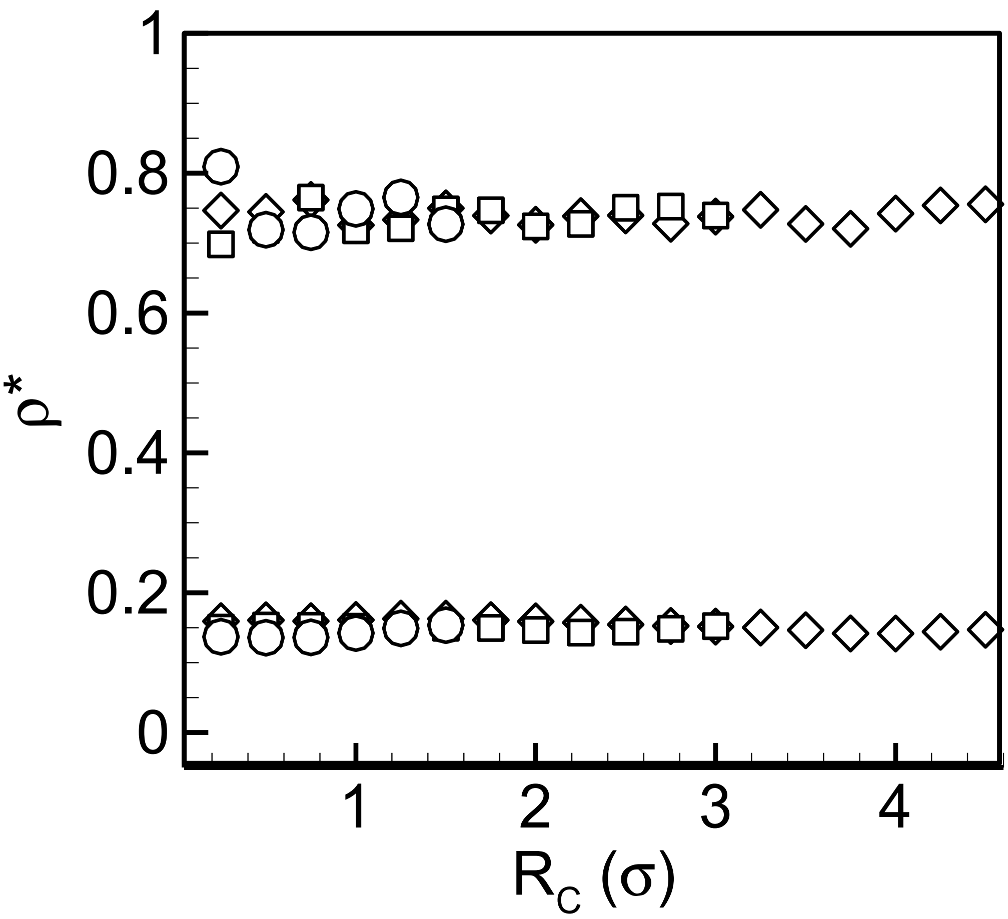

Figure 3.6: Intra-cell reduced density spatial distribution as a function of distance from the cell center for LJ-argon with equal density in inner cell and environment; lower curves – $\rho^*_{cell} = \rho^*_{env} = 0.15$, upper curves – $\rho^*_{cell} = \rho^*_{env} = 0.75$. Circles – $L_{cell} = 3\sigma$, squares – $L_{cell} = 6\sigma$, diamonds – $L_{cell} = 9\sigma$.

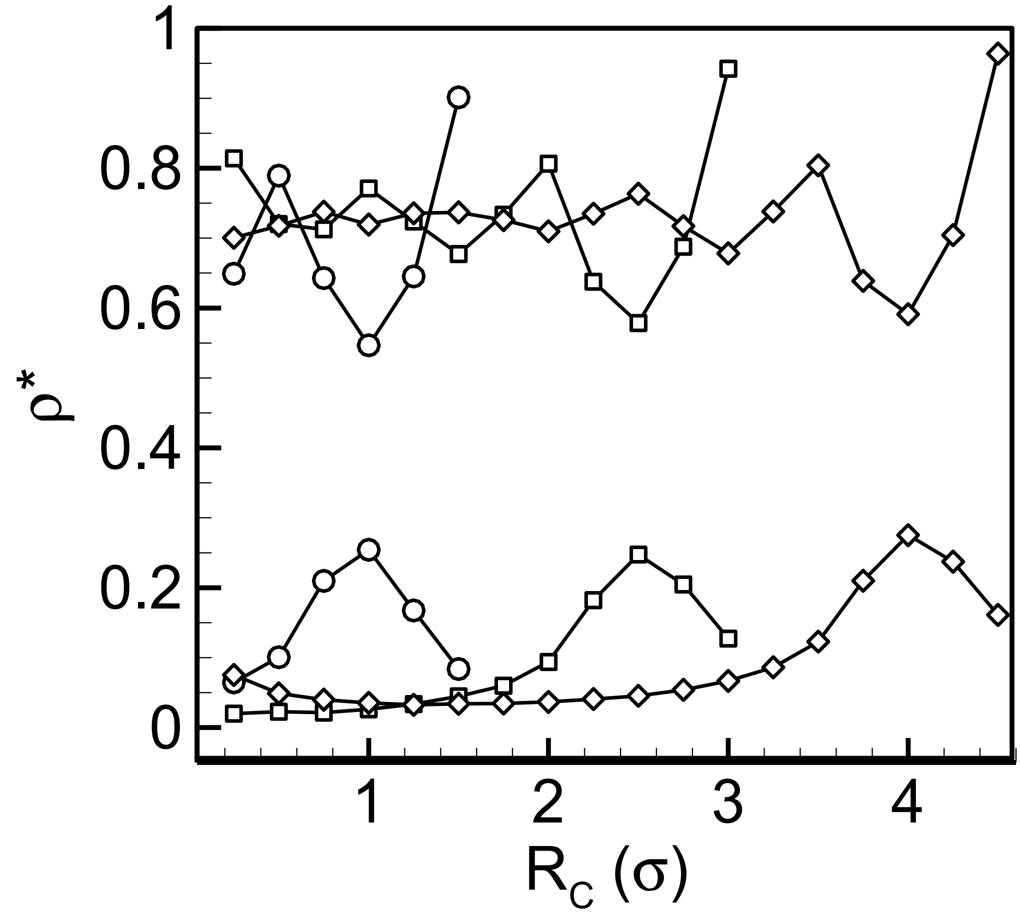

Figure 3.7: Intra-cell reduced density spatial distribution as a function of distance from the cell center for LJ-argon with different density in center cell and environment; lower curves – $\rho^*_{cell} = 0.15, \rho^*_{env} = 0.75$, upper curves – $\rho^*_{cell} = 0.75, \rho^*_{env} = 0.15$. Circles – $L_{cell} = 3\sigma$, squares – $L_{cell} = 6\sigma$, diamonds – $L_{cell} = 9\sigma$.

The results in Figures 3.6 and 3.7 suggest that cells with dimension $L_{cell} = 3\sigma$ (and 4σ) may indeed be too small to fully accommodate intra-cell density variations under certain conditions (e.g. a two-phase system) and thus lead to finite size errors. In fact, a comparison of the excess chemical potential for the LJ-argon system at $T^* = 0.8$ for

$L_{cell} = 3\sigma$ and 6σ shows maximum systematic deviations at the edges, where the inner cell and environment densities are most different; see Figure 3.8. Conversely, along the diagonal where the two densities are similar, the chemical potential values are almost identical and the two surfaces intersect. The preceding observations notwithstanding, the observed finite cell size error due to the density boundary layer does not necessarily explain the fact that the discrepancies in the VLE envelopes at $L_{cell} = 3\sigma$ and 4σ are apparent mainly near the critical point, where cell-to-cell density variations are generally small and the situation in Figure 3.6 is expected to be more representative of the overall simulation conditions. Instead, it would be expected that finite size errors would be most noticeable when large cell-to-cell density variations exist, a condition which prevails under two-phase equilibrium at lower temperatures away from the critical point. Further investigations, using other potentials and better statistical quality for the chemical potential surfaces, should help clarify remaining uncertainties associated with potential sources of error.

The density boundary layers observed in Figure 3.7 do, however, cast some doubt on the scalability of the potentials across coarse-graining scales under conditions where strong density differences exist from cell to cell. Clearly, compressing or stretching the profiles in Figure 3.7 at one scale does not produce the same profile at another scale and would distort the boundary layer region. Empirically, the results in Figures 3.4 and 3.5 suggest that this distortion does not strongly influence the VLE prediction and based on this observation here we make the claim that the potentials are scalable by simple stretching and compression. Further work will be needed to fully quantify the impact of the intra-cell non-uniformity on the scalability of the coarse-grained potentials.

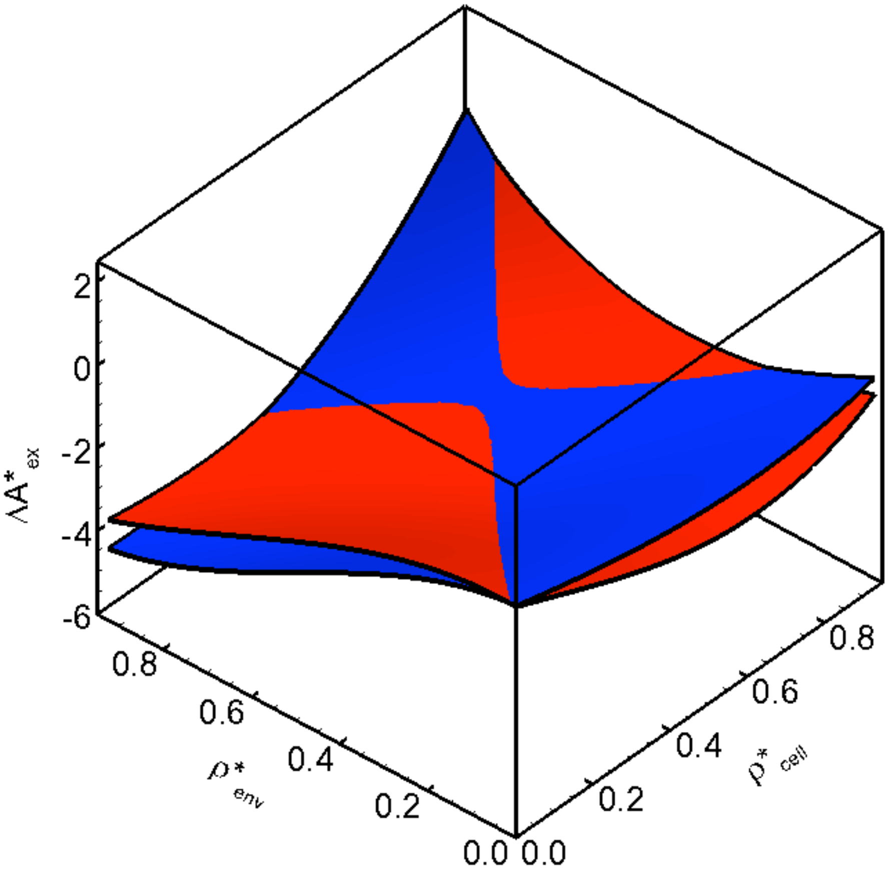

Figure 3.8: Polynomial interpolations of excess chemical potential fields computed for LJ potential for argon at $T^* = 0.8$ as a function of cell and environment densities. Coarse cell size is 3σ (blue surface) and 6σ (red surface).

In the context of error analysis we also consider here the impact of the center-of-mass constraint (see Figure 2.4(b) in Chapter 2) on the intra-cell density distribution of water molecules. Recall that point constraints on the molecule positions are required to avoid the formation of artificial boundary layers at the cell-environment interface, which necessarily implies that some part of the molecular entity will be allowed to cross the interface. Shown in Figure 3.9 are the hydrogen and oxygen number density profiles for two situations. The dashed lines show the oxygen (squares) and hydrogen (circles) number densities for the case when both the cell and environment are maintained at equal (low) density. Both oxygen and hydrogen profiles are flat at the overall density value (with the number of hydrogen atoms being double that of the molecule number). The solid lines represent the case when the inner cell density is increased to a high value while maintaining the environment at the low density.

As seen in the LJ case, the oxygen profile develops a boundary layer with a slight increase near the inner cell surface as the oxygen atoms find free volume near the inner cell boundaries. The hydrogen density, however, exhibits the opposite behavior because hydrogen atoms are able to cross the boundary and are therefore not counted within the inner cell. The net number of hydrogen atoms that lie across the boundary in this case is only about 12% of the total; the resulting implications with respect to the applied density constraint are quite modest, particularly given the small molecular weight of the hydrogen, and can be neglected in CG-MMC simulations of water. Of course, this issue may be more significant for larger or homoatomic molecules in which a significant fraction of the molecular mass is allowed to cross the boundary; these considerations are deferred to future work in applying the CG-MMC method to larger molecular entities.

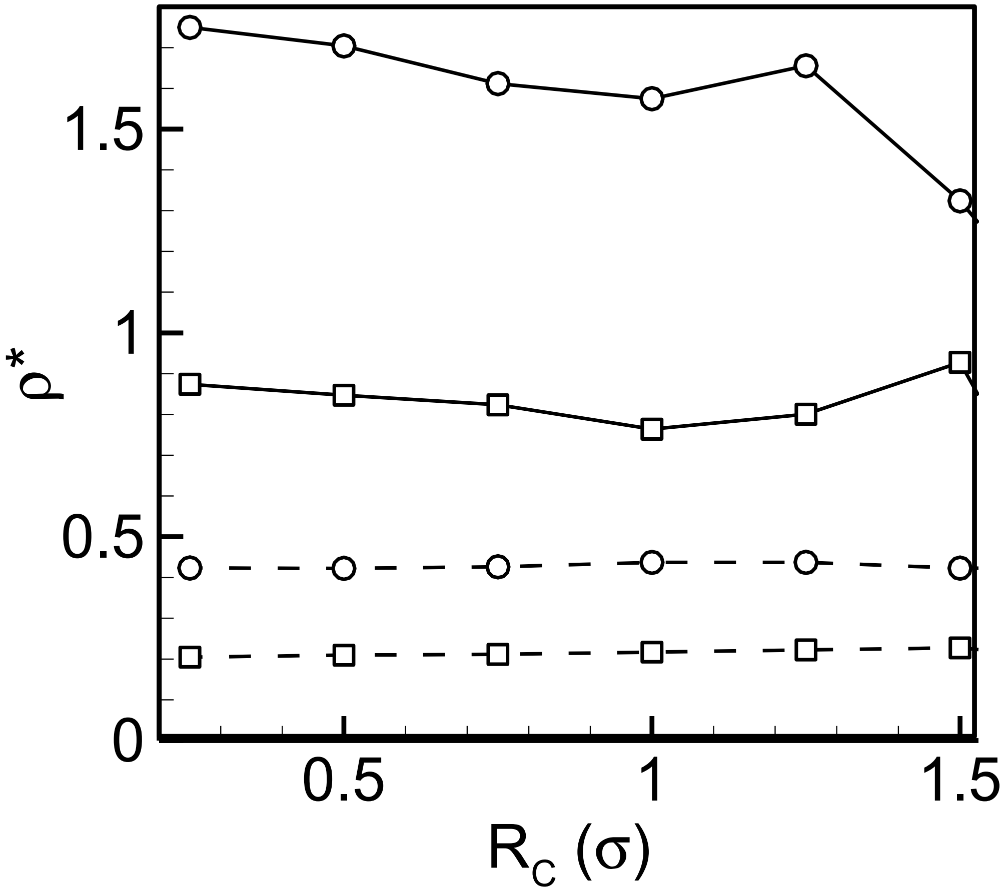

Figure 3.9: Intra-cell reduced (molecular) number density spatial distribution as a function of distance from the cell center for SPC-water ($L_{cell} = 3\sigma$); squares – oxygen, circles – hydrogen. Solid lines – $\rho_{cell} = 0.8$ g/ml, $\rho_{env} = 0.2$ g/ml, dashed lines – $\rho_{cell} = \rho_{env} = 0.2$ g/ml.

3.4 Computational Performance Analysis

We conclude this Chapter by outlining the several factors that make CG-MMC highly computationally attractive relative to full resolution MMC. In the following discussion performance comparisons are made on the basis of the same single compute core.

Bulk liquid LJ-argon is employed throughout as the basis for comparison between CG-MMC and full resolution MMC. In CG-MMC, the CPU time required for single particle move attempt is approximately 1×10^{-11} s, while it is about 1×10^{-9} s for our implementation of standard MMC. The difference arises mainly from the fact that the CG-MMC potential is tabulated/interpolated (although the analytical form of the LJ potential also is simple) and also because of the small cost associated with evaluation of the density in the neighboring cells, which does not require that any inter-particle distances be evaluated. Note that the standard MMC cost per move is a function of fluid density and potential cutoff via the average number of neighbors that each particle interacts with. Moreover, the complexity of the potential function (e.g., many-body potentials such as the SW potential for covalently-bonded silicon [6]) will play a significant role in the comparison.

Another significant computational advantage of CG-MMC over standard MMC is the move distance. First, it is important to distinguish between two classes of Monte Carlo simulation before a meaningful discussion of move size can be established. For cases in which only equilibrium properties are required, there is no restriction on move type. Indeed, many strategies for increasing efficiency of MMC simulation are based on making biased, large-displacement, and multi-particle moves that cover a lot of “distance” in phase space, and then removing any bias. On the other hand, it is well established that Metropolis Monte Carlo trajectories are equivalent, at least in a coarse-grained sense, to inertia-less Langevin trajectories when the moves are restricted to small displacements [7-9]. The criterion for defining “small” is related to, among other variables, the spatial gradient of the interaction potential; for potentials such as LJ, the typical maximum move distance is less than 0.2Å, which makes it 0.1Å on average. By contrast, the minimum move distance in CG-MMC is L_{cell}, which is about 10Å for cells of size 3σ (LJ potential). Note that the coarse-grained potential in CG-MMC is automatically scaled to a prescribed coarse-graining level. In other words, gradients in the potential naturally become smaller as the coarse-graining level increases. As such, a move over a single cell automatically satisfies the small move criterion in a CG-MMC simulation.

The effect of the move size difference between CG-MMC and full resolution simulations can be interpreted via a particle diffusivity, $D_P = R_d^2 / \tau$, where R_d is the maximum move distance and τ represents "time" via the number of Monte Carlo moves. In other words, the overall diffusivity in a CG-MMC simulation is expected to be $\sim \left(L_{cell} / 0.1\right)^2$ or 10^4 times higher for $L_{cell} = 3\sigma$. Thus, a CG-MMC simulation of spinodal decomposition and coarsening runs approximately 10^6 times faster than an equivalent full-resolution simulation (for $L_{cell} = 3\sigma$).

Finally, we discuss briefly the issue of coarse-grained potential precomputation, which of course represents a significant overhead cost for CG-MMC simulations. It is difficult to meaningfully quantify these costs because they depend on various factors, including the method used to compute excess chemical potentials, the necessary number of sampling points in density-space, and the coarse-graining scale to name a few. Most important, however, is the fact that the coarse-grained potential pre-computation is trivially distributable over an arbitrary number of compute nodes. In this sense, CG-MMC can be considered as a method to transform a Monte Carlo problem into one that is much easier to parallelize – much of the work is shifted from the MC simulation itself, which is difficult to parallelize efficiently, to potential pre-calculation, which can be easily distributed.

3.5 Conclusions

In this Chapter, the basic CG-MMC method was extended by the introduction of two closure approximations beyond the base case description in Chapter 2. First, a homogenization approximation in which a weakly supercritical fluid is substituted for the actual system was shown to enable the estimation of coarse-grained potentials at multiple temperatures with a single series of free energy calculations. When compared to reference calculations of the VLE envelope, the homogenization approximation was shown to exhibit excellent consistency across a range of temperatures. The nature of the supercritical fluid approximation, or SCFA, is such that it can be applied flexibly, thereby providing a measure of error control. Specifically, it is possible to employ more than one homogenization temperatures in the free energy calculations such that the homogenization temperature is never too far away from the temperature at which the coarse-grained potential is being evaluated. In fact, one could even imagine removing the restriction that that the "homogenization" temperature be above the critical point and instead employ sub-critical temperatures to evolve the particle trajectories. The trade-off between computational expense and error in such a hybrid approach will require further study.

It was also shown that the calculated coarse-grained potentials, when parameterized in terms of density (as opposed to the absolute number of particles), are highly scalable across different coarse-graining scales. Thus, a coarse-grained potential computed at one coarse-graining scale can be used at multiple other scales, making feasible the possibility of multiresolution or adaptive simulations. While finite cell size effects are apparent in the non-uniform density distributions across a cell during pre-calculation of the coarse-grained potential, these do not appear to limit the scalability of the coarse-grained potentials. In addition to the successful demonstration of potential scalability, upscaling and downscaling examples were shown to provide useful information regarding the various possible sources of error. Although additional studies will be required to fully assess the various error sources, there is evidence that finite size errors are present due to both potential evaluation and the CG-MMC simulation itself.

The ability to scale potentials should greatly enhance the application scope of the CG-MMC technique to situations in which spatially and/or temporally adaptive simulations are useful. In Chapter 5 of this thesis we consider a situation in which a coarse-grained potential is scaled to enable an adaptive simulation which becomes coarser as the features become larger. There it is shown that the primary challenge of extending CG-MMC to very large coarse-graining levels is to extend the single particle moves into multi-particle moves so that each move corresponds to a non-negligible transition in phase space.

References

---

[1] D. Frenkel and B. Smit, *Understanding Molecular Simulation: From Algorithms to Applications*, 2nd ed. (Academic, San Diego, 2002).

[2] W. L. Jorgensen, J. Chandrasekhar, J. D. Madura, R. W. Impey, and M. L. Klein, *J. Chem. Phys.* **79**, 926 (1983).

[3] M. A. Katsoulakis, A. J. Majda, and D. G. Vlachos*, Proc. Natl. Acad. Sci. USA* **100**, 782 (2003).

[4] J. G. Dai, W. D. Seider, and T. Sinno, *J. Chem. Phys.* **128**, 194705 (2008).

[5] N. Gonzalez-Segredo, M. Nekovee, and P. V. Coveney, *Phys. Rev. E* **67**, 046304 (2003).

[6] F. H. Stillinger and T. A. Weber, *Phys. Rev. B* **31**, 5262 (1985).

[7] K. Kikuchi, M. Yoshida, T. Maekawa, and H. Watanabe, *Chem. Phys. Lett.* **185**, 335 (1991).

[8] G. Tiana, L. Sutto, and R. A. Broglia, *Physica A - Statistical Mechanics and Its Applications* **380**, 241 (2007).

[9] R. T. Scarlett, J. C. Crocker, and T. Sinno, *J. Chem. Phys.* **132**, 234705 (2010).

Chapter 4

Non-Equilibrium Coarse-Grained Lattice Monte Carlo Simulations

4.1 Introduction

In Chapters 2 and 3, a spatial coarse-graining method for Metropolis Monte Carlo (MMC) simulations was presented in which an arbitrary inter-particle potential is numerically coarse-grained to enable coarse-grained MMC (CG-MMC) simulations of fluid systems on a rigid lattice. The CG-MMC approach was demonstrated to provide an excellent representation of various equilibrium properties such as vapor-liquid phase diagrams and intra-phase spatial density distributions for three different interaction potentials including Lennard-Jones argon, two square-well fluids, and SPC water. It was demonstrated that the CG-MMC method formally satisfies detailed balance at the coarse level (1) if particle moves are selected by choosing origination cells randomly and (2) if moves are accepted/rejected according to the standard Metropolis criterion in which the coarse-grained (free) energy is substituted for the usual potential energy. The resulting CG-MMC simulations were shown to be orders-of-magnitude faster than full-resolution simulations in attaining equilibrium configurations in a two-phase vapor-liquid system; the precise degree of speed-up is a function of the coarse-graining level.

In this Chapter, we investigate the applicability of CG-MMC to simulate non-equilibrium phenomena. The use of Metropolis Monte Carlo to study non-equilibrium phenomena is well established in the literature [1-3]. In essence, it can be shown that particle trajectories in MMC simulations are consistent with those generated by the overdamped (inertialess) Langevin equation, subject to the constraint that the maximum move attempts in MMC are sufficiently small; details of this equivalence are discussed in

Section 4.2. Our principal aim in this Chapter is to determine whether this equivalence can be retained once the coarse-graining transformation is applied.

Three variants of a simple system, namely a one-dimensional Gaussian pulse spreading in time, are used to develop, analyze and validate the non-equilibrium CG-MMC (NECG-MMC) method. In the first variant, we consider the diffusive evolution of the pulse assuming that the particles are ideal and that no external potential energy field exists. In the second variant, we consider the drift-diffusion behavior of the same pulse by applying an external potential energy field to the system. Finally, we consider the drift-diffusion behavior of a Gaussian pulse comprised of LJ-Ar particles governed by the same potential defined in Chapter 2. The remainder of the Chapter is organized as follows. In Section 4.2, a brief summary is provided of the connection between MMC and overdamped Langevin trajectories. In Section 4.3, the NECG-MMC method is motivated and introduced; the three computational experiments validating the approach described in Section 4.4.

4.2 Metropolis Monte Carlo as a Generator for Overdamped Langevin Dynamics

As mentioned in Section 4.1, the relationship between MMC and overdamped Langevin (or Brownian) dynamics has been well established by previous work applied to magnetic dynamics [4, 5], proteins [6], and vacancy cluster diffusion [7]. Here, we provide a brief summary of the pertinent points and follow closely the development in refs. [8, 9].

Consider the temporal evolution of *P(X,t)*, the probability of a one-dimensional Markovian system residing at coordinate *X* at time *t*, which is most generally given by the Master equation

$$\frac{\partial P(X,t)}{\partial t} = \int \psi(X';\Delta X) P(X',t) d(\Delta X) - \int \psi(X;\Delta X) P(X,t) d(\Delta X), \qquad (4.1)$$

where $\psi(X;\Delta X)$ is the transition rate over a small but finite time interval, Δt, and $\Delta X \equiv X - X'$. For small transitions, ΔX, the Master equation can be approximated by a Fokker-Planck equation (FPE) of the form [10, 11]

$$\frac{\partial P(X,t)}{\partial t} \approx -\frac{\partial}{\partial X}\left[A(X)P(X,t)\right] + \frac{1}{2}\frac{\partial^2}{\partial X^2}\left[B(X)P(X,t)\right]. \qquad (4.2)$$

where

$$A(X) \equiv \int_{-\infty}^{\infty} (\Delta X)\psi(X;\Delta X) d(\Delta X) = \frac{\langle \Delta X \rangle}{\Delta t}, \qquad (4.3)$$

and

$$B(X) \equiv \int_{-\infty}^{\infty} (\Delta X)^2 \psi(X;\Delta X) d(\Delta X) = \frac{\langle (\Delta X)^2 \rangle}{\Delta t}, \qquad (4.4)$$

are drift and diffusion coefficients, respectively. In other words, the drift and diffusion coefficients, which may generally be functions of position and time, are the mean displacement and mean-square displacement over some arbitrary (small) time interval, Δt.

We now consider the mean displacement and mean-square displacement that arise from executing a series of Metropolis Monte Carlo moves for which $rd_{\max}$ is the maximum MMC (attempted) displacement and ξ is a uniform random number in the interval [-1,1]. The corresponding change in potential energy is $\Delta U = \frac{\partial U}{\partial X}\Delta X = \frac{\partial U}{\partial X}\left(rd_{\max}\,\xi\right)$. It can then be shown [8, 9] that the mean displacement, $<\Delta X>$, and mean-square displacement, $<(\Delta X)^2>$, corresponding to MMC moves can then be expressed in terms of a series expansion, i.e.,

$$\left\langle \Delta X \right\rangle \approx -\frac{1}{k_B T}\frac{\partial U}{\partial X}\frac{\left(rd_{\max}\right)^2}{6} + \left(\frac{1}{k_B T}\frac{\partial U}{\partial X}\right)^2 \frac{\left(rd_{\max}\right)^3}{16} + O\left(rd_{\max}\right)^4 \tag{4.5}$$

and

$$\left\langle \left(\Delta X\right)^2 \right\rangle \approx \frac{\left(rd_{\max}\right)^2}{3} - \frac{1}{k_B T}\frac{\partial U}{\partial X}\frac{\left(rd_{\max}\right)^3}{8} + O\left(rd_{\max}\right)^4. \tag{4.6}$$

Considering the first term only in each of the preceding two equations and considering the form of the FPE in eq. (4.2) gives

$$B(X) = \frac{\left(rd_{\max}\right)^2}{3\Delta t} = 2D, \tag{4.7}$$

and therefore that

$$A(X) = -\frac{D}{k_B T}\left(\frac{\partial U}{\partial X}\right) = -\frac{1}{\gamma}\left(\frac{\partial U}{\partial X}\right), \tag{4.8}$$

where $D / k_B T = 1/\gamma$ is the Einstein relationship and γ is the damping, or friction coefficient. In other words, *A(X)* and *B(X)* correspond to the standard definition of drift and diffusion coefficients in overdamped Langevin dynamics (LD), if the assumed truncation in eqs. (4.7) and (4.8) is valid. Of course, this does not imply that MMC particle trajectories are equivalent to LD trajectories on a per-move basis, but rather that the equivalence is valid over a sufficient number of moves to properly define the averages of the mean displacement and mean-square displacement in eqs. (4.5) and (4.6), respectively.

For larger $rd_{\max}$, the MMC-LD equivalence is no longer valid because the additional terms in the expansions in eqs. (4.3) and (4.4) become important, and the trajectories implied by MMC are no longer consistent with Langevin trajectories [12]. However, dividing the leading order term in eq. (4.5) (or eq. (4.6)) by the next term in the expansion provides a criterion that sets a limit on the MMC move size that ensures the MMC-LD equivalency:

$$K \equiv \frac{3}{8}\frac{\partial U}{\partial X}\frac{rd_{\max}}{k_B T} << 1. \tag{4.9}$$

A principal implication of eq. (4.9) is that the maximum allowable move size in an MMC simulation is limited by the magnitude of the gradients in the potential energy landscape, i.e., $\left|\partial E / \partial X\right|$. Thus, for interaction potentials in which inter-particle attractions are short-ranged and steep, only very small moves can be accommodated if non-equilibrium trajectories are to be meaningful. What are the implications for NECG-MMC, where the minimum particle displacement is equal to the length of a coarse cell? Obviously, for the cell sizes considered in Chapters 2 and 3, the criterion in (4.9) is not satisfied when considering the LJ-Ar and SPC-water potentials. However, we hypothesize here that this criterion must be modified to reflect the fact that the potential energy landscape is no longer relevant once a system is spatially coarse-grained, and that the relevant criterion is now

$$K \equiv \frac{3}{8}\frac{\partial A_{CG}(L_{cell})}{\partial X}\frac{rd_{\max}}{k_B T} << 1, \tag{4.10}$$

where $A_{CG}(L_{cell})$ is the free energy landscape at a given coarse-graining level defined by the coarse cell size, L_{cell}. We further speculate that the gradients in $A_{CG}(L_{cell})$ are much smaller than the original potential energy landscape and that they scale with L_{cell} so that the criterion in eq. (4.10) is satisfied at all coarse-graining levels, at least for nearest-neighbor moves. These hypotheses will be tested empirically in the remainder of the Chapter.

We conclude this Section by making explicit the fact that the equivalence between MMC and LD trajectories (over a large enough time interval) implies a linear relationship between the number of MMC moves and "time". While the particular value of this scaling factor is not important for the ensuing analysis we note that a Monte Carlo diffusion coefficient, *D*, can be defined as

$$\tau = \frac{L_{cell}^2}{D} \tag{4.11}$$

where τ represents the time step corresponding to one CG-MMC move.

4.3 The Non-Equilibrium CG-MMC (NECG-MMC) Method

In Section 4.2, it was demonstrated that if the Metropolis criterion was applied using the coarse-grained free energy, $A_{CG}(\mathbf{n})$, detailed balance was satisfied in a CG-MMC simulation if transtions between coarse states were selected by moving particles between randomly chosen cells. Recall that a coarse state is represented by an *M*-dimensional vector $\mathbf{n} = (n_1, n_2, ..., n_M)$ that defines the cell occupancies, n_k, within the simulation domain. As noted earlier in this Chapter, the satisfaction of detailed balance does not generally have bearing on the nature of the trajectories in phase space on the way to equilibrium.

A qualitative analysis shows that some measure of inconsistency between MMC and CG-MMC is expected along non-equilibirum trajectories. Figure 4.1 shows a schematic representation of a simple, one-dimensional, non-equilibrium system in which a concentration gradient is present across the simulation domain. The top row represents a standard full-resolution simulation on which coarse cell boundaries are superposed for reference, while the lower row represents a CG-MMC simulation with an equivalent density distribution (at the coarse level). In the MMC simulation, random particle selection naturally leads to a bias towards cells that contain more particles. In CG-MMC, however, random cell selection leads to a bias in which particles in less occupied cells are more likely to be picked.

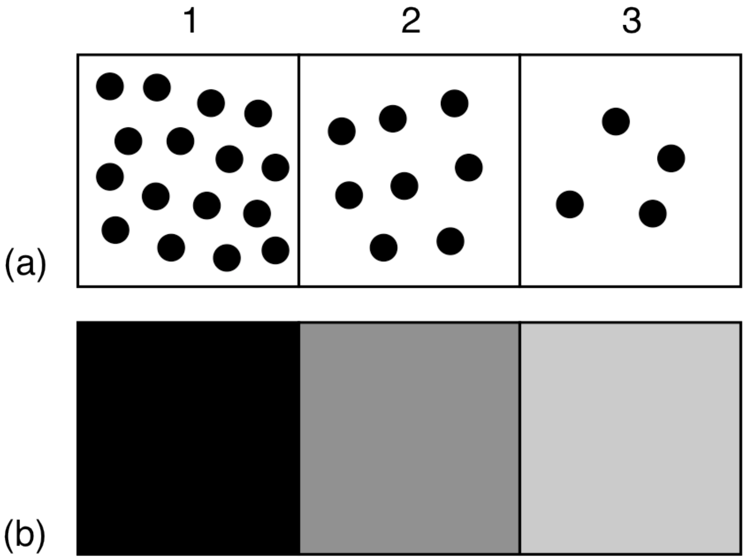

Figure 4.1: Schematic representation of a one-dimensional non-equilibrium system containing a concentration gradient. (a) Full-resolution MMC representation, and (b) CG-MMC representation, where the grey shade denotes the occupancy in each cell.

Attempting to correct this bias by simply choosing origination cells according to their particle occupancy violates detailed balance. This can be trivially demonstrated by considering the probability of selecting a transition from coarse state *i* to *j*, a_{ij}, which we arbitrarily assign to a particle moving from cell *k* to cell *l*, i.e., $\mathbf{n}(i) \equiv (n_1, ..., n_k, n_l, ..., n_M)$ and $\mathbf{n}(j) \equiv (n_1, ..., (n_k - 1), (n_l + 1), ..., n_M)$. Biasing the choice of cell by its occupancy implies $a_{ij} = n_k / N$, where is the total number of particles in the system. The probability of selecting the reverse process becomes $a_{ji} = (n_l + 1) / N$, i.e., $a_{ij} \neq a_{ji}$ and detailed balance is no longer satisfied.

We therefore seek a way to choose origination cells in a manner that is biased by their occupancy and then either (1) remove the bias using the acceptance criterion, or (2) remove the bias by ensuring that the reverse process is equally biased. While approach (1) is certainly possible in concept, here we propose a simple solution based on approach (2). In essence for each transition between two coarse states *i* and *j* (forward or backward), the transition selection probability is biased by the maximum of the cell occupancies either before or after the transition. In other words, the transition probabilities now become

$$a_{ij} = a_{ji} = \frac{\max\left(n_k,\, n_l + 1\right)}{\sum_{k=1}^{M} \sum_{hop=1}^{6} \max\left(n_k,\, n_l + 1\right)}, \tag{4.12}$$

where the denominator $P = \sum_{k=1}^{M} \sum_{hop=1}^{6} \max\left(n_k,\, n_l + 1\right)$ is a normalization factor. Note that the equal bias applied to both forward and backward transitions between the two coarse states automatically guarantees that detailed balance is satisfied. Moreover, the bias ensures that move attempts are more likely from (and to) cells with high particle occupancy.

The validity of eq. (4.12) for performing non-equilibrium CG-MMC (NECG-MMC) simulations is confirmed empirically using a suite of tests that are described in Section 4.3. However, the implementation of eq. (4.12) requires additional algorithmic considerations that are described next.

4.3.1 Implementation of the NECG-MMC Algorithm

Equation (4.12) requires that every allowable transition between all pairs of cells be assigned a bias based on the maximum particle density in each each pair of cells. The particular transition to be attempted at each move must then be chosen from a list of all possible transitions in a biased stochastic manner. In fact, this task is essentially identical to the event selection component within a kinetic Monte Carlo simulation in which all possiblre events and their rates are first defined and then selected in a biased random approach. Various methods have been developed to increase the efficiency of event selection, including binary search.

The NECG-MMC algorithm as implemented in this thesis proceeds as follows:

1) Start from an initial coarse state i_0 represented by the M-dimensional vector $\mathbf{n}\left(i_0\right) \equiv \left(n_1, n_2, ..., n_M\right)$.
2) Generate a list of all possible events (i.e., transitions) and populate an initial database of attempt probabilities for each event according to eq. (4.12).
3) Calculate the current sum of all attempt probabilities, $P = \sum_{k=1}^{M} \sum_{hop=1}^{6} \max\left(n_k,\, n_l + 1\right)$.
4) Choose an event based on its attempt probability. The origination and destination coarse cell are determined accordingly by generating a uniformly distributed random number $U[0,1]$. Select an event *r*, which represents a particle move between cells (*k*, *l*) according to the distribution of attempt probabilities, which is

given by $\sum_{k=1}^{r-1} \max\left(n_k, n_l+1\right) < U[0,1]P < \sum_{k=1}^{r} \max\left(n_k, n_l+1\right)$.

5) If origination cell k is not empty, i.e. $n_k > 0$, and destination cell l doesn't exceed the maximum occupancy, i.e. $n_l < n_{\max}$, execute the event attempt by moving one particle from cell k to l. Otherwise go back to step 4) and re-select cell k or l until both meet the requirements.

6) Evaluate the free energy change associated with this event using eq. (2.15), i.e.,

$$\Delta A\left(i \rightarrow j\right) = k_B T \ln \frac{n_l+1}{n_k} + \Delta A_{\text{input}}\left(n_l, n_{env,l}\right) - \Delta A_{\text{input}}\left(n_k - 1, n_{env,k}\right), \tag{4.13}$$

where $\Delta A_{\text{input}}\left(n_k, n_{env,k}\right)$ represents the excess free energy change due to one particle insertion into a cell with n_k particles and environment with $n_{env,k}$ particles (see Figure 2.4 for system setup and Figures 2.5, 2.6 and 2.7 for excess free energy change surfaces), i.e. $\Delta A_{\text{input}}\left(n_k, n_{env,k}\right) = \Delta A_{ex}\left(n_k \rightarrow n_k + 1 : n_{env,k}\right)$. It also highlights the fact that the numerically averaged CG potential is the only input in the CG-MMC model.

7) Accept this move with probability α_{ij}, following eq. (2.17). This is realized by generating another uniformly distributed random number ζ in $U[0,1]$. If $\alpha_{ij} < \zeta$, then remain in old state i otherwise if $\alpha_{ij} \geq \zeta$, accept the new state j:

$$\alpha_{ij} = \min\left[\exp\left(-\beta \Delta A(i \rightarrow j)\right), 1\right] \tag{4.14}$$

8) Update the occupancy of origination and destination cells, the database of attempt probabilities for coarse cells within interaction range, and the renormalization

factor P.

9) The NECG-MMC iterations continue by repeating steps 4 – 8.

The NECG-MMC algorithm described above is shown schematically in Figure 4.2.

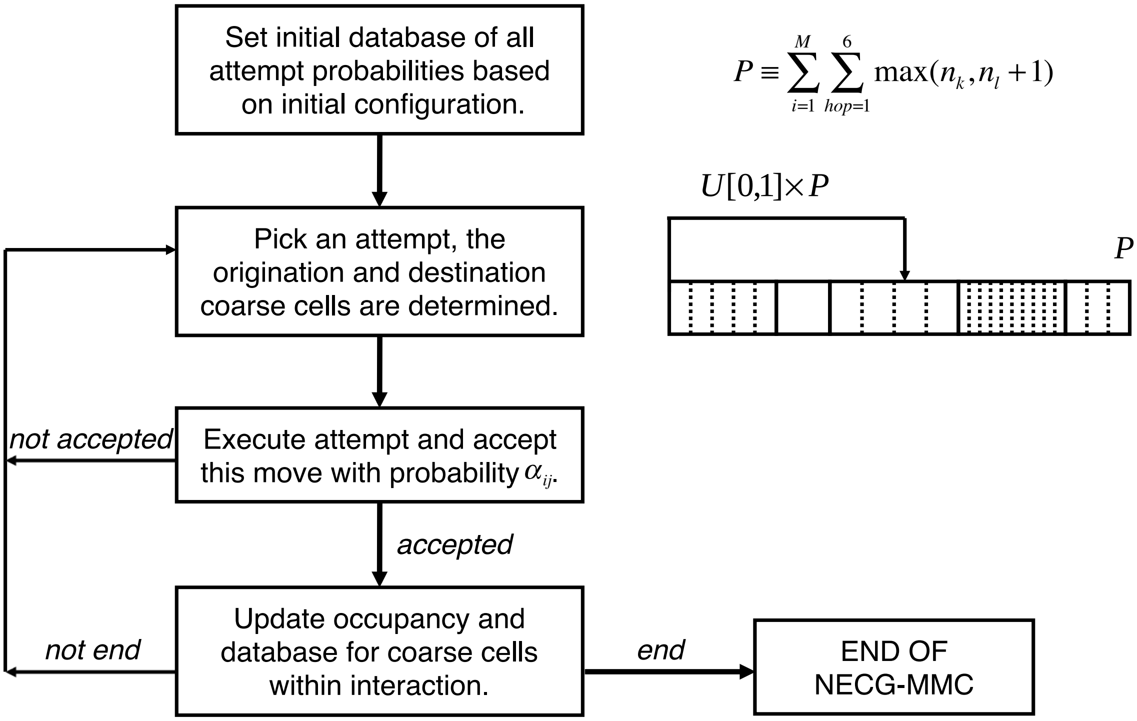

Figure 4.2: Schematic representation of NECG-MMC with biased coarse cell selection algorithm.

4.4 Validation of the NECG-MMC Method

Consider again the Fokker-Planck equation in Section 4.2 (eq. (4.2)) into which the results from eqs. (4.7) and (4.8) are substituted:

$$\frac{\partial P\left(X,t\right)}{\partial t}=\frac{1}{\gamma}\frac{\partial}{\partial X}\left[\left(\frac{\partial U}{\partial X}\right)P(X,t)\right]+\frac{\partial^2}{\partial X^2}\left[D(X)P(X,t)\right]. \tag{4.15}$$

Assuming further that that the diffusion coefficient is not a function of position (or time) and removing the explicit dependence of the distribution on position and time gives the following convection-diffusion equation:

$$\frac{\partial P}{\partial t}=-\frac{\partial}{\partial X}\left[\frac{F}{\gamma}P\right]+D\frac{\partial^2 P}{\partial X^2}, \tag{4.16}$$

where $F=-(\partial U/\partial X)$ is the force acting on the system due to an external potential. Recall again that the diffusion coefficient also is related to the friction coefficient, γ , by the Einstein relationship, $D/k_BT=1/\gamma$.

For the special case of zero external potential, eq. (4.16) reduces to

$$\frac{\partial P}{\partial t}=D\frac{\partial^2 P}{\partial X^2}, \tag{4.17}$$

which describes a transient diffusion process in one dimension. We consider here a situation in which the initial condition at time t_0 corresponds to a Gaussian pulse

$$P(X,t_0)=\exp\left(-\frac{X^2}{4Dt_0}\right), \tag{4.18}$$

with boundary conditions

$$P(\pm X_0,t)=\sqrt{\frac{t_0}{t}}\exp\left(-\frac{X_0^2}{4Dt}\right). \tag{4.19}$$

The solution of eq. (4.17) with initial and boundary conditions (4.18) and (4.19) possesses an analytical solution

$$P(X,t)=\sqrt{\frac{t_0}{t}}\exp\left(-\frac{X^2}{4Dt}\right). \tag{4.20}$$

In the following sections we execute and analyze CG-MMC and NECG-MMC simulations of the spreading of a one-dimensional Gaussian pulse both with and without the application of an external potential.

4.4.1 Ideal Gas – Pure Diffusion (No External Potential)

Our base system consists of a rectangular domain comprised of 5 coarse cells in the *Y* and *Z* directions, which are perpendicular to the concentration gradient, and subject to periodic boundary conditions. The length of the domain in the *X* direction, along which the primary diffusion is occurring, is 1000 coarse cells. For the case of an ideal gas, which we consider here, the coarse cells are defined to be of unit length and the temperature is (arbitrarily) specified to be 1.2 in consistent units. The intial Gaussian particle distribution function is given by

$$N(X,t_0) = 250\exp\left(-\frac{(X-500)^2}{800}\right), \tag{4.21}$$

where *N* is the number of particles in a cell with center-of-mass located at *X*; a side-view of the central part of the simulation domain is shown in Figure 4.3.

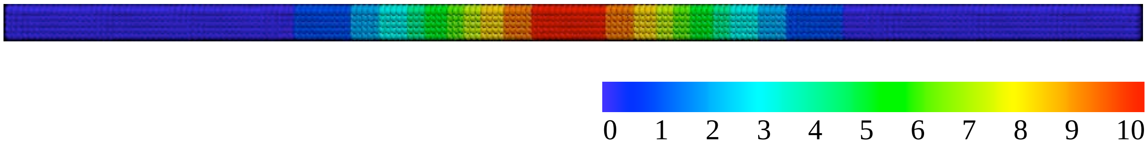

Figure 4.3: Simulation domain with initial Gaussian density distribution. Only the middle 200 planes of the rectangular $5\times5\times1000$ cell system is shown for clarity. The cell color denotes particle number that ranges from zero (dark blue) to 10 (red). The color

scale is provided on the side.

Results for the evolution of the Gaussian initial condition are shown for both CG-MMC and NECG-MMC in Figures 4.4 and 4.5, respectively. In both figures, the (red) symbols represent the simulation configuration after 2x10^8 moves, while the solid line shows a Gaussian fit to the simulation data. The distribution height value denoted by "count" in the figures is computed by area-normalizing the distribution so that the area is equal to the total number of particles in the coarse-grained system. In all ideal gas simulations, the total number of particles is given by the integral of the function in eq. (4.21), $N_T = 12400$.

While the CG-MMC distribution exhibits clear deviations from the Gaussian fit, the NECG-MMC distribution is essentially perfectly Gaussian as expected from the analytical solution in eq. (4.20). The CG-MMC deviations are particularly pronounced at the tails of the distribution, where anomalously rapid diffusion is evident. This observation is consistent with the fact that in CG-MMC all cells are equally likely to be chosen to originate particle moves, which effectively increases the diffusivity of particles in low-occupancy cells. Thus, for an ideal gas evolving without an external potential, the NECG-MMC algorithm appears to provide an excellent representation of non-equilibrium "dynamics".

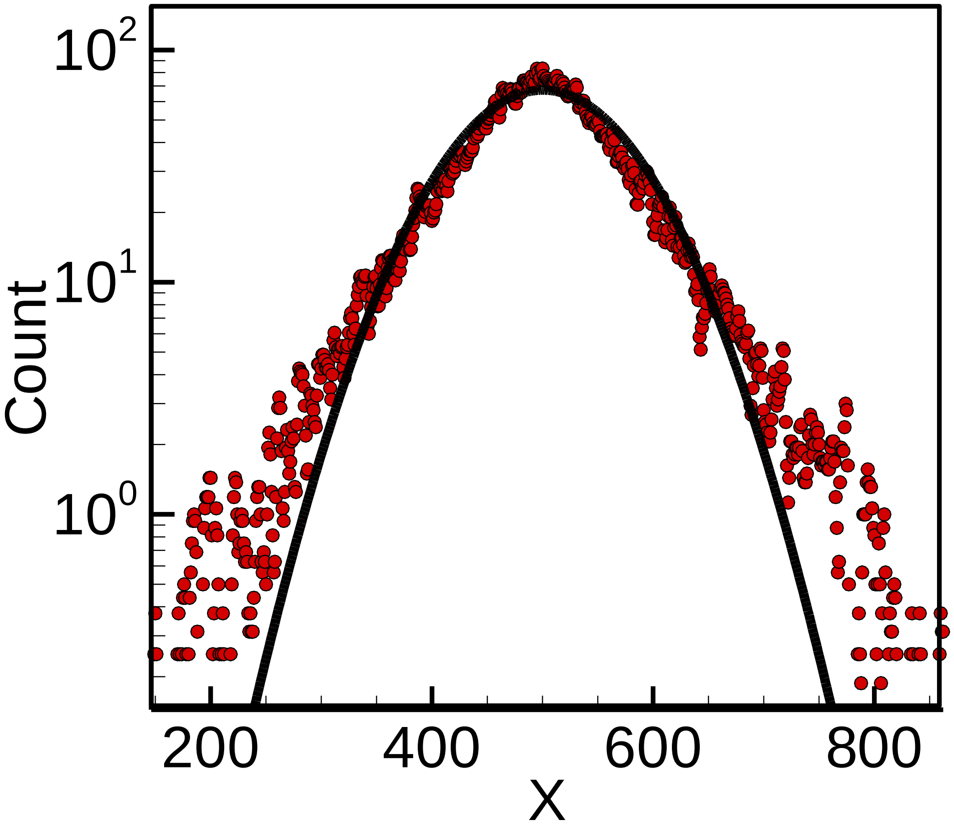

Figure 4.4: Area-normalized particle density distribution after 2×10^8 CG-MMC steps (see text for initial condition). Red circles – CG-MMC simulation; black line – Gaussian fit.

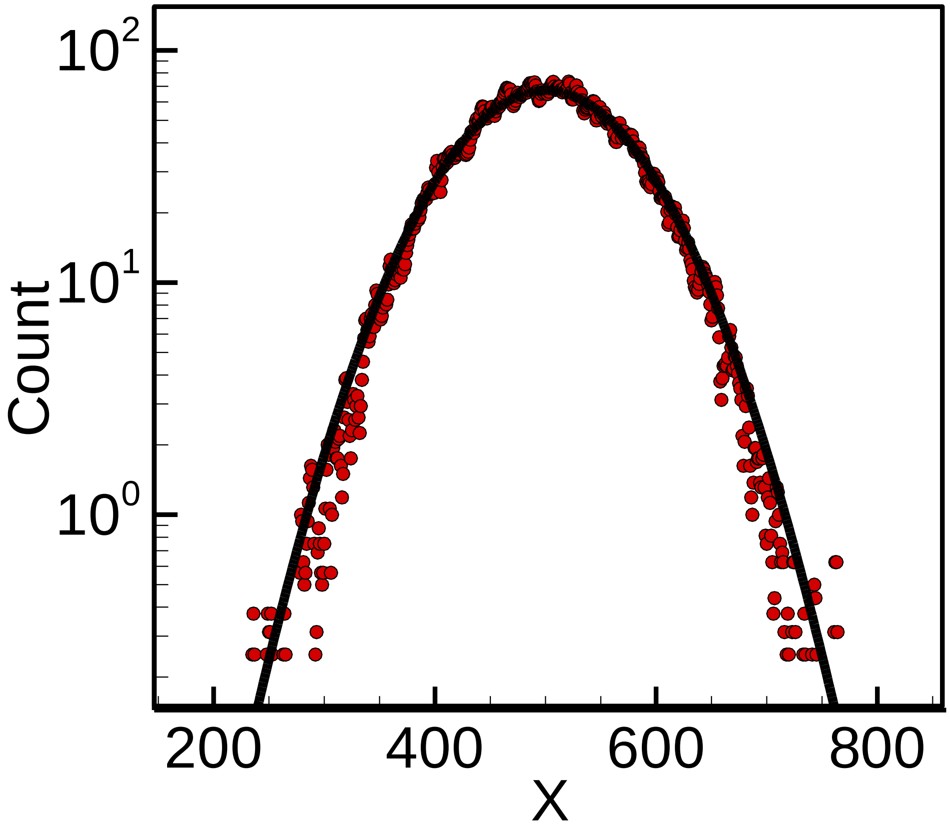

Figure 4.5: Area-normalized particle density distribution after 2×10^8 NECG-MMC steps (see text for initial condition). Red circles – NECG-MMC simulation; black line – Gaussian fit.

4.4.2 Ideal Gas – Drift and Diffusion (with External Potential)

Next, we consider the same situation as described in the previous section but with the additional application of an external potential field of the form

$$U(X) = 0.1 \times n(X) \times X \,, \tag{4.22}$$

where *n* is the number of particles in cells located at position *X*. The Gaussian initial distribution is now subjected to a constant drift velocity in addition to the background diffusion encountered in the first example.

The results for CG-MMC and NECG-MMC simulations of this system are shown in Figure 4.6. Here, the circle symbols show the CG-MMC (blue) and NECG-MMC (red) distributions after 2×10^8 steps. The solid black line denotes the initial configuration. While both distributions are affected strongly by the presence of the external potential field, the NECG-MMC shows that the profile remains Gaussian as it translates along the potential gradient. On the other hand, the CG-MMC distribution becomes strongly skewed with a long leading tail, while the peak moves much more slowly. It is easy to show that the NECG-MMC prediction is in fact correct by considering the analytical solution of eq. (4.20), which is a Gaussian spreading at the same rate as that shown in eq. (4.20) but with a translation velocity that corresponds to [13]:

$$v = \frac{F \cdot D}{k_B T}\,, \tag{4.23}$$

where as mentioned earlier, the force, *F*, is the gradient of the potential, i.e., $F = -(\partial U / \partial X)$. With the same initial condition as eq. (4.18), a similar analytical solution can be obtained for the drift-diffusion case in eq. (4.16):

$$P(X,t) = \sqrt{\frac{t_0}{t}}\exp\left(-\frac{\left(X - v(t-t_0)\right)^2}{4Dt}\right). \tag{4.24}$$

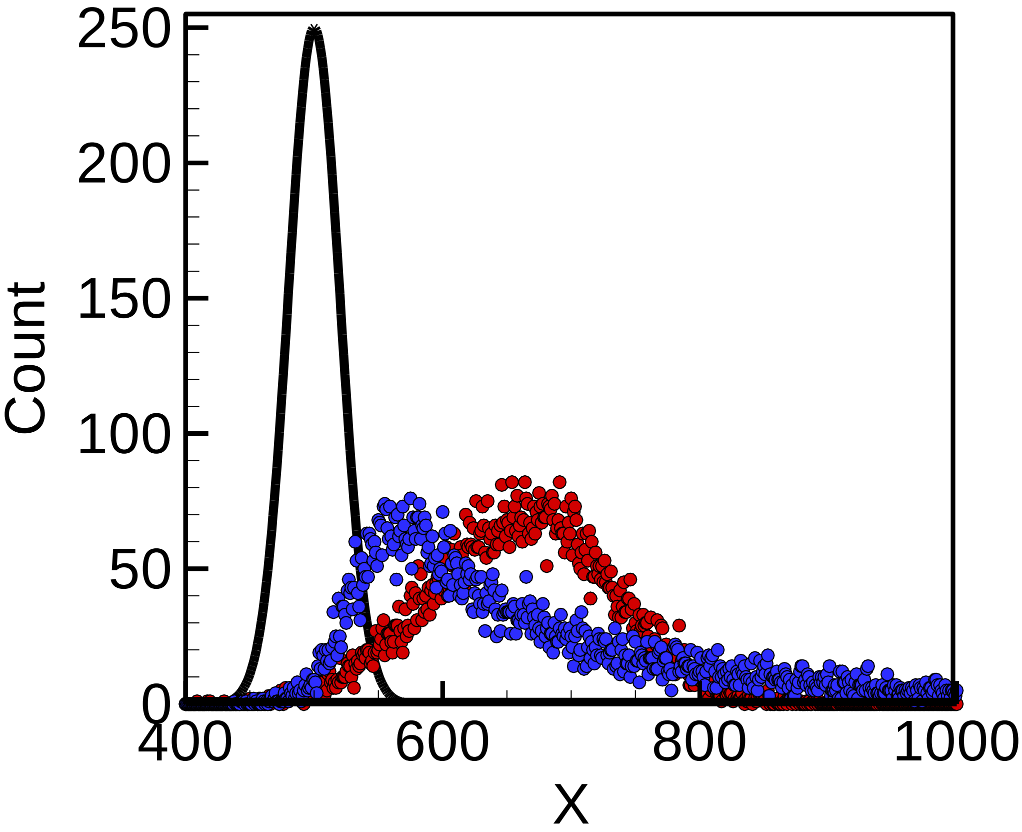

Figure 4.6: Area-normalized particle density distribution after 2×10^{8} CG-MMC (blue circles) and NECG-MMC (red circles) steps for an ideal gas diffusive system with an applied external potential field (see text for definitions). Black line – Gaussian fit of the initial condition.

The analytical solutions in eqs. (4.20) and (4.24) show that $4Dt = 2\sigma_t^2$, where σ_t is the standard deviation of Gaussian distribution at time *t*. Figure 4.7 shows the simulation time as a function of corresponding NECG-MMC steps. There exists a linear relationship between the simulation time and NECG-MMC steps. The linear fit function is $4Dt = 4.55 + 7.24S$, where S is the number of NECG-MMC steps.

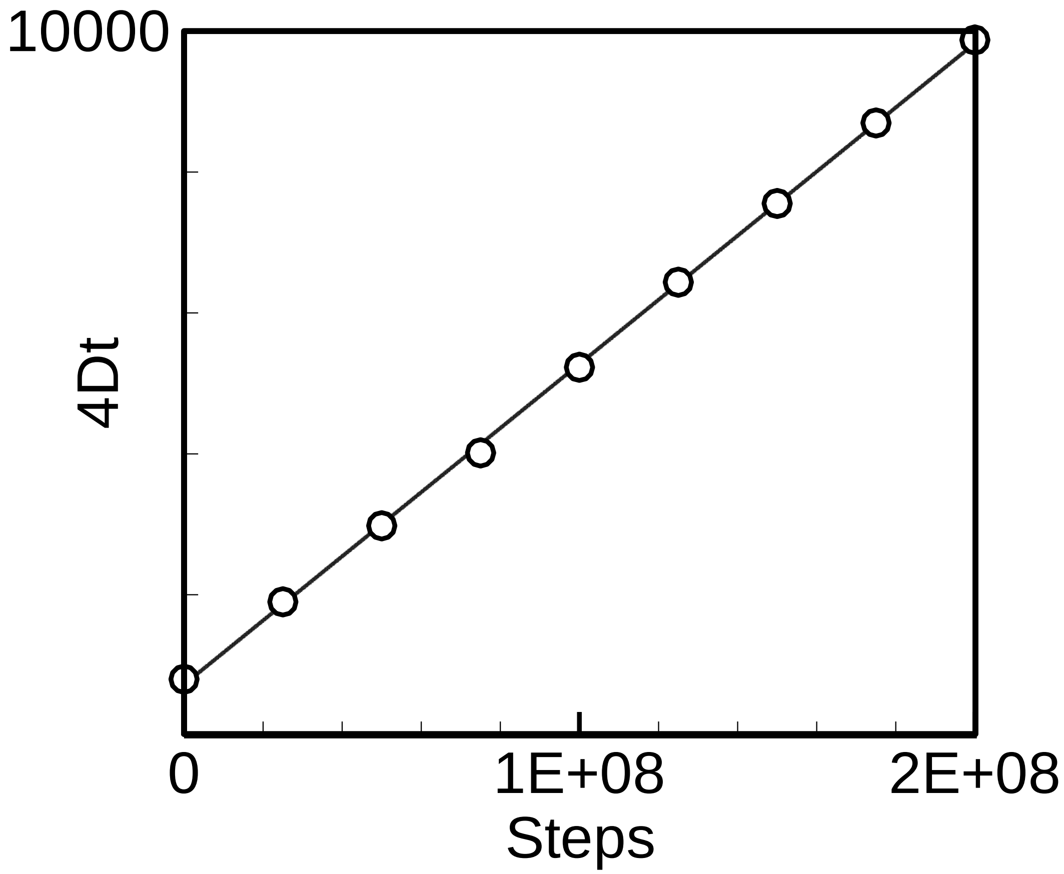

Figure 4.7: Simulation time as a function of NECG-MMC steps. All data collected from ideal gas pure diffusion process using NECG-MMC model. Black line – Linear fit.

By comparing to the initial condition in the analytical solution at time t_0 in eq. (4.18), the initial condition in eq. (4.21) gives $4Dt_0 = 800$, which sets the value of the initial time t_0. After 2×10^8 NECG-MMC steps, the linear fit between simulation time and NECG-MMC steps gives $4Dt = 2\sigma_t^2 = 9828$. Therefore, the time change can be determined from the diffusion process: $D(t-t_0) = 2257$.

To see whether the drift process is correctly captured, we need to see whether the shift of the peak in the simulation matches the analytical result calculated at the "time" determined by NECG-MMC steps. The shift of the peak from its original location $X_{t_0} = 500$ can be calculated as $\Delta X_t = v(t - t_0)$ by following the analytical solution (4.24). As $F = 0.1$, $k_B T = 1.2$, and $D(t - t_0) = 2257$, the shift of the peak can be calculated as $\Delta X_t = v(t - t_0) = \dfrac{F}{k_B T} D(t - t_0) = 188$. In Figure 4.6, the location of the peak from the simulation reads as $X_t = 685$, which is consistent with the analytical result $X_t = X_{t_0} + \Delta X_t = 688$ at time corresponding to 2×10^8 NECG-MMC steps derived from diffusion.

4.4.3 Lennard-Jones-Argon – Drift and Diffusion with Inter-Particle Potential

In this section, we again consider the evolution of the Gaussian distribution function under an externally applied potential field but now include an inter-particle potential. Note that the Master equation that would describe the evolution in this system does not possess an analytical solution, and our primary aim will be to qualitatively compare the predictions between CG-MMC and NECG-MMC simulations to demonstrate that our findings from the previous examples still hold when inter-particle interactions are present. Specifically, we apply the LJ-Ar potential described in Chapter 2 (eq. (2.21). For this example, the coarse cell size is chosen to be $L_{cell} = 3\sigma$. The simulation temperature is set at $T^* = 1.2$, corresponding to supercritical conditions, in order to simplify the analysis.

The predicted position of the initial Gaussian distribution function after 1×10^8 steps is shown in Figure 4.8 for both CG-MMC (blue) and NECG-MMC (red).

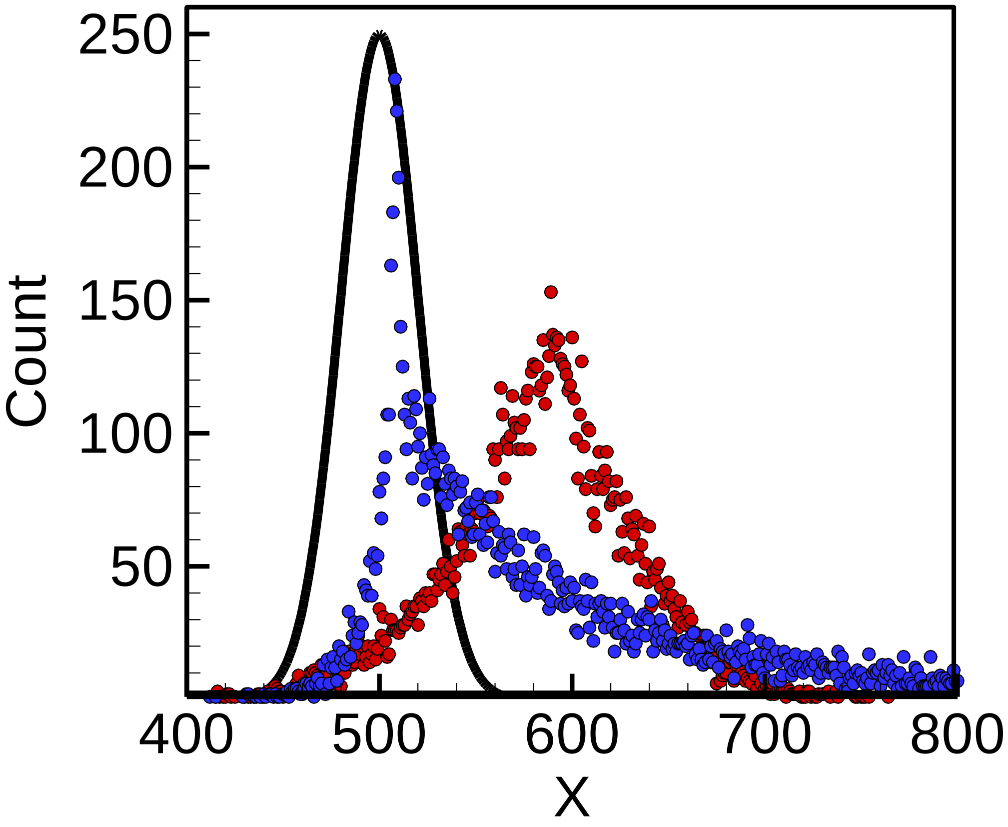

Figure 4.8: Area-normalized particle density distribution after 1×10^8 CG-MMC (blue circles) and NECG-MMC (red circles) steps for an LJ-Ar diffusive system with an applied external potential field (see text for definitions). Black line – Gaussian fit of the initial condition.

The NECG-MMC profile in this case is longer Gaussian because of the inter-particle attraction, but it still retains symmetry about the peak. Moreover, for the drift process, a translation velocity for the peak of the distribution can be clearly defined as eq. (4.23) and the location of the peak reads as $X_t = 592$, which is again consistent with the analytical result $X_t = X_{t_0} + \Delta X_t = 594$ at time corresponding to 1×10^8 NECG-MMC steps derived from diffusion. Once again, the CG-MMC result exhibits strong deviation from this behavior, and the peak of the distribution barely moves over the length of the simulation.

4.5 Diffusion at Different Coarse-Graining Levels

We conclude this Chapter by further analyzing the use of the NECG-MMC method for non-equilibrium simulations with a sequence of ideal-gas, pure diffusion simulations at different coarse-graining levels. We consider again the system described in Section 4.4.1, but now compare diffusion of a Gaussian distribution at several different coarse-graining levels. Recall that in Section 4.4.1 the cell size was set at $L_{cell} = 1$ and the overall domain was comprised of $5 \times 5 \times 1000$ coarse cells in the Y, Z, and X directions, respectively. We now consider the same domain at the following different coarse-graining levels: $L_{cell} = 1.25$ ($4 \times 4 \times 800$ coarse cells), $L_{cell} = 1.67$ ($3 \times 3 \times 600$ coarse cells), and $L_{cell} = 2.5$ ($2 \times 2 \times 400$ coarse cells).

In Figure 4.9 the initial Gaussian distribution is shown at some later time, *t*, which was chosen for each coarse-graining level such that all profiles were identical. For a diffusive system, the time change $\Delta t = t - t_0$ can be related to the number of NECG-MMC steps according to the relationship

$$\Delta t = \tau S = \frac{L_{cell}^2}{D} S \,, \tag{4.25}$$

where S is the number of NECG-MMC steps, τ is the time interval corresponding to one CG-MMC step, D is the diffusion coefficient, and L_{cell} is length of the coarse cell. In Table 4.1, the number of NECG-MMC steps required to reach the profile shown in Figure 4.9 is shown for each coarse-graining level. As expected for a properly coarse-grained system in which the diffusivity is independent of coarse-graining scale, the number of NECG-MMC steps multiplied by the square of the cell size corresponds to a fixed “time” across all coarse-graining levels.

L_{cell}	S	$\Delta t \propto L_{cell}^2 S$
1.0	5×10^7	5×10^7
1.25	3.2×10^7	5×10^7
1.67	1.8×10^7	5×10^7
2.5	0.8×10^7	5×10^7

Table 4.1: Equivalence of simulation time at different CG-MMC steps corresponding to different coarse-graining levels.

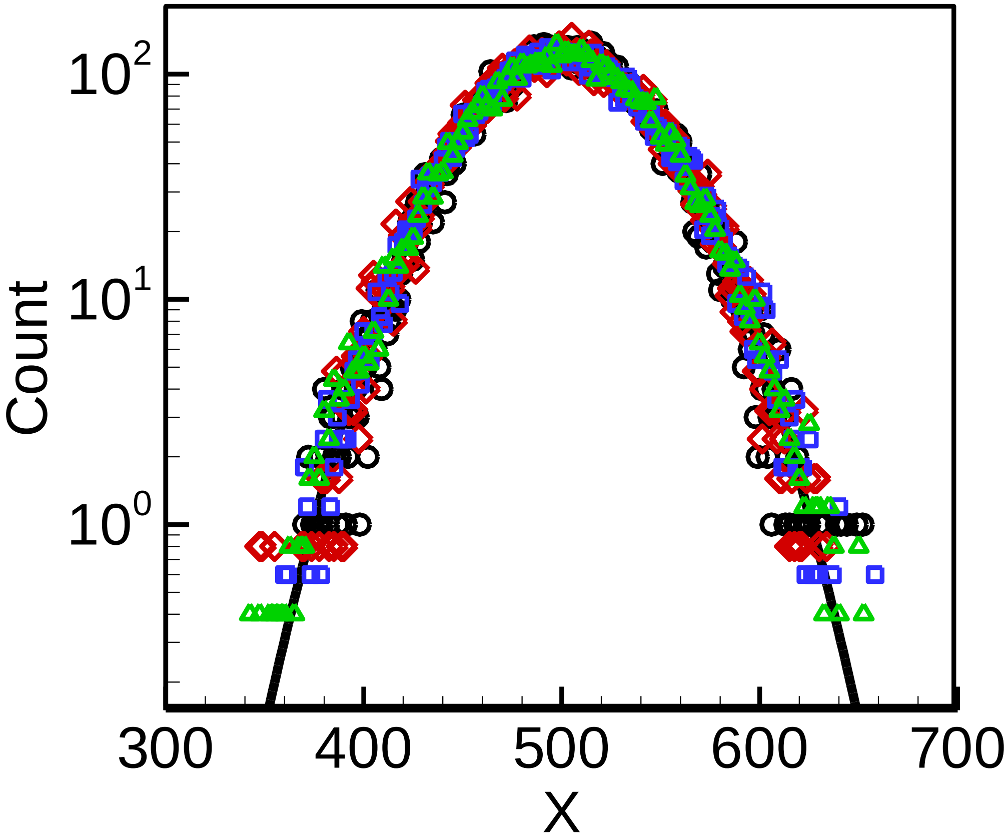

Figure 4.9: Distribution profiles obtained by NECG-MMC simulation after varying numbers of steps at several different coarse-graining levels. The number of steps were chosen to map all curves onto each other. The number of steps required at each coarse-graining level was: 5×10^7 at $L_{cell}=1$ (black circles), 3.2×10^7 at $L_{cell}=1.25$ (red diamonds), 1.8×10^7 at $L_{cell}=1.67$ (blue squares), and 0.8×10^7 at $L_{cell}=2.5$ (green deltas).

Snapshots of configurations at different coarse-graining levels corresponding to the same simulation time as in Figure 4.9 are shown in Figure 4.10. While the density distribution remains the same for simulations at different coarse-graining levels, the statistical fluctuations are clearly reduced at larger coarse-graining levels.

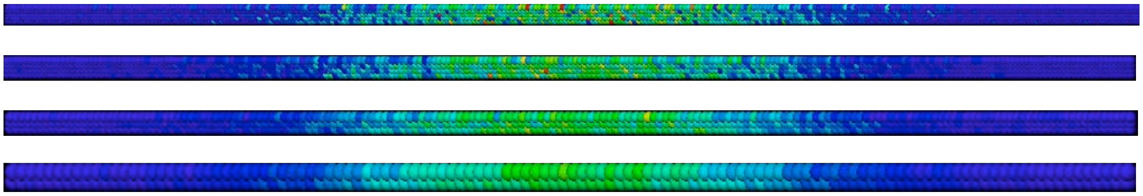

Figure 4.10: Configurations corresponding to the distributions in Figure 4.9 at different coarse-graining scales. Coarse-graining scale increases from top to bottom – see Figure 4.9 caption for details. Cell color denotes number density that ranges from low (dark blue) to high (red).

4.6 Conclusions

In this chapter, we presented a detailed discussion of the development and validation of a non-equilibrium version of coarse-grained Metropolis Monte Carlo method (NECG-MMC). The approach taken was to start with the original CG-MMC method that was shown to satisfy detailed balance, and then modify the cell selection process in such a way so as to not disturb the detailed balance condition for each possible move. The result is a method in which particle move attempts from each origination cell to destination cell are biased by the maximum density across the pair of cells. Thus, not only are particles moves from high density cells increased, but moves to high density cells are also increased. The latter result, while seemingly unintuitive, is the feature that enforces detailed balance for every possible move in the system.

We also reiterate that, at least from an algorithmic perspective, the NECG-MMC method is a hybrid between lattice kinetic Monte Carlo and Metropolis Monte Carlo. The biasing of every possible transition according to the maximum of the cell-pair density requires that all possible transitions be listed before a move can be selected. The transition attempt selection process can then be performed with established methods such as a binary search.

We certainly do not claim that the solution presented in this chapter for creating correct non-equilibrium trajectories at the coarse-grained level is unique, but we show using several examples that the approach does provide correct trajectories (at least at a given coarse-grained length scale). Using an ideal gas model, we show that the NECG-MMC trajectories in pure diffusion and drift-diffusion settings are completely consistent with analytical solutions to the corresponding Fokker-Planck equations. Equally significantly, we demonstrate that the CG-MMC method presented in Chapters 2 and 3 does not achieve this consistency. We then further validate the NECG-MMC method by simulating the drift-diffusion process of a supercritical Lennard-Jones Argon fluid. Once again, the NECG-MMC evolution exhibits a qualitatively reasonable trajectory, while the CG-MMC method leads to artifacts that are easily identified even though an analytical solution is not available.

References

---

[1] H. Mtiller-Krumbhaar and K. Binder, *J. Stat. Phys.* **8**, 1, (1973).

[2] W. R. Gilks and C. Berzuini, *R. Stat. Soc. Ser. B Stat. Methodol.* **63**, 127 (2001).

[3] H. E. A. Huitema and J. P. van der Eerden, *J. Chem. Phys.* **110**, 3267 (1999).

[4] X. Z. Cheng, M. B. A. Jalil, H. K. Lee, and Y. Okabe, *Phys. Rev. Lett.* **96**, 067208 **(**2006**)**.

[5] U. Nowak, R. W. Chantrell, and E. C. Kennedy, *Phys. Rev. Lett.* **84**, 163 **(**2000**)**.

[6] G. Tiana, L. Sutto, and R. A. Broglia, *Physica A* **380**, 241 **(**2007**)**.

[7] S. V. Khare, N. C. Bartelt, and T. L. Einstein, *Phys. Rev. Lett.* **75**, 2148 **(**1995**)**.

[8] K. Kikuchi, M. Yoshida, T. Maekawa, and H. Watanabe, *Chem. Phys. Lett.* **185**, 335 **(**1991**)**.

[9] R. T. Scarlett, J. C. Crocker, and T. Sinno, *J. Chem. Phys.* **132** (2010).

[10] R. K. Pathria, *Statistical Mechanics,* 2nd ed. (Elsevier Butterworth-Heinemann, Boston, 1996**)**.

[11] N. G. v. Kampen, *Stochastic Processes in Physics and Chemistry* (Elsevier, Amsterdam, 2007**)**.

[12] D. M. Heyes and A. C. Branka, *Mol. Phys.* **94**, 447 **(**1998**)**.

[13] H. Risken, *The Fokker-Planck Equation: Methods of Solution and Applications,* 2nd ed. (Springer, Berlin, 1996).

Chapter 5

Large-Scale Coarse-Grained Lattice Metropolis Monte Carlo Simulations

5.1 Introduction

In Chapters 2 and 3, a spatial coarse-graining method for Metropolis Monte Carlo (MMC) simulations was presented in which an arbitrary inter-particle potential is numerically coarse-grained to enable Monte Carlo simulations of fluid systems on a rigid lattice (CG-MMC). It was shown that the CG-MMC method was generally applicable to any type of interatomic potential, subject to the constraint that the potential range was smaller than the length of a single coarse cell. The CG-MMC method was then modified slightly in Chapter 4 to render it consistent with non-equilibrium trajectories. To accomplish this, we used and extended theoretical arguments that demonstrate the equivalence between standard, full-resolution MMC and Langevin trajectories. The resulting method, which was referred to as non-equilibrium coarse-grained Metropolis Monte Carlo, or NECG-MMC, was shown to provide excellent quantitative agreement between simulations and analytical solutions for a simple diffusion and drift-diffusion systems.

One key result of Chapter 3 was that the coarse-grained potentials generated at one coarse-graining scale could be upscaled (or downscaled) to another coarse-graining scale, thereby enabling the possibility of executing CG-MMC or NECG-MMC simulations at multiple coarse-graining scales without the need to pre-compute several different potentials. Upscaling is particularly useful at larger coarse-graining scales where the potential pre-computation becomes prohibitively expensive. CG-MMC simulations in Chapters 3 and 4 were executed for coarse cell sizes up to about 2 nm (or 6σ in the Lennard-Jones argon (LJ-Ar) length scale). At this scale, a liquid-state coarse cell contains about 200 particles. While this is a significant amount of coarse-graining, in the present chapter we investigate the properties of CG-MMC (or NECG-MMC) for much larger length scales.

While there is no conceptual difficulty in upscaling a coarse-grained potential to arbitrarily large coarse-graining levels, it is immediately obvious that the single-particle moves that have been used up to this point become highly inefficient for propagating the system as the number of particles per coarse cell increases. Our main focus in this chapter, therefore, is to extend the capability of spatial coarse-graining to multi-particle moves while retaining (1) the computational efficiency of a move, and (2) the accuracy of the method. In the demonstrations presented here, we consider LJ-Ar simulations in which the coarse cells are scaled up to a size of almost 10 nm, and contain over 10,000 particles each in the liquid state. In particular, we use a simulation of three-dimensional spinodal decomposition of a homogeneous (LJ-Ar) fluid to highlight how CG-MMC can be used in an adaptively multiscale setting

5.2 Multi-Particle Moves

Recall that in Chapter 2, the coarse-grained potential was computed in terms of a chemical potential, or a free energy difference that results upon the insertion of one particle into a coarse-grained cell with particle density, ρ, surrounded by an environment density, ρ_{env}, and at temperature *T*. Here, we seek to derive an expression for the free energy change due to a multiple particle insertion in terms of the coarse-grained potentials that were already computed.

We begin by restating the canonical partition function in the coarse-grained state space

$$Q_{CG}(N,V,T)=\frac{1}{\Lambda^{3N}N!}\sum_{k}\exp\left(-\frac{A_{CG}(\mathbf{n})}{k_BT}\right), \tag{5.1}$$

where the coarse-grained system free energy is defined as $A_{CG}(\mathbf{n})=\sum_{k=1}^{M}A_k$, and A_k is the free energy in coarse cell *k*. Now consider the Helmholtz free energy in a system containing *N* particles at volume *V* and temperature *T*:

$$\begin{aligned}A(N,V,T)&=-k_BT\ln Q\\&=-k_BT\ln\left(\frac{V^N}{\Lambda^{3N}N!}\right)-k_BT\ln\left(\int dr^N\exp\left[-\frac{U(r^N)}{k_BT}\right]\right),\\&\equiv A_{id}(N,V,T)+A_{ex}(N,V,T)\end{aligned} \tag{5.2}$$

where "*id*" and "*ex*" refer to ideal and excess contributions, respectively. The Helmholtz free energy change upon the addition of *n* particles to the system is therefore given by

$$\begin{aligned}\Delta A(N\rightarrow N+n)&=-k_BT\ln Q_{N+n}/Q_N\\&=-k_BT\ln\left(\frac{V^n/\Lambda^{3n}}{(N+1)...(N+n)}\right)-k_BT\ln\left(\frac{\int dr^{N+n}\exp[-U(r^{N+n})/k_BT]}{\int dr^{N+n}\exp[-U(r^N)/k_BT]}\right).\\&=\sum_{i=1}^{n}\Delta A(N+i-1\rightarrow N+i)\end{aligned} \tag{5.3}$$

In other words, an *n*-particle insertion into a coarse cell can be regarded simply as a sum of *n* single particle insertions. Similar considerations hold for particle deletion – recall that a particle move represents the sum of a particle insertion in one cell and a particle deletion in another. Note that each subsequent insertion (or deletion) occurs at a slightly different cell occupancy and possibly a slightly different environment density. The corresponding move acceptance criterion for a multi-particle move is simply based on the sum of the single-particle free energy changes across the entire move and now becomes

$$\alpha_{ij}^{(n)} = \min\left[\exp\left(-\beta\sum_{i=1}^{n}\Delta A_i\right), 1\right]. \tag{5.4}$$

CG-MMC simulations with multi-particle moves were tested using the LJ-Ar potential at the state point $\rho^* = 0.3$ (homogeneously distributed across the domain) and $T^* = 0.9$. Recall that the dimensionless density and temperature are defined as $T^* \equiv k_B T / \varepsilon,\ \rho^* \equiv \rho\sigma^3$.

A cubic simulation domain consisting of 10 coarse cells in each direction was employed; the coarse-graining level was chosen to be $L_{cell} = 6\sigma$. The multi-particle moves were implemented by first defining a maximum number of particles that could be moved, $n_{\max}$, and then choosing the move size with a uniformly distributed random number in the interval [1, $n_{\max}$]. This move distribution was applied for all subsequent multi-particle move studies in this chapter. The CG-MMC simulations were allowed to evolve until equilibrium was reached and the cell density distribution was collected.

As shown in Figure 5.1, two different values for the maximum move size were used: $n_{\max} = 4$ (red squares) and $n_{\max} = 8$ (blue diamonds). The cell density distribution was obtained with a single-particle CG-MMC simulation is also shown in Figure 5.1 for comparison (black circles). As expected, the density distributions from all three simulations are essentially identical – note that there are no approximations implied in eqs. (5.3) and (5.4).

However, in the present formulation the multi-particle move simulations do not provide any computational benefit, even though the number of multi-particle moves required to reach equilibrium is lower than the corresponding number of single-particle moves. The reason for this is due to the sequential way in which the free energy change for the multi-particle moves was evaluated. In effect, each multi-particle move costs *n* times as much as a single particle move because the free energy change is accrued one particle move at a time. We develop improvements to this approach in the following section.

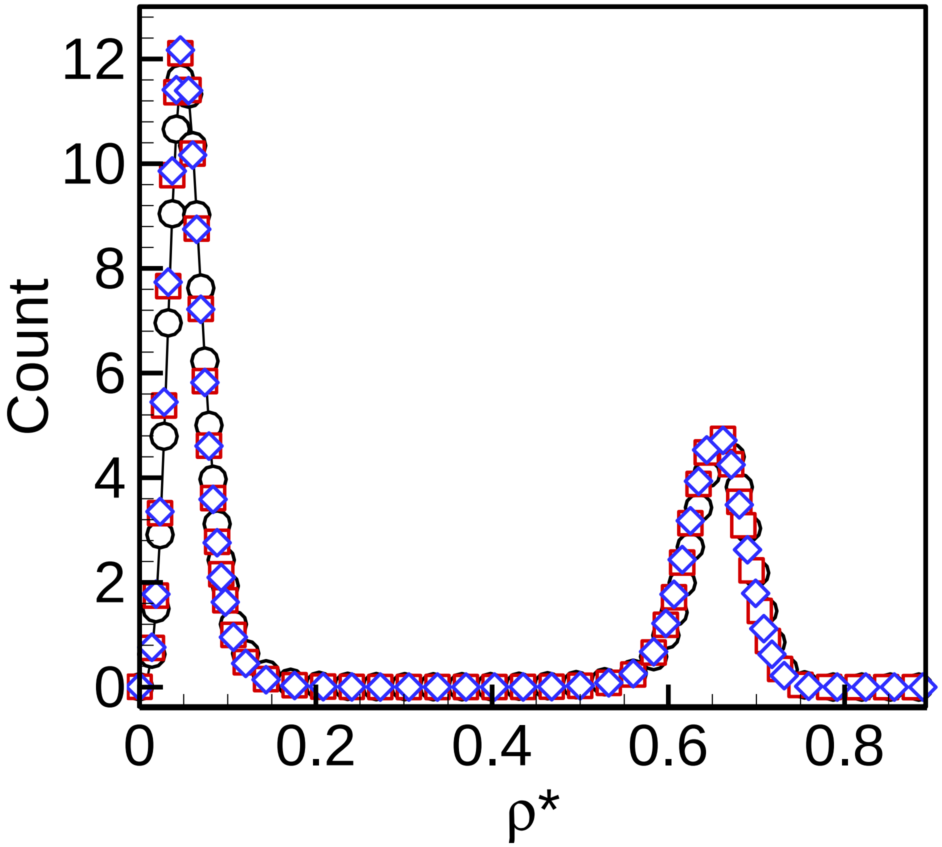

Figure 5.1: Unit area-normalized cell density histogram for LJ-argon obtained from equilibrated CG-MMC simulations with $L_{cell} = 6\sigma$ and $\rho^* = 0.3$ at $T^* = 0.9$. Black

circles – CG-MMC with single-particle move, red squares – CG-MMC with multi-particle move, $n_{\max} = 4$, blue diamonds – CG-MMC with multi-particle move, $n_{\max} = 8$.

5.3 Scalable Multi-Particle Moves in CG-MMC

Consider again the coarse-state dependence of the free change due to a single particle insertion

$$\Delta A(\rho, \rho_{env}, T) = \Delta A_{id}\left(\rho, T\right) + \Delta A_{ex}\left(\rho, \rho_{env}, T\right), \tag{5.5}$$

which makes explicit the fact that the free energy per particle insertion (deletion) changes as more particles are inserted (deleted). The total free energy change upon a multi-particle move can therefore be expressed as

$$\Delta A_{tot} = \sum_{i=1}^{n} \Delta A_i\left(\rho(n_i), \rho_{env}(n_i), T\right), \tag{5.6}$$

where n_i represents the number of particles in the cell for the i^{th} particle insertion. Eq. (5.6) can be expressed more generally in continuous form as

$$\Delta A_{tot} = \int_{n_{init}}^{n_{final}} \Delta A(\rho(n), \rho_{env}(n), T)\, dn, \tag{5.7}$$

where n_{init} and n_{final} represent the number of particles in the cell at the beginning and end of the multi-particle move, respectively.

We can now apply any of the standard numerical integration approximations to evaluate the integral in eq. (5.7). The cost of the evaluation is directly proportional to the number of integrand samples. In the following demonstrations we apply the single-interval trapezoid rule to evaluate eq. (5.7) for a multi-particle move, i.e.,

$$\int_a^b f(x)\,dx \approx \frac{b-a}{2}\left[f(a)+f(b)\right]. \tag{5.8}$$

The accuracy of the evaluation can be systematically increased by either using composite formulas such as

$$\int_a^b f(x)\,dx \approx \frac{b-a}{n}\left[\frac{f(a)}{2}+\sum_{i=1}^{n-1} f\left(a+\frac{i(b-a)}{n}\right)+\frac{f(b)}{2}\right], \tag{5.9}$$

or increasing the order of the numerical integration formula, e.g., Simpson's rule. Note that the single-interval trapezoid rule requires two integrand evaluations and therefore costs about twice as much as a single-particle move, *irrespective of the number of particles being moved.*

Rewriting eq. (5.7) in terms of the appropriate coarse-grained free energies gives

$$\Delta A = \sum_{i=1}^{n} \Delta A_i \approx \frac{n}{2}\left(\Delta A_1 + \Delta A_n\right), \tag{5.10}$$

where ΔA_1 is the change of free energy due to the first particle moved, and ΔA_n is the change of free energy due to the last particle moved. The corresponding move acceptance criterion now becomes

$$\alpha_{ij}^{(n)} = \min\left[\exp\left(-\beta\frac{n\left(\Delta A_1 + \Delta A_n\right)}{2}\right), 1\right] \tag{5.11}$$

The trapezoid approximation is tested using our standard base case simulation: a cubic domain comprised of 10 coarse cells on a side, with coarse-graining level $L_{cell} = 6\sigma$. The coarse-grained potential is derived from the LJ-Ar potential and the state point is given by $\rho^* = 0.3$ (initially uniform distribution) and $T^* = 0.9$. The equilibrium cell density distribution is shown in Figures 5.2 and 5.3 for multi-particle moves with $n_{\max} = 8$ (red squares), $n_{\max} = 16$ (blue diamonds), $n_{\max} = 80$ (green deltas), and single-particle moves (black circles).

The linear scales in Figure 5.2 show essentially perfect agreement between all cases, while the logarithmic scaling in Figure 5.3 highlights a small deviation between the multi-particle move and single-particle move cases in the intermediate part of the distribution, which corresponds to partially-filled cells at the boundary between liquid and vapor regions. Note that the bulk of the deviation occurs at very low values of the distribution. In addition, there is some additional deviation evident for the largest moves $n_{\max} = 80$; increasing the accuracy of the numerical integration scheme should resolve these errors. Finally, it is instructive to also consider the multi-particle moves in terms of the density change, $\Delta\rho^*$ (see Figure 5.2 and Figure captions). Here, the density change is defined as the average change in (dimensionless) cell density due to the multi-particle move, i.e., $\Delta\rho^* = (1+n_{\max})/2V_{cell}$. For the largest ($n_{\max} = 80$) moves, the average move size corresponds to $\Delta\rho^* = 0.1875$. The density change representation allows move sizes at different coarse-graining levels to be compared on a normalized basis. Overall our results show that the trapezoid rule estimation of the integral in eq. (5.10) is likely to be sufficient for the general case.

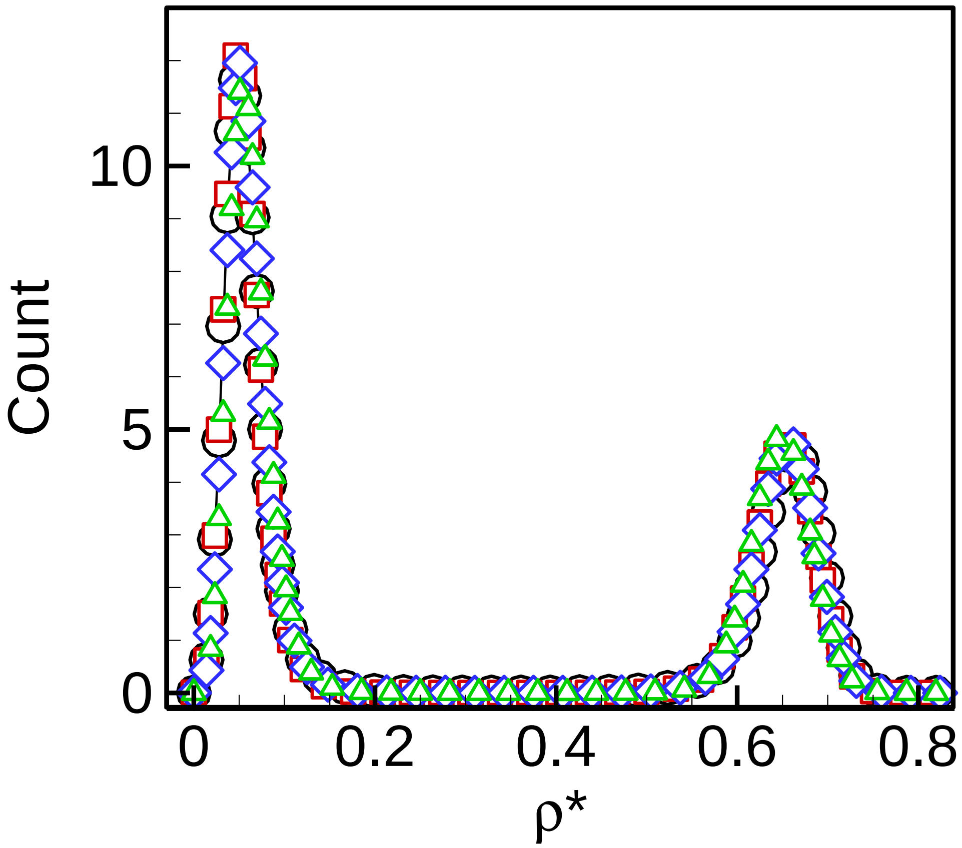

Figure 5.2: Unit area-normalized cell density histogram on linear scales for LJ-argon obtained from equilibrated CG-MMC simulations with $L_{cell} = 6\sigma$ and $\rho^* = 0.3$ at $T^* = 0.9$. Black circles – single-particle moves (reference case), red squares – multi-particle move: $n_{\max} = 8$ ($\Delta\rho^* = 0.0208$), blue diamonds – multi-particle move: $n_{\max} = 16$ ($\Delta\rho^* = 0.0394$), green deltas – multi-particle moves: $n_{\max} = 80$ ($\Delta\rho^* = 0.1875$).

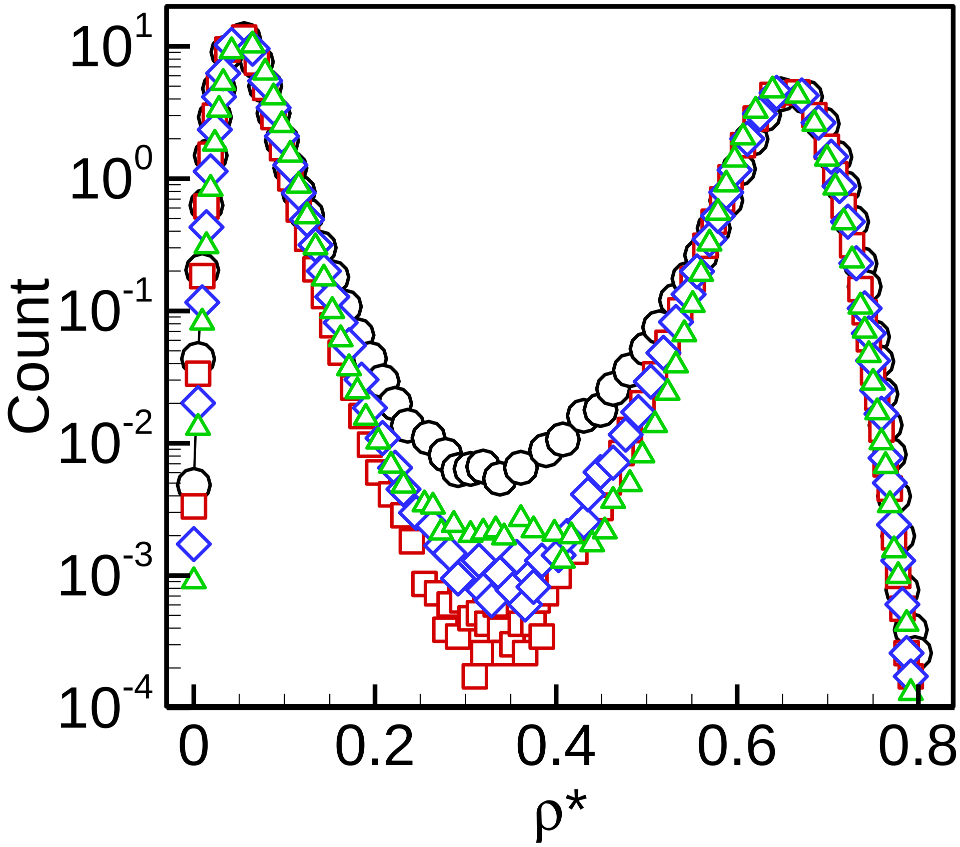

Figure 5.3: Unit area-normalized cell density histogram on logarithmic scales for LJ-argon obtained from equilibrated CG-MMC simulations with $L_{cell} = 6\sigma$ and $\rho^* = 0.3$ at $T^* = 0.9$. Black circles – single-particle moves (reference case), red squares – multi-paarticle move: $n_{\max} = 8$ ($\Delta\rho^* = 0.0208$), blue diamonds – multi-particle move: $n_{\max} = 16$ ($\Delta\rho^* = 0.0394$), green deltas – multi-particle moves: $n_{\max} = 80$ ($\Delta\rho^* = 0.1875$).

5.3.1 Analysis of Multi-Particle Move Efficiency

The efficiency gains associated with increasing the move size are partially tempered by a reduction in the move acceptance rate. Shown in Figure 5.4 is the acceptance ratio as a function of density change for two different coarse-graining levels. The plots were contructed using near-equilibrium configurations based on the LJ-argon potential at $\rho^* = 0.3$ and $T^* = 0.9$, although the results are not sensitive to these parameters. For both cell sizes, the average move acceptance probability, $<\alpha_{ij}>$, decreases with increasing move size. In both cases, the move acceptance rate appears to reach a limiting value of about 0.2 for the smaller cells and about 0.07 for the larger ones. Note that the acceptance probability is always lower in the larger cells for a given density change.

Although the relationship between the move acceptance probability and the move size is not analytically determined, it can be qualitatively observed that for both cell sizes, increasing the move size provides a net benefit in terms of efficiency, i.e., that across the entire range of move sizes considered here the move size grows faster than the acceptance probability decreases. For example, in the smaller cells, increasing the maximum number of particles per move in CG-MMC from 1 to 80, which corresponds to an average density change from $\Delta\rho^* = 0.0046$ to $\Delta\rho^* = 0.1875$, the acceptance ratio only decreases from around 90% to 20%. Optimal move size determination will require further study, particularly because the optimum move size is likely to be configuration and system specific.

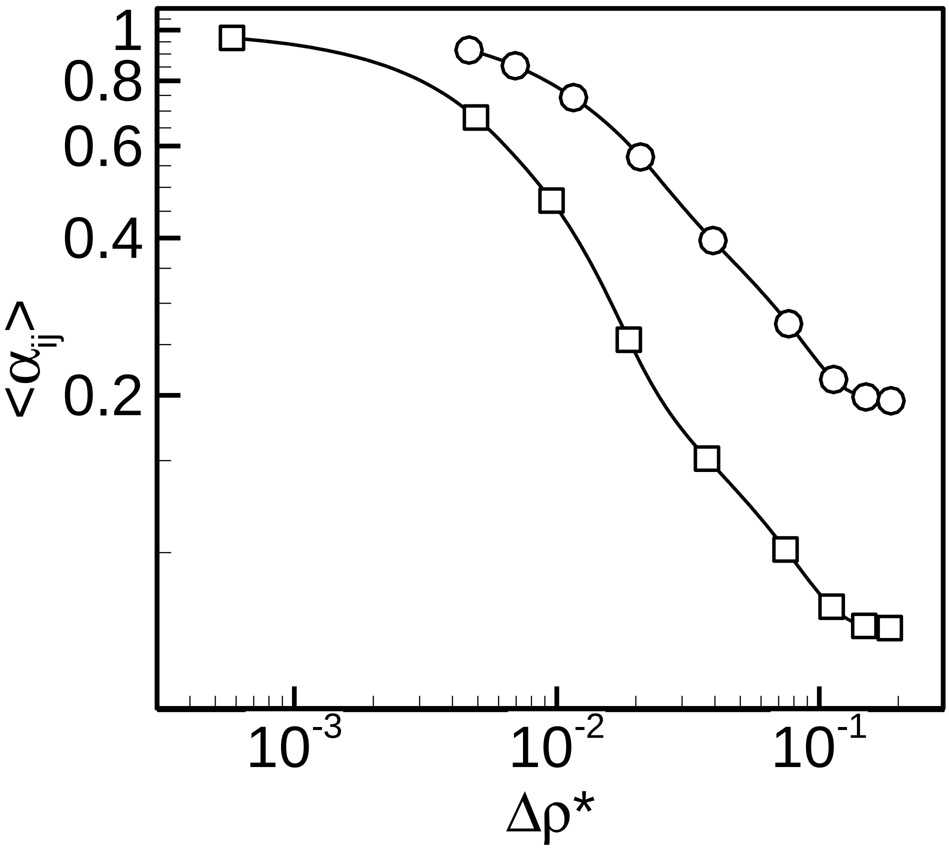

Figure 5.4: Acceptance probability as a function of move density change. Two cell sizes are considered: (a) $L_{cell} = 6\sigma$ (circles) and $L_{cell} = 6\sigma$ (squares). All data collected using LJ-Ar potential with near-equilibrium configurations at $\rho^* = 0.3$ and $T^* = 0.9$.

The influence of cell size on the acceptance probability deserves further analysis because the results in Figure 5.4 suggest a strong dependence between acceptance probability and cell size for a fixed move size (in terms of density change). In Figure 5.5 we show the acceptance probability as a function of cell size at a fixed density change, $\Delta\rho^* = 0.037$. Plotted on power-law scales, the acceptance rate first decreases slowly and then achieves an apparent constant power-law decrease with exponent $\left\langle \alpha_{ij} \right\rangle \sim \left(L_{cell} \right)^{-3/2}$. The practical implication of this result is important. Qualitatively speaking, for moves at fixed density change, the "time" that each move would correspond to in a CG-MMC simulation would scale as the diffusive time step times the acceptance probability times the number of particles that are moved with each successful attempt:

$$\tau \sim \frac{{L_{cell}}^2}{D} \cdot \left\langle \alpha_{ij} \right\rangle \cdot n_{\max} \sim n^{1.16}. \tag{5.12}$$

Note that in the above analysis it is assumed that the "time" equivalent of a single CG-MMC step is proportional to the number of particles moved in that step.

The principal implication of eq. (5.12) is that the CG-MMC method becomes increasingly efficient as the coarse cell size is increased even though the move acceptance rate becomes progressively smaller. In other words, not only does the method allow for larger length scale access, but it also appears to provide longer timescale access as the coarse-graining level is increased. This is a critical property of any coarse-graining approach because features that exist at larger length scales almost always evolve at longer timescales. It is not clear whether the present conclusions hold for coarse-graining levels beyond the range investigated here – future studies will be required to probe the behavior of the CG-MMC (or NECG-MMC) method in the limit of very large cell sizes.

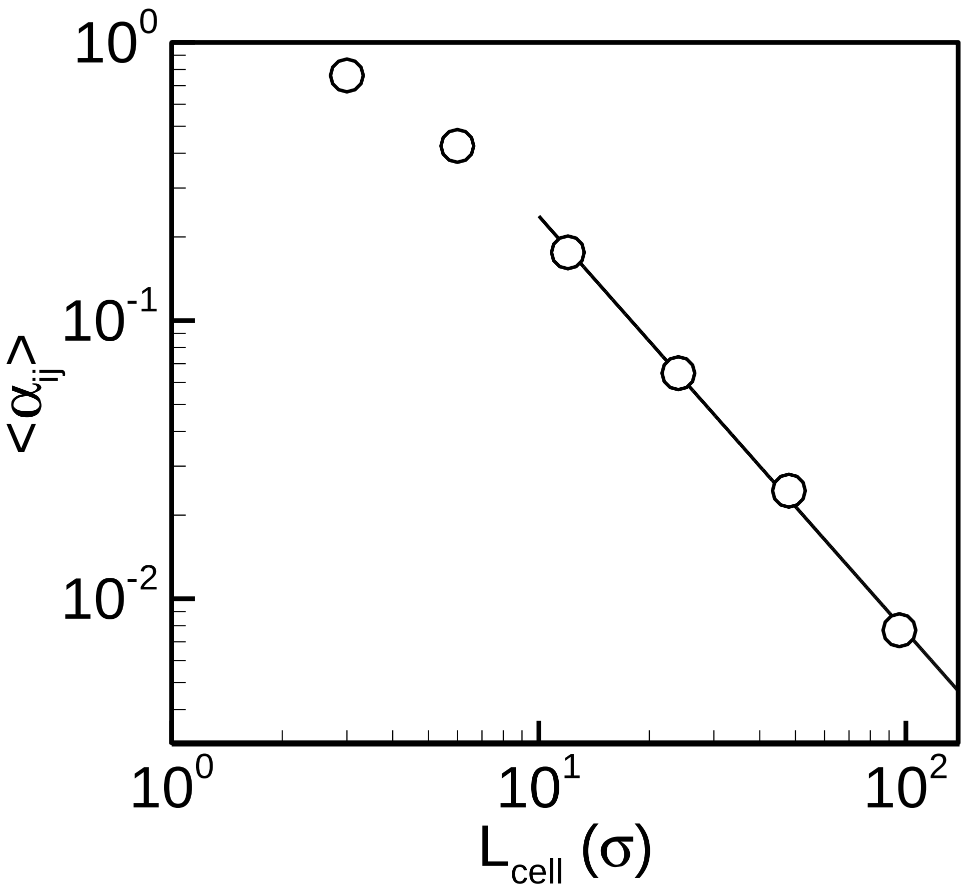

Figure 5.5: Acceptance probability as a function of coarse cell size at fixed density change, $\Delta\rho^* = 0.037$. Line shows power-law fit over the interval shown. All data collected using LJ-Ar potential with near-equilibrium configurations at $\rho^* = 0.3$ and $T^* = 0.9$.

5.4 Adaptive Scaling Using CG-MMC Models

In the remainder of this chapter we use a simple example of a non-equilibrium system to demonstrate the advantages and possible applications of the CG-MMC (or NECG-MMC) method. We consider the spinodal decomposition of a homogeneously-distributed LJ-Ar fluid at $\rho^* = 0.3$ and $T^* = 0.8$ into equilibrium liquid and vapor phases. We use a large system comprised of 80 coarse cells on a side at a coarse-graining level of $L_{cell} = 3\sigma$ so that the total simulation domain volume is $240 \times 240 \times 240\sigma^3$, which at the given density, corresponds to more than 4,000,000 atoms; see Figure 5.6(a). At this coarse-graining level, single particle moves are performed, which corresponds to a density change of $\Delta\rho^* = 0.037$.

The $L_{cell} = 3\sigma$ simulation first is executed for 6×10^4 CG-MMC sweeps (corresponding to 3.1×10^{10} moves). As shown in Figure 5.6(b), the extent of evolution is still quite limited and the length scale associated with the homogeneous spinoldal decomposition is only a few cells. Moreover, further evolution will take place at an ever-slowing rate making the approach to equilibrium (or anything near it) difficult, even with coarse-graining. We now continue the simulation by (1) upscaling the coarse-grained potential to $L_{cell} = 6\sigma$ and (2) upscaling the configuration in Figure 5.6(b) to the same level, as shown in Figure 5.6(c). Note that at the new coarse-graining level the simulation domain is now comprised of 40 coarse cells on a side. Also note that much of the detail that was discernible at the finer scale is now lost. The simulation is now continued using multi-particle moves with the same density change, i.e., $\Delta\rho^* = 0.037$; these correspond to moving about 8 particles on average. The configuration following 1.5×10^4 sweeps (9.6×10^8 moves) is shown in Figure 5.6(d). The system has clearly evolved at a much faster rate per move at the new coarse-graining level

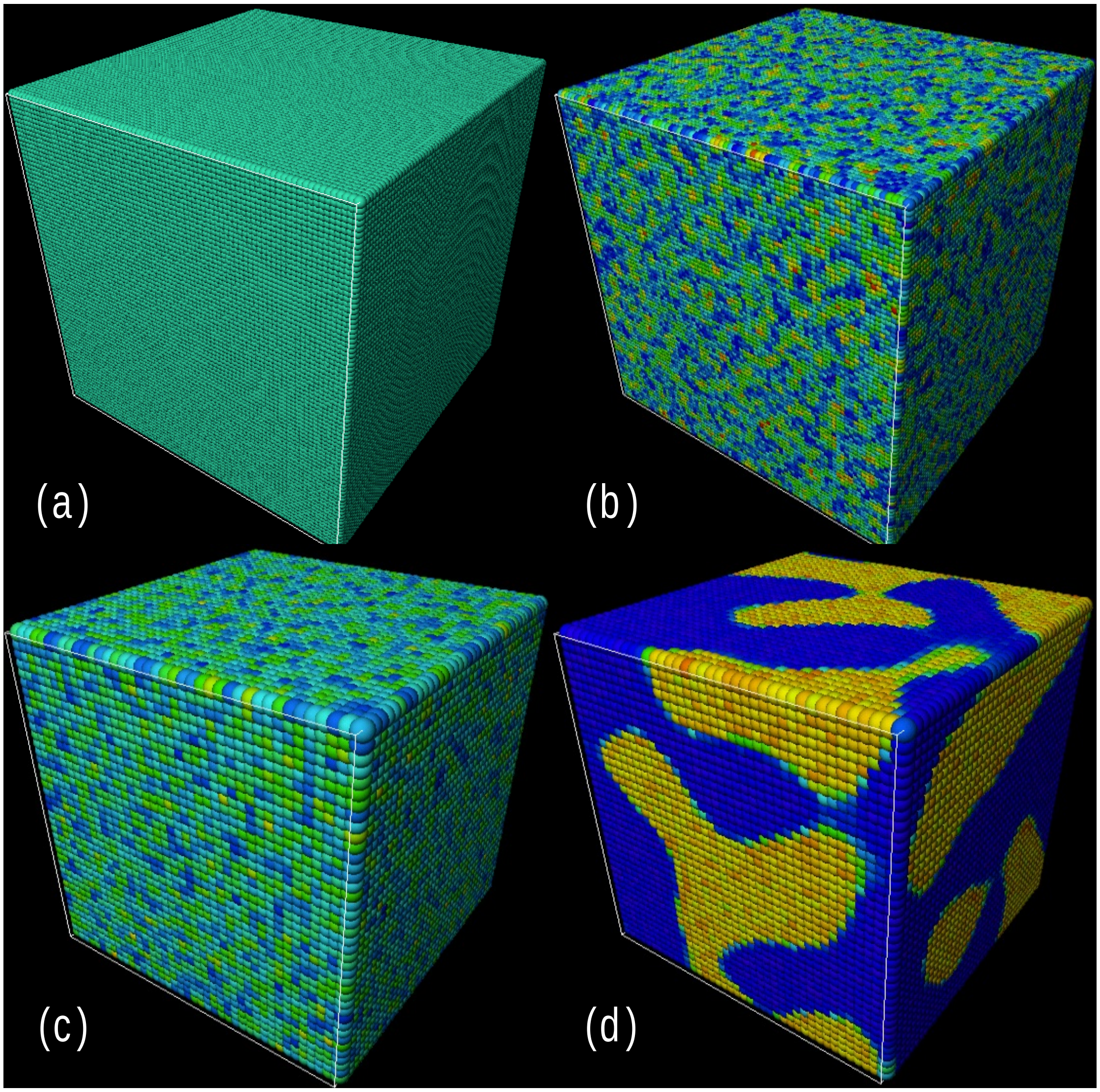

Figure 5.6: CG-MMC simulation configurations at $T^* = 0.8$ and $\rho^* = 0.3$. (a) Initial condition ($L_{cell} = 3\sigma$), (b) after 6×10^4 CG-MMC sweeps ($L_{cell} = 3\sigma$), (c) configuration (b) upscaled to $L_{cell} = 6\sigma$ (d) after 1.5×10^4 CG-MMC sweeps ($L_{cell} = 6\sigma$). Cell color denotes reduced density ρ^* that ranges from zero (dark blue) to 0.9 (red). Density change per move at all coarse-graining levels is $\Delta\rho^* = 0.037$.

The adaptive coarse-graining procedure is continued by taking the configuration from Figure 5.6(d) and upscaling it to the $L_{cell} = 12\sigma$ coarse-graining level as shown in Figure 5.6(e). At the $L_{cell} = 12\sigma$ level, the simulation domain consists of 20 coarse cells on a side and although the move size is unchanged in terms of the density change, the maximum number of particles per move is now 64. A total of 1.0×10^4 sweeps (8×10^7 moves) leads to the configuration shown in Figure 5.6(f). One final upscaling step is applied to map the configuration onto the $L_{cell} = 24\sigma$ coarse-graining level (Figure 5.6(g)) and the system is then evolved for another 1.0×10^4 sweeps (1×10^7 moves).

The final configuration shown in Figure 5.6 is at equilibrium. However, we claim that this configuration is not just an example configuration of the equilibrium state, but rather *the* equilibrium configuration. In other words, at the $L_{cell} = 24\sigma$ coarse-graining scale we claim that we are able to reach a macroscopically meaningful equilibrium, rather than just statistical equilibrium. While the latter is only meaningful when averaged over time or a number of instances, the former is defined at any instant of time. Note that the particular configuration shown in Figure 5.6(h) is of bicontinuous form due to the nature of the periodic boundary condition – the system simply cannot further reduce the vapor-liquid surface area unless these boundary conditions are relaxed. We again emphasize that it would be extremely computationally expensive to run the CG-MMC simulation at lower coarse-graining levels to this point – not only because the system has more coarse cells but because the implied time interval corresponding to each move is much smaller.

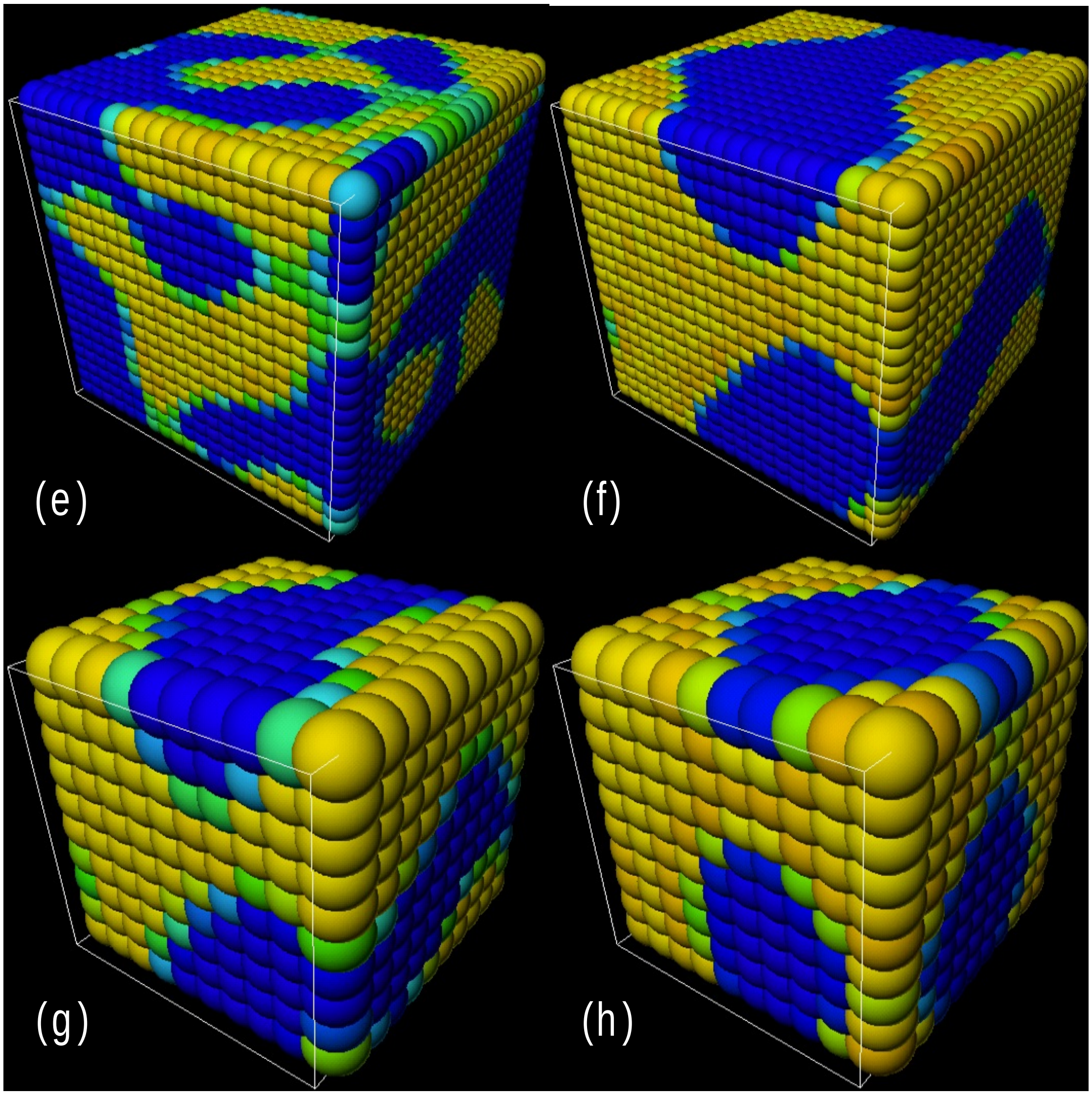

Figure 5.6: CG-MMC simulation configurations at $T^* = 0.8$ and $\rho^* = 0.3$. (e) configuration (d) upscaled to $L_{cell} = 12\sigma$, (f) after 1.0×10^4 CG-MMC sweeps ($L_{cell} = 12\sigma$), (g) configuration (f) upscaled to $L_{cell} = 24\sigma$, (h) after 1.0×10^4 CG-MMC sweeps ($L_{cell} = 24\sigma$). Cell color denotes reduced density ρ^* that ranges from zero (dark blue) to 0.9 (red). Density change per move at all coarse-graining levels is $\Delta\rho^* = 0.037$.

We next perform a "control" simulation in which the coarse-graining level is fixed $L_{cell} = 24\sigma$ from the initial configuration shown in Figure 5.6(a). The same overall domain size, move size, and coarse state point are used for this run.. The equilibrium configuration obtained from this simulation (following a total of 1×10^6 sweeps or 1×10^9 moves) is shown in Figure 5.7, along with Figure 5.6(h) for comparison. The bicontinuous configurations are essentially identical further demonstrating the uniqueness of the final equilibrium configuration. The demonstration in Figure 5.7 also highlights the fact that unless the early-time configurations are required, one could always run the entire simulation at the final required coarse-graining level. Note that only a total of 1×10^9 CG-MMC moves were required in the second simulation. In the adaptively scaled simulation, the number of moves was about 30 times larger, with the vast majority being applied at the lowest coarse-graining scale.

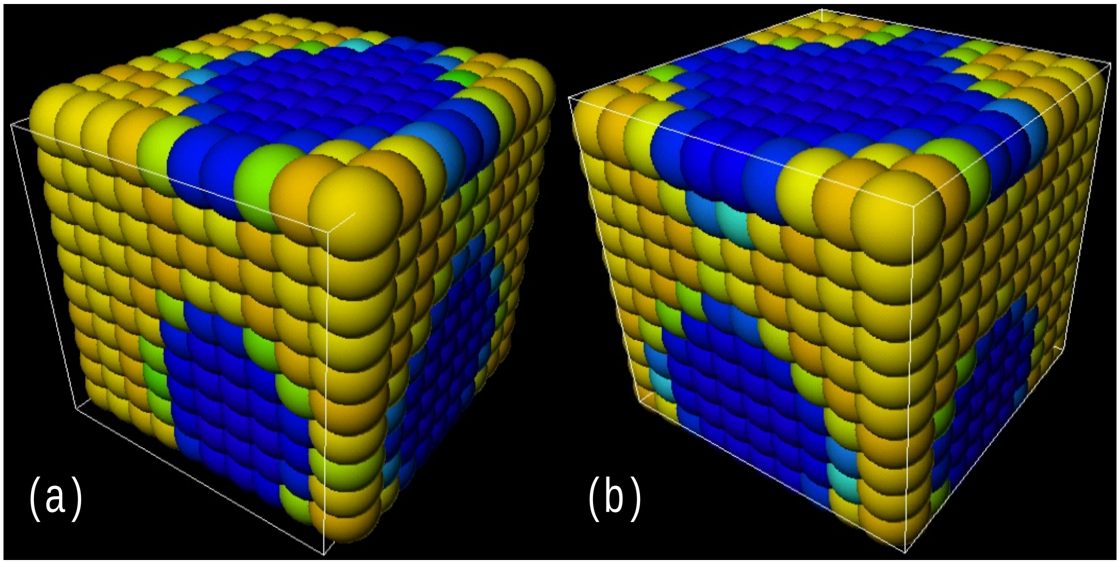

Figure 5.7: Equilibrium CG-MMC simulation configurations at $T^* = 0.8$ and $\rho^* = 0.3$ for LJ-Ar. (a) Adaptive coarse-grained simulation (see Figure 5.6 for details), (b)

constant coarse-graining at $L_{cell} = 24\sigma$. Cell color denotes reduced density $\rho*$ that ranges from zero (dark blue) to 0.9 (red).

Finally, we ask the question: what if we require a high-resolution image of the equilibrium configuration? Taking the $L_{cell} = 24\sigma$ configuration in Figure 5.7(a), we performed a gradual downscaling in which the configuration was mapped onto a higher resolution level ($L_{cell} = 12\sigma$), evolved for 2.5×10^4 sweeps (2×10^8 moves), and then remapped onto the next higher level, all the way until the $L_{cell} = 3\sigma$ coarse-graining level was reached. The results are shown in Figure 5.8. The final configuration (Figure 5.8(g)) exhibits the macroscopic equilibration that would have been impossible to reach at the $L_{cell} = 3\sigma$ level, while also showing the details of the intra-phase structure and giving a clean view of the structure at the interface. In principle, this configuration could be used to initialize a full-resolution standard MMC run to obtain an explicitly atomic view.

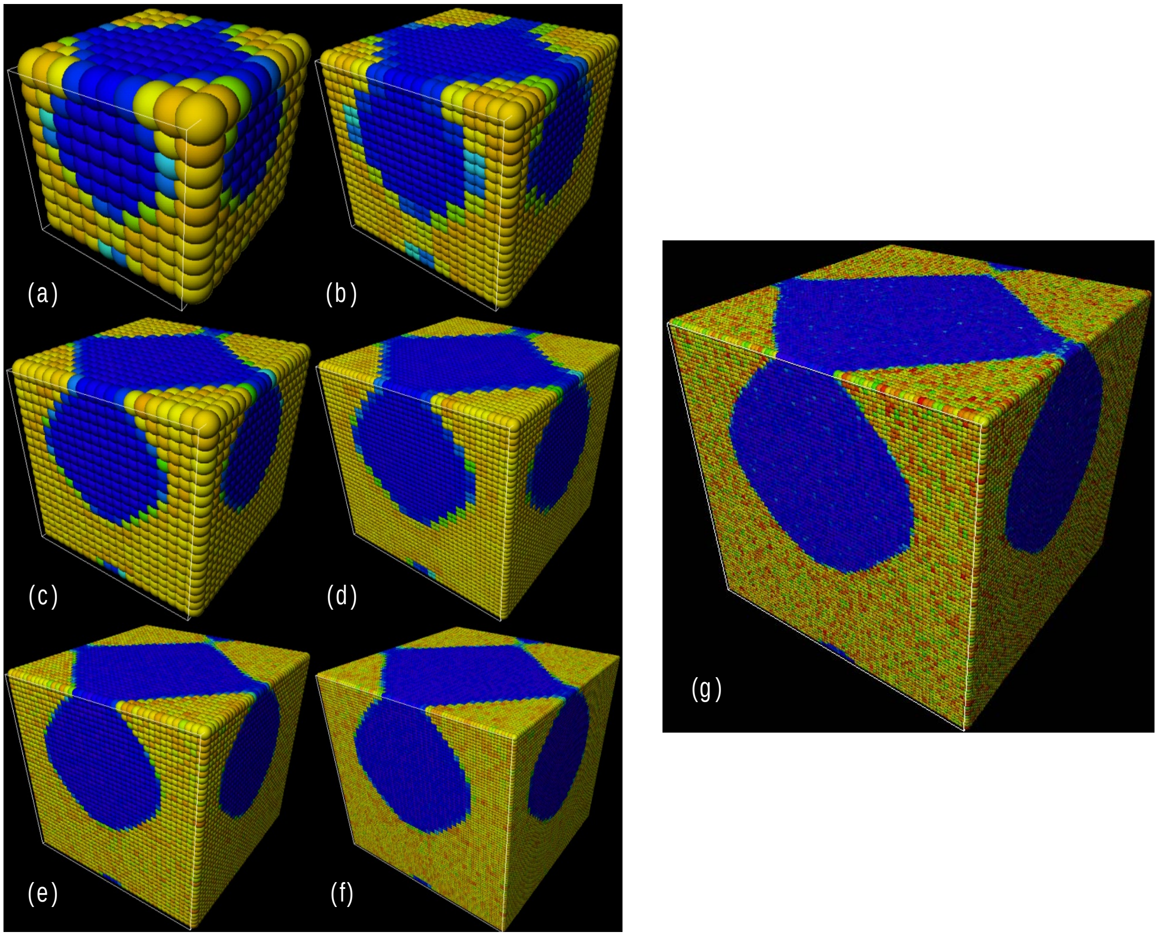

Figure 5.8: CG-MMC simulation configurations at $T^* = 0.8$ and $\rho^* = 0.3$ for LJ-Ar. (a) Equivalent configuration of Figure 5.7(a) downscaled to $L_{cell} = 12\sigma$, (b) after 2.5×10^4 CG-MMC sweeps ($L_{cell} = 12\sigma$), (c) configuration (b) downscaled to $L_{cell} = 6\sigma$, (d) after 1.5×10^4 CG-MMC sweeps ($L_{cell} = 6\sigma$), (e) configuration (d) downscaled to $L_{cell} = 3\sigma$, (f) after 1.5×10^3 CG-MMC sweeps ($L_{cell} = 3\sigma$), (g) enlarged configuration (f), which exhibits the macroscopic equilibration. Cell color denotes reduced density ρ^* that ranges from zero (dark blue) to 0.9 (red). Density change per move at all coarse-graining levels is $\Delta\rho^* = 0.037$.

More generally, one could envision applying the "coarse timestepper" idea within the equation-free strategy espoused by Kevrekidis and coworkers in a large number of studies [1-8]. In the present embodiment, a system is propagated along a trajectory at a coarse level, which provides long-time access. Periodically, the system is downscaled (or "lifted" in the terminology of refs. [2-5]) to a lower coarse-graining representation and locally equilibrated to provide a detailed local picture for computing highly-resolved quantities. Following this, the configuration can be again upscaled (or "restricted") to a higher coarse-graining level and evolved further. While superficially similar to the ideas proposed by Kevrekidis and coworkers, here the downscaling steps serve only to refine the solution at various points along the way and do not provide any refinement of the coarse timestepper characteristics. In other words, no new information is computed from the high-resolution configurations because all the required information was computed once at the beginning in the form of a scalable coarse-grained potential. In contrast, in refs. [2-5] the lifting steps serve to repeatedly compute new properties for use at the coarse level.

5.5 Conclusions

In this chapter a strategy for perfoming multi-particle moves was introduced and shown to provide substantial increase in CG-MMC efficiency. The salient features of multi-particle moves are as follows. Using simple numerical integration approximations we showed that a multi-particle move can be executed with about the same amount of work as two single-particle moves and is independent of the number of particles being moved. The acceptance probability of multi-particle moves was shown to decrease as the number of particles being moved increased and also as the coarse-graining level increased. However, it was also shown that this decrease was more than compensated for by the gains associated with larger coarse-graining levels and therefore that the CG-MMC method, at least over the scales investigated here, continues to improve in terms of efficiency as the coarse-graining level is increased.

The multi-particle move CG-MMC method was demonstrated using a spinodal decomposition simulation example for the LJ-Ar system. In this demonstration, the simulation resolution was reduced gradually to provide adequate information at each stage of the coarsening process but still enable access to long timescales. The final structure was shown to be a macroscopically equilibrium configuration. Moreover, it was shown that this configuration could be subsequently remapped to the highest resolution level using short re-equilibration runs after each refinement step. The final structure offers a high resolution view of a configuration that is otherwise inaccessible by simulation at a single coarse-graining level.

It is worth considering here briefly the limit of very large (i.e., continuum) coarse-graining. At such scales, it is obvious that the density fluctuations which are prevalent at small scales are no longer viable. On the other hand, it is obvious that density fluctuations are a necessary consequence of MMC moves. This apparent paradox suggests that the usual type of MMC moves will eventually become a bottleneck as the coarse-graining scale becomes very large, i.e., that it will deviate from the analysis in Section 5.4. Whether this is in fact the case should be the subject of further study.

In conclusion, the ability to perform multi-particle moves enables CG-MMC simulation at very high coarse-graining levels, not only provides access to large length scales, but also to long time scales. In fact, it is the latter that is generally the principal bottleneck in many applications. Moreover, the flexible coarse-graining in CG-MMC enables one to refine the system state at any point to a higher-resolution configuration. The resulting toolkit now offers the capability of studying long-timescale non-equilibrium phenomena, which we believe are the primary targets of the CG-MMC technique.

References

---

[1] C. Theodoropoulos, Y. H. Qian and I. G. Kevrekidis, *Proc. Natl. Acad. Sci.* **97**, 9840 (2000).

[2] C. W. Gear, I. G. Kevrekidis and C. Theodoropoulos, *Comput. Chem. Eng.* **26**, 941 (2002).

[3] I. G. Kevrekidis, C. W. Gear, J. M. Hyman, P. G. Kevrekidis, O. Runborg, and C. Theodoropoulos, *Comm. Math. Sci.* **1**, 715 (2003).

[4] I. G. Kevrekidis and G. Samaey, *Annu. Rev. Phys. Chem.* **60**, 321 (2009).

[5] C. W. Gear, T. J. Kaper, I. G. Kevrekidis and A. Zagaris, *SIAM J. Appl. Dyn. Syst.* **4**, 711 (2005).

[6] A. Bindal, M. G. Ierapetritou, S. Balakrishnan, A. Armaou, A.G. Makeev, and I. G. Kevrekidis, *Chem. Eng. Sci.* **61**, 779 (2006).

[7] F. J. Alexander, G. Johnson, G. L. Eyink, and I. G. Kevrekidis, *Phys. Rev. E.* **77** 026071 (2008).

[8] I. G. Kevrekidis, C. W. Gear, and G. Hummer, *AIChE J.* **50**, 1346 (2004).

Chapter 6

Conclusions and Future Work

6.1 Conclusions

In this thesis, a new framework for coarse-graining Metropolis Monte Carlo simulations of fluids is developed and validated. The CG-MMC model is apparently potential independent and can be applied to simulate atomic and molecular fluid systems described by standard molecular potential field. The basic approach is that a thermodynamically consistent coarse-grained interaction potential is first obtained numerically and automatically from a continuous potential field such as Lennard-Jones. The coarse-grained potential then is used to drive CG-MMC simulations. The CG-MMC technique is demonstrated to be highly thermodynamically consistent with the underlying full resolution simulations using a series of detailed comparisons, including vapor-liquid equilibrium phase envelopes and spatial density distributions for the square well, Lennard-Jones argon and simple point charge (SPC) water models.

The CG-MMC model is further analyzed and extended. The principal computational bottleneck associated with computing a coarse-grained interaction function for evolving particle positions on the discretized domain is addressed by the introduction of new closure approximations. In particular it is shown that the coarse-grained potential, which, like all coarse-grained interaction functions, is generally a function of temperature and coarse-graining level, can be computed at multiple temperatures and scales using a single set of free energy calculations. The utility of the method is demonstrated using a non-equilibrium simulation of phase coarsening in a fluid system. The computational performance of the method relative to standard Monte Carlo simulation also is discussed.

The CG-MMC model is shown to satisfy detailed balance, but requires additional adjustment in order to reproduce non-equilibrium dynamic process. Subsequent non-equilibrium CG-MMC model (NECG-MMC) is built based on biased coarse cell selection adjustment with detailed balance requirement satisfied. Both diffusion and drift-diffusion processes are tested for ideal gas case and Lennard-Jones potential case starting from Gaussian distribution. NECG-MMC model is proved to be able to capture the correct non-equilibrium dynamic evolution by comparing to analytical solutions, while the CG-MMC model fails. Moreover, the NECG-MMC model is also proved to maintain a direct mapping between NECG-MMC steps and simulation time at different coarse-graining levels.

Coarse-grained potentials can be scaled from one coarse-graining scale to another, potentially allowing for extremely large length scales to be accessed with the atomistic potential as the only input. A strategy for performing multi-particle moves was introduced and shown to provide substantial increase in CG-MMC efficiency. The multi-particle move CG-MMC model is successfully applied in adaptive scaling and large-scale simulations using a spinodal decomposition example for the LJ-Ar system.

6.2 Future Work

6.2.1 Coarse-Grained Kinetic Monte Carlo Model

An important limitation of CG-MMC is the lack of an explicit measure of time in non-equilibrium simulations. Although it is possible to make formal connections between non-equilibrium Metropolis Monte Carlo and Langevin dynamics under certain conditions (e.g., sufficiently small move distances) [1], the use of Metropolis Monte Carlo for studying dynamical evolution in non-equilibrium settings is not ideal. The CG-MMC model developed in this thesis provides a framework to follow when developing coarse-grained lattice kinetic Monte Carlo (CG-LKMC) simulations, whose only input is the same coarse-grained potential used in CG-MMC simulations. In any lattice kinetic Monte Carlo simulation, the primary input is a database of rates for all allowable events at a given configuration. Once the rates are established, move events are selected in a biased random manner with faster events being chosen more often – the resulting evolution dynamics are explicit in time. Using the general theory of drift-diffusion, as represented by the Smoluchowski equation, it is possible to express rates for any given event such as a particle move, in terms of an underlying potential function (coarse-grained or otherwise). We will use these ideas to translate CG-MMC into CG-LKMC simulations to allow for explicit-time non-equilibrium calculations; the technical details are presented as follows.

In this section, we will show the derivation of the equivalent stochastic processes between Lattice Kinetic Monte Carlo model (LKMC) and Brownian dynamics model (BD).

6.2.1.1 Overdamped Langevin Dynamics

Consider again the one-dimensional Fokker-Planck equation eq. (4.2) in Chapter 4 [2, 3] into which the results from eqs. (4.7) and (4.8) are substituted:

$$\frac{\partial P(X,t)}{\partial t}=\frac{1}{\gamma}\frac{\partial}{\partial X}\left[\left(\frac{\partial U}{\partial X}\right)P(X,t)\right]+\frac{\partial^2}{\partial X^2}\left[D(X)P(X,t)\right]. \tag{6.1}$$

Assuming further that that the diffusion coefficient is not a function of position (or time) and removing the explicit dependence of the distribution on position and time gives the following convection-diffusion equation:

$$\frac{\partial P}{\partial t}=-\frac{\partial}{\partial X}\left[\frac{F}{\gamma}P\right]+D\frac{\partial^2 P}{\partial X^2}, \tag{6.2}$$

where $F=-(\partial U/\partial X)$ is the force acting on the system due to an external potential. Recall again that the diffusion coefficient also is related to the friction coefficient, γ, by the Einstein relationship [4], $D/k_BT=1/\gamma$. Let's assume the force field is constant, eq. (6.2) becomes

$$\frac{\partial P}{\partial t}=-v\frac{\partial P}{\partial X}+D\frac{\partial^2 P}{\partial X^2}, \tag{6.3}$$

where $v=\frac{F}{\gamma}=F\frac{D}{k_BT}$ is the constant drift coefficient.

A physical model of the drift-diffusion problem in eq. (6.3) is an overdamped particle subjected to a constant force field, which adds a constant drift velocity superimposed on the Brownian motion. There are two equivalent ways of describing this overdamped Brownian dynamics. One is to describe the time evolution of the probability distribution $P(X,t)$, the other is to describe the position evolution $X(t)$ using Langevin equation [4]:

$$\frac{dX}{dt}=v+D^{1/2}\xi_G, \tag{6.4}$$

where ξ_G is a Gaussian white noise.

If the particle starts from the origin moves between two absorbing boundaries *-L* and *L*, the splitting probability, i.e. the probability that the particle is absorbed finally by the left- or the right-hand boundary [4] gives

$$\mathrm{Pr}_{<-} = \frac{\exp(-Lv/D)}{1+\exp(-Lv/D)}, \tag{6.5}$$

and

$$\mathrm{Pr}_{->} = \frac{1}{1+\exp(-Lv/D)}, \tag{6.6}$$

with $\mathrm{Pr}_{->} + \mathrm{Pr}_{<-} = 1$. Only the right-hand splitting probability will be considered for simplicity.

The mean first-passage time, i.e. the average time it takes for the particle to be absorbed by any of the boundaries is

$$\tau = \frac{L}{v}\frac{1-\exp(-Lv/D)}{1+\exp(-Lv/D)}. \tag{6.7}$$

6.2.1.2 Equivalent Lattice Kinetic Monte Carlo Description

When mapping the continuous motion onto lattice model with lattice spacing ΔL, where $\Delta L = \frac{L}{N}$, we suppose the particle moves distance ΔL in either x^+ or x^- direction, with rate R_+ and R_- respectively.

Suppose the velocity is in x^+ direction, the random walk is biased with higher probability moving in x^+ than in x^- direction. The probability to move in x^+ is

$$p_+ = \frac{R_+}{R_+ + R_-}, \tag{6.8}$$

and the probability to move in x^- is

$$p_- = \frac{R_-}{R_+ + R_-}. \tag{6.9}$$

with $p_+ > p_-$ and $p_+ + p_- = 1$.

Following the KMC algorithm, average updated time for each hop is

$$\Delta\tau = \frac{1}{R_+ + R_-}. \tag{6.10}$$

Separate the transport process into diffusion and convection with rates:

$$R_d = \frac{D}{L^2}, \tag{6.11}$$

and

$$R_c = \frac{v}{L}. \tag{6.12}$$

In a real physical system, there are two apparent constraints that should be satisfied: (i) the detailed balance, and (ii) the equality between the difference of the two rates and the convection rate. It follows

$$\frac{R_+}{R_-} = \exp(-\beta\Delta U), \tag{6.13}$$

as well as

$$R_+ - R_- = R_c. \tag{6.14}$$

In a lattice model, $\frac{v\Delta L}{D} = -\beta \Delta U$, therefore eq. (6.13) becomes

$$\frac{R_+}{R_-} = \exp(\frac{v\Delta L}{D}) . \tag{6.15}$$

Base on Eq. (6.8, 6.9, 6.10, 6.14, 6.15), probability for each hop has following relation:

$$\frac{p_+}{p_-} = \exp(\frac{v\Delta L}{D}) . \tag{6.16}$$

$$\frac{p_+ - p_-}{\Delta \tau} = \frac{v}{\Delta L} . \tag{6.17}$$

The splitting probability for biased random walk is exactly expressed as:

$$\mathrm{Pr}_{->} = \frac{1}{1 + (p_+ / p_-)^N} . \tag{6.18}$$

The mean first-passage time is

$$\tau = \frac{2(\mathrm{Pr}_{->} - 1)}{p_+ - p_-} N \Delta \tau . \tag{6.19}$$

Comparing Eq.(6.16, 6.17, 6.18, 6.19) with Eq.(6.6, 6.7), we get the same splitting probability and first-passage time, which proves the equivalence of LKMC model and BD model.

Even though the derivation is based on the constant-force assumption, the equivalence holds as long as the lattice spacing is small enough so that the force is constant between before and after each hop. In this sense, lattice spacing determines the accuracy in LKMC as time step in BD. There is no analytical solution in a variable force field, we have shown both BD and LKMC are equivalent numerical models to simulate the dynamical process.

Base on Eq. (6.14, 6.15), the rates in LKMC model for each hop are:

$$R_{-} = \frac{v}{\Delta L}\frac{1}{\exp(v\Delta L / D) - 1} = R_c \frac{1}{\exp(\omega) - 1}. \tag{6.20}$$

$$R_{+} = \frac{v}{\Delta L}\frac{\exp(v\Delta L / D)}{\exp(v\Delta L / D) - 1} = R_c \frac{\exp(\omega)}{\exp(\omega) - 1}. \tag{6.21}$$

where $\omega = \frac{R_c}{R_d} = \frac{v\Delta L}{D}$.

Additionally, as $\omega << 1$, Taylor expansion of exponential to the first order is $\exp(\omega) = 1 + \omega + O(\omega^2)$. Therefore, the first-order truncation rates are (named as KMC $O(\omega)$):

$$R_{-} = R_d = R_c \frac{1}{(1+\omega) - 1}. \tag{6.22}$$

$$R_{+} = R_d + R_c = R_c \frac{1+\omega}{(1+\omega) - 1}. \tag{6.23}$$

6.2.2 Extension to Complex Systems

The CG-MMC and NECG-MMC models developed in Chapter 2 and Chapter 4 respectively are potential independent and can be applied to simulate atomic and molecular fluid systems described by standard molecular potential field. These models can be expanded to further explore other more complex systems that active research has been focused on.

6.2.2.1 Extension to the Solid State

The first case for possible future work is the extension of spatial coarse-graining to solid phases, thereby enabling simulations of solidification and melting. The primary challenge here is again the poor ergodicity of solid phases, which essentially renders particle insertion useless. While free energy estimation for a single solid configuration, e.g., a perfect crystal, is straightforward because only vibrational entropy is significant, sampling over a collection of solid configurations that include disorder such as defects is much more challenging. It may not be necessary to seamlessly sample the entire energy landscape across the solid and liquid macrostates in order to compute an adequate coarse-grained potential for use in CG-MMC simulations because in the coarse-grained state-space it is not possible to identify features such as the onset of nucleation. The quality of coarse-grained potential "patching" across the liquid and solid macrostates required for meaningful simulations of melting and solidification will be the focus of our investigations.

6.2.2.2 Extension to Charged Systems

The second case for possible future work is the consideration of charged systems in which long-ranged Coulombic interactions must be accounted for; this issue was circumvented in our preliminary work by using a spherically truncated model for water. Approaches such as the Ewald summation method [5] are not compatible with SCG because of the heterogeneous cell structure used in the coarse-grained potential evaluations. However, other methods for approximating Coulombic interactions using modified short-ranged interaction functions appear to be promising; examples include the reaction-field method [6] and the Wolf summation [7]. It will be applicable extension to incorporate these methods into CG-MMC simulations with the aim of enabling coarse-grained simulations of charged systems.

6.2.2.3 Extension to Multiple-component Systems

The third case for possible future work is the application in multi-component systems. The number of independent variables over which coarse-grained potentials are defined, e.g., density, composition, temperature, represents the dimensionality of the coarse-grained space and is the single most important factor in establishing the computational overhead associated with coarse-grained potential evaluation. The ability to consider multicomponent systems is critical for extending the horizon of spatial coarse-grained methods. Consider, for example, the case in which the independent variables for a single-component system at a given temperature are the cell particle density and the average local environment density. Extending the system to two components would require that the cell and environment fields be now described by two density variables each. Effectively, the coarse-grained potential is transformed from a two-dimensional field in the single-component case to a four-dimensional one in the binary case. Similar considerations apply for additional species. If strategies to enable optimal (and sparse) sampling of high-dimensional fields can be implemented, then interpolated coarse-grained potential functions for multicomponent systems and be construct, the CG-MMC framework will be applied to multicomponent systems.

References

---

[1] R. T. Scarlett, J. C. Crocker, and T. Sinno, *J. Chem. Phys.* **132**, 234705 (2010).

[2] R. K. Pathria, *Statistical Mechanics,* 2nd ed. (Elsevier Butterworth-Heinemann, Boston, 1996).

[3] N. G. v. Kampen, *Stochastic Processes in Physics and Chemistry* (Elsevier, Amsterdam, 2007).

[4] H. Risken, *The Fokker-Planck Equation: Methods of Solution and Applications*, end ed. (Springer, Berlin, 1996).

[5] M. Mezei, *Mol. Simul.* **9**, 257 (1992).

[6] I. G. Tironi, R. Sperb, P. E. Smith, and W. F. Vangunsteren, *J. Chem. Phys.* **102**, 5451 (1995).

[7] D. Wolf, P. Keblinski, S. R. Phillpot, and J. Eggebrecht, *J. Chem. Phys.* **110**, 8254 (1999).